Extended Structures in Globular Clusters

Pete B. Kuzma

A thesis submitted for the degree of
Doctor of Philosophy of
The Australian National University

September, 2017

Declaration

This thesis is an account of research undertaken between February 2013 and September 2017 at The Research School of Astronomy and Astrophysics, The Australian National University, Canberra, Australia.

Except where acknowledged in the customary manner, the material presented in this thesis is, to the best of my knowledge, original and has not been submitted in whole or part for a degree in any university.

The three papers presented in this thesis use data from the following instruments: Dark Energy Camera on the 4m Blanco Telescope at Cerro Tololo, Chile; MegaCam on the 6.5m Clay Telescope at Las Campanas, Chile; and AAOmega 2df on the Anglo-Australian Telescope at Siding Springs Observatory, Australia. The data reduction, analysis, writing of the papers and the thesis was performed by the candidate in its entirety, incorporating feedback from co-authors and referees.

Pete B. Kuzma

September, 2017

Acknowledgements

If you had asked me as an undergraduate at the ANU that I would complete a PhD in Astronomy and Astrophysics, I would have dismissed the thought. Yet here we are. The past 4 years have proved to be fun, but difficult. I've experienced so much and have learnt even more. I owe a lot to the staff, both administrative and academic, at Mt Stromlo Observatory and I thank them immensely for their support. I thank my friends and family for their patience as I worked away at this thesis and failed to attend family gatherings and social events. I also thank the Crisp/Shack boys for making sure I did not get too stressed or too complacent with the writing of this thesis.

I would not have reached this stage of my academic career if it were not for Helmut Jerjen. He presented me with the opportunity to perform research as an undergraduate and I would not have continued on without his guidance. Brad Tucker's support through outreach allowed me to focus on something that was not the thesis every once and while.

The students at Mt Stromlo support each other through their studies and without them the PhD journey would not be as enjoyable. I'd like to specifically thank my office mate, Elise Hampton. Our random brainstorming sessions and distracting conversations were always helpful while getting through stressful periods. I have to thank Tammy Roderick, who was instrumental in my thesis. From our observing trip to DECam to discussing/drawing DECam on the white board in your office, your contributions to my thesis was greatly appreciated.

Of course, none of this could be done without the instruction of two specific people. Dougal Mackey, my co-supervisor for my Phd and my Honours supervisor, I owe a lot to. His patience with my silly questions and discussions about our techniques, while in part as the supervisory role, was invaluable. The last, but the most important, person I need to acknowledge is Gary Da Costa. As my primary advisor, his role in my studies was significant. From having incredible patience with me when getting the papers ready for submission, to his support when I presented our work at conferences both local and international, to taking me on as his student, I am greatly thankful for every moment of his time spent helping and guiding me through this journey.

This research is supported by an Australian Government Research Training Program (RTP) Scholarship.

This project includes data gathered with the 6.5 meter Magellan Telescopes located at Las Campanas Observatory, Chile. Australian access to the Magellan Telescopes was supported through the National Collaborative Research Infrastructure Strategy of the Australian Federal Government.

This project used data obtained with the Dark Energy Camera (DECam), which was constructed by the Dark Energy Survey (DES) collaboration. Funding for the DES Projects has been provided by the U.S. Department of Energy, the U.S. National Science Foundation, the Ministry of Science and Education of Spain, the Science and Technology Facilities Council of the United Kingdom, the Higher Education Funding Council for England, the National Center for Supercomputing Applications at the University of Illinois at Urbana-Champaign, the Kavli Institute of Cosmological Physics at the University of Chicago, the Center for Cosmology and Astro-Particle Physics at the Ohio State University, the Mitchell Institute for Fundamental Physics and Astronomy at Texas A&M University, Financiadora de Estudos e Projetos, Fundação Carlos Chagas Filho de Amparo à Pesquisa do Estado do Rio de Janeiro, Conselho Nacional de Desenvolvimento Científico e Tecnológico and the Ministério da Ciência, Tecnologia e Inovacão, the Deutsche Forschungsgemeinschaft, and the Collaborating Institutions in the Dark Energy Survey.

The Collaborating Institutions are Argonne National Laboratory, the University of California at Santa Cruz, the University of Cambridge, Centro de Investigaciones Enérgeticas, Medioambientales y Tecnológicas-Madrid, the University of Chicago, University College London, the DES-Brazil Consortium, the University of Edinburgh, the Eidgenössische Technische Hochschule (ETH) Zürich, Fermi National Accelerator Laboratory, the University of Illinois at Urbana-Champaign, the Institut de Ciències de l'Espai (IEEC/CSIC), the Institut de Física d'Altes Energies, Lawrence Berkeley National Laboratory, the Ludwig-Maximilians Universität München and the associated Excellence Cluster Universe, the University of Michigan, the National Optical Astronomy Observatory, the University of Nottingham, the Ohio State University, the University of Pennsylvania, the University of Portsmouth, SLAC National Accelerator Laboratory, Stanford University, the University of Sussex, and Texas A&M University.

Abstract

Our view and understanding of globular clusters in the Milky Way have undergone massive changes over the past few decades. No longer are globular clusters seen as the perfect example of simple stellar populations, as almost all Galactic globular clusters are now known to contain star-to-star light element abundance variations, and a small subset contain heavy element abundance ranges. However, not only can a lot be learnt from studying the stars within globular clusters, but also from the stars outside globular clusters, beyond the tidal radius. Whether the structure is in the form of tidal tails such as the iconic tails of Palomar 5, or part of a much larger scale stellar feature such as the stellar stream belonging to the disrupting dwarf galaxy Sagittarius or the wealth of streams in the halo of M31, the environs of Galactic globular clusters can be used as insights into the formation of the globular clusters themselves and to the shape and formation of the Milky Way's halo.

This thesis focuses on exploring extended features of Milky Way globular clusters. First, by increasing the spatial coverage and kinematics of the tidal tails of Palomar 5 through low to intermediate resolution spectroscopy from the 2df AAOmega spectrograph on the Anglo-Australian Telescope. We identify 39 new and recover 8 previously determined members in the tidal stream through radial velocities, line strengths and photometric information.

Second, we performed a wide field photometric survey of southern Galactic globular clusters with the complementary imagers MegaCam on the 6.5m Clay Telescope, and the DECam, on the 4m Blanco Telescope. We present the results for the four clusters analysed during the PhD candidature: NGC 1261, NGC 1851, NGC 5824 and NGC 7089 (M2). We find diffuse large low surface density envelopes containing NGC 1261, NGC 1851 and M2, with a tentative detection of an envelope surrounding NGC 5824. We discuss the origins of the envelopes and how the features we have uncovered, along with Palomar 5's tidal tails, may influence our understanding of the Galactic halo and globular cluster formation.

Contents

Declaration iii

Acknowledgements v

Abstract vii

1 Introduction 1

1.1 Galaxy Formation 1

1.2 The Structure of the Milky Way 3

1.2.1 Bulge and the thin/thick disk 3

1.2.2 Galactic Halo 4

1.3 Milky Way Globular Clusters 5

1.3.1 Multiple Populations in Globular Clusters 5

1.3.2 Evolution of Globular Clusters 6

1.3.3 Tidal Tails of Globular Clusters 9

1.4 Globular Clusters and Dwarf Galaxy Accretion 10

1.5 The PhD project 12

2 Palomar 5 and its Tidal Tails: A Search for New Members in the Tidal Stream 15

2.1 Introduction 16

2.2 Observations and Data Reduction 18

2.2.1 Observations and Target Selection 18

2.2.2 Reduction and Techniques 21

2.3 Analysis and Discussion 27

2.3.1 Cluster Members 28

2.3.2 Tidal Tail Members 31

2.3.3 Blue Horizontal Branch Stars 33

2.3.4 Final Tidal Tail Sample 34

2.3.5 Velocity Gradient and Dispersion 35

2.4 Conclusion 38
2.5 Appendix 45
2.6 Addendum 45

3 The Outer Envelopes of Globular Clusters - I 47
3.1 Introduction 47
3.2 Observations and Data reduction 51
3.2.1 Observations 51
3.2.2 Photometry 53
3.2.3 Artificial Star Tests 57
3.2.4 Complete Catalogue 59
3.3 Results 61
3.3.1 Over-density Detection 61
3.4 Discussion 70
3.4.1 Nature of the Substructure Around M2 70
3.5 Conclusions 76
3.6 Addendum 77

4 The Outer Envelopes of Globular Clusters - II 79
4.1 Introduction 80
4.2 Observations and Data reduction 84
4.2.1 Observations 84
4.2.2 Photometry 85
4.2.3 Artificial Star Tests 88
4.2.4 Extinction 89
4.2.5 Complete Catalog 92
4.3 Results 92
4.3.1 Field Identification and Subtraction 92
4.3.2 Radial Density Profile 96
4.3.3 Field Subtraction and 2D Density Distribution 97
4.4 Analysis 101
4.4.1 M2 101
4.4.2 NGC 1851 102
4.4.3 NGC 5824 102

4.4.4 NGC 1261 106
4.5 Discussion 107
4.5.1 Origin of the envelopes 107
4.6 Conclusion 112
4.7 Addendum 114

5 Conclusions **115**
5.1 Future Prospects 119

List of Figures

1.1 The tidal tails of Palomar 5. 10
1.2 The Field of Streams 11
1.3 PAndAS M31 halo map. 13

2.1 Colour-Magnitude Diagram of Palomar 5 21
2.2 Dwarf-Giant Separation in the Palomar 5 sample. 24
2.3 Summed equivalent widths of Ca II triplet against $V-V_{HB}$ for the calibration clusters. 25
2.4 [Fe/H] as a function of the reduced equivalent width belonging to the calibration clusters. 27
2.5 Velocity distributions of stars within a 8.3 arcmin radius of the Pal 5 center. 28
2.6 Same as Fig. 2.3 but for candidate stars outside a 8.3 arcmin radius 29
2.7 Colour-magnitude diagram of Palomar 5 with the corresponding candidate cluster and tidal tail members highlighted. 35
2.8 Spatial distribution of candidate cluster and tail stars along the extent of the tails. 36
2.9 Demonstration of the linear velocity gradient along the tidal tails. 37
2.10 Demonstration of the galactocentric velocity gradient in the tidal tails. . . . 45

3.1 The set of MegaCam and DECam observations of NGC 7089 51
3.2 Example of the cleaning technique used in the reduction pipeline. 55
3.3 Extinction distribution in the MegaCam and DECam observations of NGC 7089 57
3.4 Completeness functions for each of the NGC 7089 observations. 58
3.5 Colour-magnitude diagrams of NGC 7089 59
3.6 Completeness as a function of distance from the center of NGC 7089 60
3.7 The isochrone weighting scheme for NGC 7089 63
3.8 Azimuthally averaged radial density profile for NGC 7089 64

3.9 2-Dimensional density distribution of the MegaCam observations of NGC 7089 67
3.10 2-Dimensional density distribution of the DECam observations of NGC 7089 68
3.11 Location of over-densities that are not physically connected to the NGC 7089 envelope 69
3.12 DECam Colour magnitude diagram of detection 5. 71

4.1 Locations of observations for the three clusters 85
4.2 Completeness curves for NGC 1261,NGC 1851 and NGC 5824 90
4.3 The extinction in the field of view for NGC 1261, NGC 1851, NGC 5824 . . 91
4.4 Colour-magnitude diagrams of the DECam observations for the three clusters 93
4.5 Colour-magnitude diagram of the MegaCam observations for NGC 5824 . . 95
4.6 Isochrone-based weighting scheme for NGC 1261, NGC 1851 and NGC 5824 96
4.7 Radial density profiles for NGC 1261, NGC 1851, NGC 5824 and NGC 7089 98
4.8 2-Dimensional density distributions for NGC 1261, NGC 1851 and NGC 5824 99
4.9 CMD of the extra tidal populations 103
4.10 2-D density distribution of NGC 1851 with a restricted photometric depth . 105
4.11 The flat fields from our DECam and MegaCam observations. 114

List of Tables

2.1 List of Palomar 5 Observations 20
2.2 Comparing the radial velocities of cluster targets identified with those in Odenkirchen et al. (2002) 31
2.3 Comparison of the radial velocities between identified tail members with those presented in Odenkirchen et al. (2009) 33
2.4 A list of all stars determined to be members. The 'New Member' column denotes either the stars discovered here or those known from earlier work (O02 or O09). 40

3.1 Details of the NGC 7089 MegaCam and DECam observations 52
3.2 Parameters of the photometric calibration of NGC 7089 57
3.3 Parameters used to calculate the NGC 7089 2D density maps. 65
3.4 Results of the significance testing procedure for over-densities 70

4.1 List of parameters for the three clusters. 83
4.2 Listing of the DECam observations for NGC 1261, NGC 1851 and NGC 5824 86
4.3 Listing of MegaCam observations for NGC 5824 87
4.4 Photometric calibration parameters for NGC 1261 and NGC 1851 88
4.5 Photometric calibration parameters for NGC 5824 89
4.6 Fitted structural parameters from the LIMEPY surface brightness models . 94
4.7 Paramaters used to calculate the 2-Dimensional density maps for NGC 1261, NGC 1851 and NGC 5824 101
4.8 Details of the clusters and their envelopes 109

Chapter 1

Introduction

For eons, humans have looked to the heavens and have used the stars and planets to guide their way of life. Whether it was worshipping deities or understanding when to plant crops for food, the night sky has always had an important relationship to us. As a result, our inquisitive nature has led us to investigate the night sky, to understand what is out there and how we fit into it all. The science of Astronomy may be as old as human history, but the most ground-breaking discoveries of our Universe have come in the past 200 years. One of the most notable was the discovery that the stars in the night sky are just our own galaxy, called The Milky Way, by Edwin Hubble in 1926 and that there are galaxies beyond our own. The Universe suddenly became infinitely bigger, while we felt infinitely smaller.

Our Milky Way is home to a lot more than just stars. Stellar nurseries, star clusters and smaller galaxies (dwarf galaxies) live throughout and surrounding our Galaxy; each object holding within it details about their own formation and evolution as well as that of their host environment. In fact, the oldest objects in the Milky Way, star clusters known as globular clusters, are treasure troves for information on Milky Way formation and evolution. Many of these spherical, tightly compact groups of near-countless stars hint at some structure beyond their edges. This thesis will explore the outermost regions of globular clusters and beyond, and will discuss what the implications are depending on what features are found.

1.1 Galaxy Formation

The discovery of many different types of galaxies beyond our own brought many new and exciting questions to Astronomers. How all these galaxies formed became an active area of research in the 1960s. Over the decades, different formation theories were proposed, specifically two different approaches. Eggen et al. (1962) proposed that the Milky Way and

its stars and globular clusters all formed out of the same protogalactic cloud: noting that individual stars of lower metallicity were found to move in highly elliptical orbits, while the more circular orbits belonged to the more metal-rich stars. A consequence is that at increasing galactocentric radii, stars become more metal poor – a metallicity gradient. The second approach, one that challenged the theory proposed by Eggen et al. (1962), was a result of a study of Galactic globular clusters performed by Searle & Zinn (1978). After finding no correlation between globular cluster metallicities and galactocentric radii, a result that conflicted with those of Eggen et al. (1962), the authors suggested that the halo (clusters and individual stars alike) formed in their own environments, in protogalactic clouds of different metallicities, and were gravitationally drawn into the Milky Way over an extended period of time. These two theories have now been coalesced into a single, widely accepted model of galaxy formation, one that is consistent with the currently accepted cosmological model, the lambda cold dark matter (ΛCDM) model.

A case was made for the need of a cosmological model that incorporates hierarchical galaxy formation as early as the 1970s (de Vaucouleurs 1970). The two formation scenarios of Eggen et al. (1962) and Searle & Zinn (1978) became amalgamated into the current hierarchical formation picture, a theory that gained much traction from the late 1970s (White & Rees 1978; Blumenthal et al. 1984). The hierarchical model states that the early seeds of galaxies are fed primordial gas through dark matter filaments. Galaxies will then continue to grow in size by accreting smaller protogalaxies that bring with them stars and gas that have evolved in completely different environments. Much more recent studies have provided strong theoretical evidence for the hierarchical model (e.g., Steinmetz & Navarro 2002; Springel et al. 2005), and it has become a widely accepted theory for galaxy formation.

Observationally, the past two decades have been productive in finding evidence for the hierarchical model. Our Galaxy appears to have a number of stellar streams which may be the tidal remains of dwarf galaxies (e.g., see chapter 4 in Newberg & Carlin 2016). The most notable example of which is the Sagittarius stream which originates from the tidal disruption of the Sagittarius dwarf (Ibata et al. 1995). Even our largest galactic neighbour M31 shows evidence of large scale accretion (see section 1.4). Add to that the growing list of massive anomalous globular clusters that have properties that paint them as intruders in the Milky Way's family of globular clusters (see section 1.3.1), the hierarchical formation model of galaxies has received of a lot of observational support. By acknowledging that

the hierarchical formation process may be responsible for the large scale stellar structures in the Milky Way and M31's halos, we can use stellar streams and globular clusters as potential tracers for the accretion events. Mapping globular clusters with connections to different stellar structures will slowly unveil how the Milky Way grew to what we see today.

1.2 The Structure of the Milky Way

A lot of the Milky Way remains not completely understood, despite the fact that we call this galaxy our home. However, Astronomers have still managed to paint a solid picture of the overall structure of the Milky Way. The Milky Way can be split up into multiple components, each with distinctly different stellar populations and properties (see Bland-Hawthorn & Gerhard 2016).

1.2.1 Bulge and the thin/thick disk

The central region of our galaxy is known as the Galactic bulge. The bulge is typically an old, but metal-rich, population, hypothesised to have formed during the early stages of the Milky Way's formation through mergers and *in-situ* (i.e., inside the Milky Way) gravitational collapse. The overall shape of the bulge is somewhat unclear. The Milky Way was originally thought to be a 'classical' bulge, built up through early mergers. However, many studies suggest the bulge follows a boxy/peanut shape (or X-shape), which arises through buckling instabilities in the surrounding disk (Wegg & Gerhard 2013; Vásquez et al. 2013; Zoccali & Valenti 2016, and references therein).

Surrounding the bulge is the disk of the Milky Way, the very feature that gives rise to the notion of a disk galaxy. However, it is not just one component. The disk can be broken down into the thin disk and the thick disk, the properties of the latter are still a matter of debate (e.g., Schönrich & Binney 2009; Bovy et al. 2012). The thin disk has a smaller scale height, $\sim$ 300 pc, when compared to its counterpart; the scale height of the thick disk is at least 1 kpc (Bland-Hawthorn & Gerhard 2016). Conversely, the radial scale length of the thick disk is estimated to be smaller than the thin disk: 2.0 ± 0.2 kpc compared to 2.6 ± 0.5 kpc, respectively. Despite the apparent size difference, the thick disk is considerably fainter, and much more diffuse than the thin disk.

1.2.2 Galactic Halo

The disk is embedded in an envelope of dark matter and diffusely distributed stars known as the Galactic halo. The halo has been traced to at least 100 kpc in radius. Despite its size, the stellar component of the halo is remarkably faint, containing roughly $\sim 1\%$ of the stellar mass of the Milky Way (e.g., Bland-Hawthorn & Gerhard 2016, and references therein). As a result, it is not a simple task to observe the stellar component of halos in nearby galaxies. It has proven to be a substantial task for the Galactic halo too, as we have utilised many large scale photometric surveys, such as the Sloan Digital Sky Survey (SDSS; Fukugita et al. 1996; Gunn et al. 1998; York et al. 2000) and the American Association of Variable Star Observers (AAVSO) Photometric All-Sky Survey (APASS; Henden et al. 2009), to map the halo at varying photometric depths. The stellar component of the Galactic halo (hereafter stellar halo) consists of both individual stars and globular clusters that live at varying galactocentric distances and orbits, with a stellar population that is, on average, old and metal poor (e.g., Mackey & van den Bergh 2005; Carretta et al. 2009). In fact, the Galactic halo may be home to some of the oldest objects in the Milky Way, potentially born at the earliest stages of the Milky Way's formation.

The stellar halo is merely a small part of the Galactic halo, which has a more substantial component hiding in plain sight. It is well established that galaxies have unseen matter contributions to their total mass, as their rotational velocities remain constant at increasing radii (e.g., Freeman 1970; Rubin et al. 1980). This invisible matter was given the name 'dark matter' and the corresponding component of the Galactic halo is appropriately denoted as the dark halo. The Galactic halo (and by extension the Galaxy itself) is dark matter dominated. In fact, dark matter accounts for most of the Galaxy's mass (e.g., Kafle et al. 2014; McMillan 2017). Understanding this component of a galaxy is crucial; as any models of galaxy evolution and formation will need to consider the dark halo effects on other halo components as well its size and shape. As discussed in section 1.1, dwarf galaxies can be accreted onto large galaxies and the interaction can be greatly influenced by the dark halo, dictating the shape that the disrupting system takes during the accretion process (e.g., Law & Majewski 2010b). Modelling disrupting dwarfs galaxies and globular clusters, such as their stream morphologies, can be used to infer properties of the dark halo, such as how much mass it holds and what shape it takes (see section 1.4). Accretion events can remain prominent in the Galactic halo for many Gyrs, depending on the location of the interaction, as the dynamical timescales become longer with increasing galactocentric

distances. This leaves the Galactic halo as a viable place to conduct investigations into the early formation history of the Galaxy.

1.3 Milky Way Globular Clusters

Globular clusters have proved themselves to be invaluable to our understanding of galaxies. These centrally concentrated spherical groupings of stars, are found in abundance in the Milky Way: the present-day population is approximately 160 globular clusters. Globular clusters lie at variable galactocentric distances, ranging between less than one kpc to in excess of 120 kpc. Furthermore, Galactic globular clusters have a variety of metallicities ($-2.5 <$ [Fe/H] < 0), though the typical [Fe/H] abundance is ~ -1.5 (e.g., Carretta et al. 2009). Milky Way globular clusters were thought to be a perfect example of a simple stellar population: stars born at the same epoch out of the same primordial cloud. Consequently, all the stars in a given globular cluster should be chemically homogeneous – a simple stellar population. However, over the past few decades, particularly since the turn of the millennium, globular clusters have been discovered to be not as 'simple' as originally thought.

1.3.1 Multiple Populations in Globular Clusters

Over three decades ago, spectroscopy of red giant stars in different globular clusters began to challenge the 'simple' picture. Knowledge of light element abundance variations goes back to the mid-to-late 1970s and early 1980s (e.g., Harris 1974; Cohen 1978; Cottrell & Da Costa 1981; Norris et al. 1981). As time passed, more light element variations (i.e., anti-correlations between Na-O, C-N and Mg-Al) appeared in different clusters and the size of the sample of clusters with multiple populations grew and grew. The single stellar population view of globular clusters became defunct, and since the turn of millennium, our view of clusters has changed entirely. Many studies since the 2000s have revealed that multiple populations are part of almost all Galactic globular clusters (see the review of Piotto (2009) or a full release from an HST photometric survey of clusters by Milone et al. (2017) and references therein). In fact, only two clusters have been found to be single stellar populations: Rup 106 (Villanova et al. 2013) and IC 4499 (Walker et al. 2011). Despite clusters showing the now standard anti-correlated abundance variations (Kraft 1994; Gratton et al. 2004; Carretta et al. 2010b; Gratton et al. 2012a), the extent of the anti-correlations are mostly unique to each cluster, and the relative amount of stars

belonging to each population in any given cluster is not constant. It remains to this day a puzzle as to how clusters could create such abundance variations.

Some globular clusters show not only light element variances, but also variations in heavy elements. ω Centauri (ω Cen) has been shown to posses at least six sub-giant branches in its colour-magnitude diagram (CMD), corresponding to the different Fe-abundances found within (Bellini et al. 2010; Tailo et al. 2016). Furthermore, ω Cen's giants show variations in s-process elements (e.g., Norris & Da Costa 1995). ω Cen is joined by only a handful of clusters that have similar properties such as NGC 1851 (Milone et al. 2009; Carretta et al. 2010c; Gratton et al. 2012b), NGC 5286 (Marino et al. 2015), NGC 5824 (Da Costa et al. 2014; Roederer et al. 2016), M2 (Yong et al. 2014; Milone et al. 2015) and M54 (Carretta et al. 2010a). It is currently unclear as to why this subset of globular clusters has these peculiar properties. It is worth noting that all these clusters are particularly massive ($> 10^5$ $M_\odot$), therefore it is possible that heavy element abundance variations may be a natural product of massive globular cluster formation. For example, the clusters could be massive enough (or were more massive in the past) so that they were able to hold onto supernovae ejecta from the first generation stars, which supplies heavier elements to enrich the second population of stars (e.g., Parmentier et al. 1999). However, it should be made clear that not all globular clusters with masses $> 10^5$ $M_\odot$ contain internal heavy element variations (e.g., NGC 2808 Milone et al. 2015). Another proposal about these clusters is that they are the stripped cores of dwarf galaxies. This interpretation holds particular relevance, as ω Cen has long been suggested to be the core of an accreted dwarf galaxy (Freeman 1993). Additionally, M54 sits coincidentally at the center of the dwarf galaxy currently being accreted by the Milky Way: the Sagittarius dwarf galaxy (e.g., Da Costa & Armandroff 1995). Globular clusters and their roles in dwarf galaxy accretion will be discussed in depth in section 1.4.

1.3.2 Evolution of Globular Clusters

Despite concerns about their formation, the way globular clusters evolve is well studied and mostly well understood. Over a Hubble time, globular clusters undergo a handful of internal processes that can, in combination with external effects from tidal fields, lead to the dissolution of the cluster. Characteristics such as a cluster size/mass, galactocentric distance and eccentricity of the orbit can all influence how a cluster evolves, with some processes having stronger effects than others depending on the values of these parameters.

The stars in a globular cluster will gravitationally influence each other as they orbit the cluster's center of mass. These interactions will consistently occur, slightly changing each participating star's orbit eventually leading to completely randomised orbits. This process is known as two-body relaxation (see e.g., Spitzer 1987; Binney & Tremaine 2008). The timescale for a cluster to become 'relaxed' (i.e., when all orbits become randomised) is known as the relaxation time. The inner regions of a majority of clusters in the Milky Way are dynamically 'relaxed', as many have relaxation times within the half-mass radius (otherwise known as the median relaxation time) that are much shorter than a Hubble time (e.g., McLaughlin & van der Marel 2005). During relaxation process, stars will interact through an energy equipartition process: stars will transfer energy amongst themselves through passing interactions in an attempt to reach a state of thermal equilibrium within the cluster (Spitzer 1987). As a consequence of the interaction, the higher mass stars or stars with lower energies will slowly populate the inner regions of the cluster, having lost energy in their orbits while the lower mass or more energetic stars will preferentially populate the outer regions of the clusters. This process drives mass segregation in which more massive stars are relatively more frequent in the inner regions and less frequent in the outer regions in comparison to less massive stars (e.g., Spitzer 1987; Meylan & Heggie 1997).

The effects of mass segregation can continue even beyond the point a cluster becomes 'relaxed'. Stars will continue to undergo two-body interactions, continuously moving low energy stars towards the cluster center with the high energy stars becoming more populous in the outer regions. This process has been understood as a cluster approaching equipartition of kinetic energy. However, no globular clusters will ever reach complete equipartition. Despite losing energy in the two-body interaction, stars in the inner regions will move to more tightly bound orbits, increasing the overall kinetic energy. This is opposite to the processes expected in equipartition (e.g., Trenti & van der Marel 2013). Stars in the inner regions will continue to pass kinetic energy to the stars in the outer regions of the cluster through two-body interactions, and will again find themselves on even tighter orbits. This results in an increase of kinetic energy once more. The energy transfer process will continuously repeat itself, moving mass consistently towards the center of mass (e.g., Lynden-Bell & Wood 1968; Lynden-Bell & Eggleton 1980). It is clear that a run-away effect is occurring here, and it is given the name 'core-collapse' . The core of the cluster will continue to shrink as the energy is passed from the core to the stars in the outer

regions (e.g., Chernoff & Weinberg 1990). To stop the collapse, the core requires a way to create more energy than what is being taken away. A common suggestion is that the core receives energy through stars in binaries (Heggie & Aarseth 1992; McMillan & Hut 1994). Whether the binary systems are primordial or formed through interaction in the compact core of the cluster, the binding energy increase by the tightening of the binaries, or even three-body interactions, can supply the core with enough energy to halt the collapse. The time scale for core collapse is different from cluster to cluster, with many properties like the initial mass function or total number of stars in the system affecting the rate of collapse. Estimates place core collapse occurring on the order of 300 times the central relaxation time (e.g., Takahashi 1995; Binney & Tremaine 2008).

While core collapse is occurring in the center of the cluster, stars in the outer regions continue to gain energy. The extra energy in the orbits will take stars further and further away from the central regions of the cluster. If a globular cluster is in an isolated environment (i.e., a quasi-static state), this can create a diffuse stellar envelope surrounding the central core. An envelope created this way has an hypothesised radial density profile that, at large radii, follows a power law, $\rho \sim r^{-3.5}$ (see Spitzer 1987). However, no clusters are known to evolve in an isolated environment. All known globular clusters are within a galaxy, within a tidal field. The effects of the tidal field on the cluster itself can greatly effect the cluster's evolution, with different processes contributing towards dissolution. Once such process is tidal evaporation. Evaporation occurs as the most energetic stars are accelerated to the point where they can escape from the cluster: their radial distance from the cluster center exceeds the radius where the tidal forces between the globular cluster and the Galactic halo are in balance. This radius is known as the tidal radius. Additionally, a cluster can be severely damaged by a relatively short duration but significant addition of energy from bulge and disk passages, "shocking" the cluster (e.g., Gnedin et al. 1999). These tidal shocks inevitably hasten the evaporation process. The rate that evaporation occurs, or the destruction rate, varies from cluster to cluster as properties such as mass and orbit are major factors when considering destruction rates (e.g., see Dinescu et al. 1999; Allen et al. 2006). As some of the destruction rates presented in Gnedin & Ostriker (1997) are less than a Hubble time, the current globular cluster population could be a small subset of the initial one.

1.3.3 Tidal Tails of Globular Clusters

As previously discussed, globular clusters evolving in a tidal field undergo constant stress from Galactic forces. Stars that get sufficiently "excited" due to either internal or external events begin to populate the outer regions of cluster, within the tidal radius. The stars that find themselves in these outer regions are typically of low mass, due to the dynamical events discussed in the previous section. As stars begin to gather near the tidal radius, they form a faint stellar envelope until they approach the Lagrange points, the points of neutral gravitational influence (e.g., Küpper et al. 2010b). This can be seen as an excess above any density models (e.g., King 1966 or Wilson 1975 models) in outer regions of the density profile (e.g., Johnston et al. 1999; Testa et al. 2000). When at the Lagrange points, stars can now leave the cluster. As the stars escape, they form two coherent co-moving structures extending from the cluster. These long two-arm structures are denoted as tidal tails.

Tidal tails are powerful tools for understanding the nature of the Galactic halo. The formation, shape and asymmetry of the tidal debris that globular clusters can develop in their outer regions depends on the nature of the tidal field in which the cluster is located. Tidal tails, therefore, have potential to constrain properties of the Galactic halo, such as mass enclosed and potential substructure (e.g., Dehnen et al. 2004; Mastrobuono-Battisti et al. 2012; Bonaca et al. 2014; Pearson et al. 2015). There are a small group of clusters with observed tidal tails (e.g., Grillmair & Johnson 2006), and there is a larger group of clusters that show evidence of cluster-like stellar populations beyond the tidal radius (e.g., Grillmair et al. 1995; Leon et al. 2000). There is no set of tails studied more than the elegant tidal tails belonging to Palomar 5.

The low mass cluster, Palomar 5 (Pal 5) was found to possess extensive tidal tails by Odenkirchen et al. (2001) in the Sloan Digital Sky Survey. Revisiting the tails, Odenkirchen et al. (2003) (Fig. 1.1) measured the length of the tails to be 10° of arc. The tails are now known to extend over at least 23° of arc (Grillmair & Dionatos 2006). The tails are suggested to contain at least 1.2 times more stars, hence more stellar mass, than the cluster itself, hinting that Pal 5 has undergone substantial mass-loss in the creation of these tails (Odenkirchen et al. 2003). Consequently, Pal 5 will most likely be completely destroyed on its next passage through the disk (Odenkirchen et al. 2003; Dehnen et al. 2004). As the poster child of disrupting globular clusters, many studies have modelled the tails and have attempted to estimate properties of the Galactic halo, such as mass contained

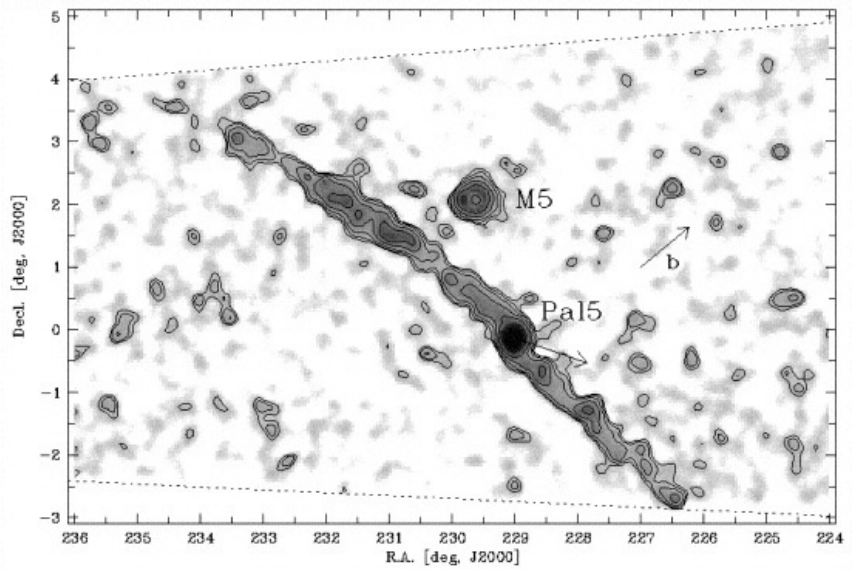

Figure 1.1: The tidal tails of Palomar 5. (Odenkirchen et al. 2003)

within the current galactocentric radius of Pal 5 and the existence of dark-matter sub halos, with results differing between each research group (see e.g., Mastrobuono-Battisti et al. 2012; Bonaca et al. 2014; Pearson et al. 2015).

1.4 Globular Clusters and Dwarf Galaxy Accretion

As was mentioned in section 1.3.1, there are Milky Way globular clusters that may not have formed *in-situ*, in the Milky Way. Searle & Zinn (1978) hypothesised that, potentially, a generous subset of clusters may have formed in dwarf galaxies before being accreted into the Galactic halo. The authors came to this conclusion after finding no relationship between the metallicities and galactocentric distances for globulars, which is contrary to the predictions of the primordial cloud collapse model of galaxy formation. The accretion model is consistent with the expectations of galaxy formation in the ΛCDM cosmology, but accretion in action in the Galactic halo was not observed until a major serendipitous discovery in mid 1990s.

The 'smoking gun' for Searle & Zinn (1978) hierarchical accretion model was the discovery of the active accretion of the Sagittarius dwarf galaxy onto the Milky Way. While completing a spectroscopic study of the outer regions of the Galactic bulge, Ibata et al. (1994) discovered a significant kinematic signature, unlike anything they were expecting. This was the first detection of the Sagittarius dwarf galaxy. In the matter of a decade, the debris of the disrupting dwarf was traced entirely around the Milky Way, in the form

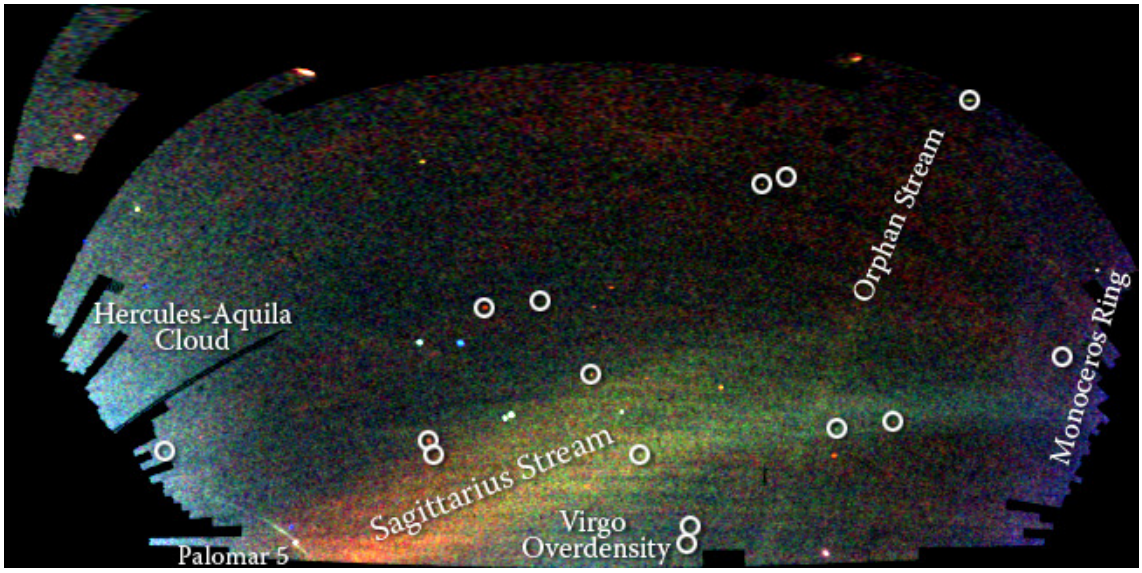

Figure 1.2: The Field of Streams from the Sloan Digital Sky Survey. Note the significant Sagittarius stream across the center and the Palomar 5 tidal tails in the lower left hand corner (Belokurov et al. 2006b).

a thick stellar stream (Fig. 1.2) (Majewski et al. 2003). It is worth noting that, just as with tidal tails like Pal 5, the larger streams from accreted dwarf galaxies such as Sagittarius can also be used to constrain the potential of the Milky Way. There are issues with this process, however. Law et al. (2010) modelled the disruption process of Sagittarius successfully with triaxial potential model for the Milky Way (Law et al. 2009), but this model for the potential does cause problems when used to produce thin tidal tails such as those observed for Pal 5. In particular, models of the Pal 5 tails with the triaxial potential showed that the tails fan out with increasing distance from the cluster, which is in contrast to actual shape of the tails (Pearson et al. 2015). Further, the triaxial potential itself is likely to be unstable (e.g., Binney 1981).

Interestingly, Sagittarius was found to be bringing along a number of globular clusters with it. To date, four globular clusters have been confidently attributed to the disrupting dwarf (see e.g., Law & Majewski 2010a). Those are M54, Terzan 7, Terzan 8 and Arp 2 (Da Costa & Armandroff 1995). While not directly located on the stream, Palomar 12 has been linked to Sagittarius (Martinez Delgado et al. 2002), as has Whiting 1 (Carraro et al. 2007). A number of other clusters have been postulated to be part of the Sagittarius, but their link remains tentative (AM-4, NGC 5053 and NGC 5634; Carraro 2009; Sbordone et al. 2015). M54 sits at the centre of the Sagittarius debris, and it is commonly referred to as being the nucleus of the dwarf. The abundance patterns, multiple stellar populations and other similarities that M54 has with ω Cen, also reflect this possibility (e.g., Layden

& Sarajedini 2000; Siegel et al. 2007; Bellazzini et al. 2008; Carretta et al. 2010a).

Meanwhile, the globular cluster system and halo environment of M31, the other large disk galaxy in the Local Group, is remarkably different. The Pan-Andromeda Archeological Survey (PAndAS; McConnachie et al. 2009) has revealed the extent of a large globular cluster population in the outer halo. Between a radius of 25 kpc to $\sim$ 150 kpc, the newly discovered globular clusters, $\sim$ 90 in total, raise the known number of M31 globular clusters to over 500 (e.g., Huxor et al. 2014). This is nearly triple the size of the Milky Way globular cluster population. The PAndAS team have also discovered that the M31 halo is littered with large scale streams and over-densities. Many of these substructures in the M31 halo have globular clusters identified as members (Fig. 1.3) through statistical means (e.g., Mackey et al. 2013; Veljanoski et al. 2014). More direct links have been established, however; Mackey et al. (2014) linked two globular clusters, PA-7 and PA-8, with the South West Cloud through consistent kinematics and metallicities. The combination of PAndAS findings and Sagittarius with its own set of globular clusters suggest that there is a strong connection between the accretion merger process and globular clusters.

1.5 The PhD project

The shape of the Galactic halo is under much debate, notwithstanding the models reproducing the multiple tidal streams that the Galactic halo holds. One thing is abundantly clear however, stellar streams and tidal tails are the keys to fully understanding many properties of the Milky Way. As globular clusters are a common thread between both the larger stellar streams and the smaller tidal tails, they, too, can play a pivotal role in the task of understanding the Galactic halo. The goal of this thesis is to supply important information about the outer structures of globular clusters through two studies. First, by measuring and investigating the kinematics in the tidal tails of Palomar 5 over a spatial coverage much larger than any previous study. Second, by searching for more extended structures in the environs of outer halo globular clusters.

Previously, the only kinematic study of the Pal 5 tidal tails was completed by Odenkirchen et al. (2009), covering roughly 9.5° of arc. However, the known length of the tails is over 20°. Increasing the kinematic coverage of the tails would provide modellers with extra ammunition to define and constrain the orbit/formation of the tidal tails and, ultimately, the galactic potential that allows such a structure. In Chapter 2, a spectroscopic analysis of giant stars along the tidal tails of Pal 5 is presented. An extent of 23°

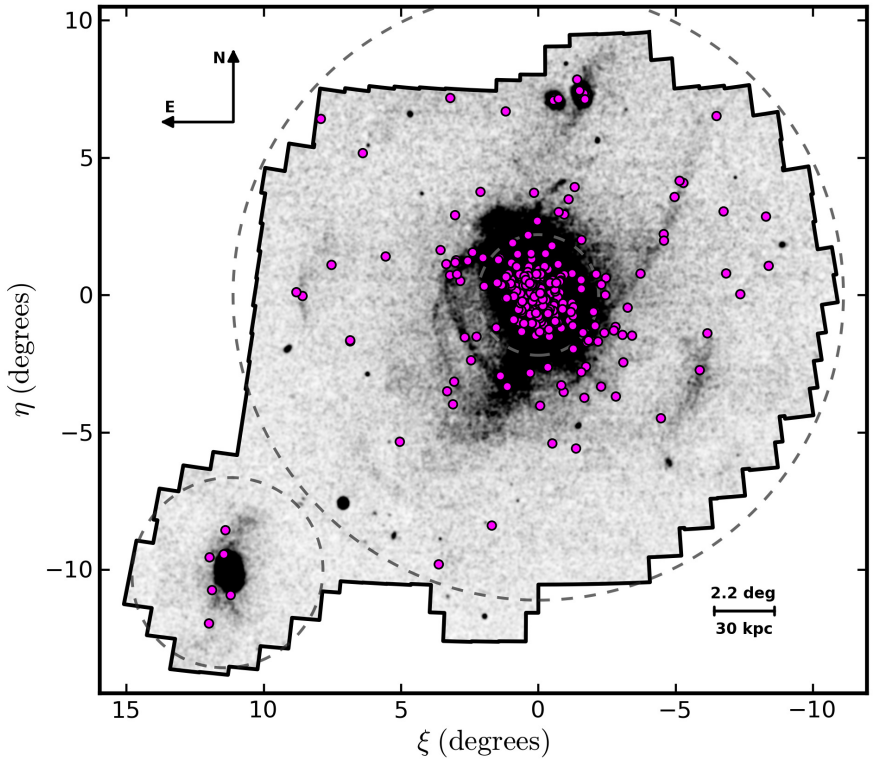

Figure 1.3: The latest update of the map of the M31 halo as measured from PAndAS in Mackey et al. (2010b). The magenta points indicate globular clusters. The inner dashed circle indicating a scale radius of 25 kpc while the outer dashed ring indicates a scale radius of 150 kpc. M33 is surrounded by a ring of scale radius 50 kpc.

across the leading and trailing tails is covered, and 67 giant stars (47 newly discovered) in the cluster and tidal streams are identified. These were discerned from contaminating field stars through metallicities, surface gravities and kinematics.

The second study aims to uncover what kind of extended structures lie undiscovered around outer halo globular clusters. As previously addressed in this chapter, a lot of unresolved questions remain in regards to the Galactic halo, such as shape and formation. Further questions arise when comparing the Galactic halo and the halo of M31. For example, why does the M31 halo appear to have substantially more large scale sub-structure compared to the Milky Way? The common factor for all of these issues are globular clusters. Uncovering more tidal tails, larger scale stellar streams that may relate to accreted dwarf galaxies, or some other kind of extra tidal structure (e.g., a stellar envelope as found around NGC 1851; Olszewski et al. 2009), will provide great aid to answering these puzzling questions. Chapters 3 and 4 present the results of a wide-field photometric survey of

outer halo globular clusters. We present the results for four clusters, out of a sample of 25, which hint that some kind of extended structure exists beyond the cluster tidal boundary. The clusters are NGC 1261, NGC1851, NGC 5824 and NGC 7089 (M2). We find that M2, NGC 1261 and NGC 1851 are embedded in low-surface brightness stellar envelopes and NGC 5824 appears very extended with a tentatively detected envelope. We go on to discuss the implications of our findings. Chapter 5 contains a concluding discussion, as well as a discussion about the future work planned for a wide-field photometric survey of outer halo globular clusters.

Chapter 2

Palomar 5 and its Tidal Tails: A Search for New Members in the Tidal Stream

This chapter is based on the published article "Palomar 5 and its Tidal Tails: A Search for New Members in the Tidal Stream", P. B. Kuzma, G. S. Da Costa, S. C. Keller, E. Maunder, 2015, Monthly Notices of the Royal Astronomical Society, 446, p.p. 3297. Minor typographical and grammatical changes have been made as a result of the Examiner Reports. Significant alterations to the original text, as suggested from the Examiner Reports, are shown in italics.

In this chapter we present the results of a search for members of the globular cluster Palomar 5 and its associated tidal tails. The analysis has been performed using intermediate and low resolution spectroscopy with the AAOmega spectrograph on the Anglo-Australian Telescope. Based on kinematics, line strength and photometric information, we identify 39 new red giant branch stars along ~20° of the tails, a larger angular extent than has been previously studied. We also recover eight previously known tidal tail members. Within the cluster, we find seven new red giant and one blue horizontal branch members and confirm a further twelve known red giant members. In total, we provide velocity data for 67 stars in the cluster and the tidal tails. Using a maximum likelihood technique, we derive a radial velocity for Pal 5 of -57.4 ± 0.3 km s^{-1} and a velocity dispersion of 1.2 ± 0.3 km s^{-1}. We confirm and extend the linear velocity gradient along the tails of 1.0 ± 0.1 km s^{-1} deg^{-1}, with an associated intrinsic velocity dispersion of 2.1 ± 0.4 km s^{-1}. Neither the velocity gradient nor the velocity dispersion appear to change with angular distance from the cluster. Our results verify the tails as kinematically cold structures and

will allow further constraints to be placed on the orbit of Pal 5, ultimately permitting a greater understanding of the shape and extent of the Galaxy's dark matter halo.

2.1 Introduction

The globular clusters (GCs) of the Milky Way have proven to be treasure chests of invaluable information about the Galactic halo. These stellar systems are self-gravitating groups of similar stars, in both age and metallicity. Stars that reside in the outer regions of a cluster are sensitive to the gravitational tidal field of the Galaxy, and if the cluster potential is overcome, the stars can be lost from the cluster to the halo field. The distance from the cluster centre at which the gravitational forces are balanced is known as the tidal radius, r_t. The fitting-formulae of King (1962) and more sophisticated modelling (e.g., McLaughlin & van der Marel 2005) have provided reasonable estimates of the tidal radius for a number of GCs. However, some clusters do not exhibit a classic tidally-limited profile, revealing instead "extra-tidal" features. For example, Grillmair et al. (1995) showed through star counting techniques the existence of clusters that have density profiles extending well beyond the limiting radii set by the best-fit King profile. These extra-tidal features are generally indicators of a significant loss of stars from the cluster as a result of tidal interactions with the Galaxy, potentially leading to the complete disruption of the cluster. The escaping stars form leading and trailing streams (tidal tails) generally aligned with the orbit of the cluster[1]. Consequently, the tidal tails present a prime opportunity to further define the orbit of the parent cluster, which in turn allows constraints to be placed on the potential field of the Galaxy's dark matter halo.

Amongst the Galactic globular clusters with extra tidal features, Palomar 5 (Pal 5) stands out. At a distance of 23.2 kpc from the Sun (e.g., Mastrobuono-Battisti et al. 2012), the cluster has a number of characteristics (low luminosity, low central concentration and low velocity dispersion) that made it a perfect candidate for a cluster undergoing tidal disruption. Odenkirchen et al. (2001) uncovered the presence of substantial tidal tails through spatial analysis techniques utilizing the extensive photometry provided by the Sloan Digital Sky Survey (SDSS; Gunn et al. 1998; Fukugita et al. 1996; York et al. 2000; Yanny et al. 2009b). Later data releases of the SDSS allowed additional analysis: Grillmair & Dionatos (2006), following similar techniques to Odenkirchen et al. (2001), extended the

[1] *This is due to the Coriolis acceleration, which becomes dominant at great distances from the cluster center. Closer to the cluster, tidal tails follow the shape of the parent clusters' Roch lobe, which is affected by the pull of the host galaxy's potential.*

definition of the trailing tail to roughly 16° from the cluster centre and that of the leading tail to ~6°, at which point the SDSS coverage ends. With further analysis, the trailing tail has now been shown to span at least 23° from the cluster centre, where again the limits of the SDSS survey area are reached (Carlberg et al. 2012).

The discovery of the tails spurred further study of Pal 5. For example, Koch et al. (2004) noted that the luminosity function (LF) of Pal 5 in the cluster core is flatter than the LF in the outer regions. This indicates that the core of Pal 5 lacks low mass stars as result of dynamically driven mass segregation. Koch et al. (2004) also investigated the LF of the tails, noting that it is comparable to that for the outer regions of cluster. These results complement those of Odenkirchen et al. (2003) who report that the mass in the tails is greater than the mass remaining within the cluster. It is likely that another passage of Pal 5 through the disk of the Galaxy will prove to be the final one before the cluster is completely disrupted (Odenkirchen et al. 2003).

In this respect Dehnen et al. (2004) completed a large number of N-body simulations of clusters travelling along an orbit analogous to that of Pal 5 in the potential of the Milky Way. The simulations showed that clusters with similar properties to Pal 5 would create tidal tails from multiple passages through the disk of the Galaxy, and that these disk crossings can eventually lead to the complete dissolution of the cluster. Indeed these simulations predict the complete destruction of Pal 5 at its next disk crossing.

Nonetheless, the simulations failed to produce some of the structure seen within the Pal 5 tails. In particular, as first noted by Odenkirchen et al. (2003), the tails display a series of inhomogeneities along their length, visible as regions of higher and lower density (see also Grillmair & Dionatos 2006; Jordi & Grebel 2010). Carlberg et al. (2012) suggested that the inhomogeneities may have been created by the interaction of the stream with dark matter sub-halos present in the Galactic halo, potentially providing an important probe of the predictions of the standard ΛCDM model for the Galaxy (Ngan & Carlberg 2014 and references therein). However, Mastrobuono-Battisti et al. (2012) showed through detailed *N*-body simulations that the clumps and gaps can also result from the epicyclic motion of the stars in the tidal tails. The question has been further investigated with the simulations performed by Ngan & Carlberg (2014). These showed that in a ΛCDM Milky Way dark matter halo model, gaps in tidal streams can be caused by both purely epicyclic motions and by sub-halo interactions, with the presently available data unable to definitely distinguish between the possibilities. Most recently, Pearson et al. (2015) found

that the thin shape of the tails can be successfully reproduced in spherical dark matter halo potentials. However, they found this is not the case for the triaxial potential proposed by Law & Majewski (2010b) to describe the properties of the Sagittarius stream.

The kinematics of the cluster itself have been studied by Odenkirchen et al. (2002) (hereafter O02). O02 found the heliocentric velocity of the cluster to be -58.7 ± 0.2 km s^{-1} with a notably small velocity dispersion of 1.1 ± 0.4 km s^{-1}. Subsequently, Odenkirchen et al. (2009, O09) provided a kinematic analysis of individual stars in the tails of Pal 5. Seventeen stars were determined to be members of the tails based on their line-of-sight velocities. As for the cluster the tails were shown to have a low velocity dispersion: $\sigma < 5$ km s^{-1}. Such a low dispersion is a defining characteristic of a kinematically cold structure. The velocities of the stars along the tails also revealed a velocity gradient of $\sim$1 km s^{-1} deg^{-1}. These results suggested a revision of the orbit of Pal 5, and O09 further found that the results are best interpreted if the tails do not align exactly with the orbit of Pal 5, contrary to earlier indications (Odenkirchen et al. 2001). O09 point out the need for additional kinematic information at larger distances along the tail to further constrain the simulations of the orbit. Lux et al. (2013) reach similar conclusions.

In this paper we present a self-consistent analysis to identify additional members of Pal 5 and of its tidal tails. In particular we explore the full 20° extent of the tails presented in Grillmair & Dionatos (2006). In the following section we describe the observations and the analysis techniques employed. In section 3 we discuss our results, first for the cluster and then for the stars in the tidal tails. Section 4 contains our concluding comments.

2.2 Observations and Data Reduction

2.2.1 Observations and Target Selection

The observations employed for this work were taken with the Anglo-Australian Telescope (AAT) at Siding Spring Observatory (SSO), using AAOmega, a multi-fibre, dual-beam spectrograph that utilizes the two degree Field (2dF) fibre-positioning system[2]. The system can allocate up to 392 fibres allowing simultaneous observations of both science targets and sky regions across a 2° diameter field-of-view. The light fed into the spectrograph is split into the red and blue arms by a dichroic centred at 5700Å. This work makes use of a number of observations performed across five years. These include our own observations

[2]Manuals and technical information at `http://www.aao.gov.au/2df/aaomega/`

from 2009 and 2010, as well as a set from 2006 (PI: Lewis) obtained from the AAT archive. In the 2006 June observations, 14 2dF configurations were observed over five nights at nine distinct field centres spread along the leading and trailing tails. The total integration time per configuration was 3×30 min. For this run the red arm of AAOmega was configured with the 1700D grating and the blue arm with the 2500V grating. The red arm spectral coverage was 8450 – 9000Å at a resolution of $\mathcal{R} \approx 10000$ while for the blue arm the coverage was 5280 – 5630Å at $\mathcal{R} \approx 8000$.

The second set of observations took place in 2009 March and April. Completed during service observing runs, AAOmega was configured with the 1000I grating (spectral range: 8000 – 9500Å with a coverage of 1100Å, $\mathcal{R} = 4400$) in the red arm and the 580V grating (spectral range: 3700 – 5800Å full coverage, $\mathcal{R} = 1300$) in the blue arm. In 2009 March single configurations were observed at two field centres while in 2009 April two configurations were observed at a field centre located in the leading tail. The integration times were 3×20 min for the March observations and 2×20 min for the April set. The final set of observations used for this work took place in 2010 May, with AAOmega configured with the 1700D (red arm) and 580V (blue arm) gratings. Single configurations at two field centres were observed with integration times of 3×20 min and 4×20 min, respectively. Overall each 2dF configuration typically consisted of approximately 330 targets together with 30 fibres allocated to blank sky regions. Table 2.1 gives an overview of all the observations used in this work; the total number of stars observed was 4507.

The selection of stars targeted for observation with 2dF varied across the different runs, and this is illustrated in Fig. 2.1. Both panels display the reddening corrected colour-magnitude diagram (CMD) for Pal 5 generated from the SDSS DR10 photometry of Ahn et al. (2014). Only stars within 8.3′ of the cluster centre are plotted and the reddening corrections made use of the dust maps available from Schlegel et al. (1998). In the left panel the approximate region used for target selection for the 2006, 2009 March and 2010 May observations is delineated, while the right panel shows the approximate target selection region for the 2009 April run. The reddening corrections to the SDSS photometry were small, as there is little variation from the cluster value of $\mathrm{E}(B-V) = 0.06$ (Schlegel et al. 1998) across the regions of the tidal tails studied.

Table 2.1: List of observations. Fields have been named 1 -11 based on increasing R.A.

Field Name	Mean Field Center		Date-obs	# of config.	# of exp.	Exp. Time	Red Grating	Blue Grating
	R.A (J2000)	Dec (J2000)	mm/year			per Obs. (s)		
F1	15:09:44.89	–01:48:00.1	04/2009	2	2	1200	1000I	580V
F2	15:10:00.57	–01:29:58.5	06/2006	1	3	1800	1700D	2500V
F3*	15:15:59.93	–00:06:37.4	06/2006	3	3	1800	1700D	2500V
			03/2009	1	3	1200	1000I	580V
F4*	15:17:59.67	00:19:59.6	06/2006	1	3	1800	1700D	2500V
			05/2010	1	3	1200	1700D	580V
F5	15:23:59.97	01:30:00.1	05/2010	1	4	1200	1700D	580V
F6	15:31:59.37	03:29:54.9	06/2006	1	3	1800	1700D	2500V
			03/2009	1	3	1200	1000I	580V
F7	15:40:00.17	04:00:01.3	06/2006	2	3	1800	1700D	2500V
F8	15:48:01.19	04:41:55.6	06/2006	1	3	1800	1700D	2500V
F9	15:56:00.82	05:30:03.3	06/2006	2	3	1800	1700D	2500V
F10	16:03:12.70	06:30:01.6	06/2006	2	3	1800	1700D	2500V
F11	16:16:49.07	07:47:55.2	06/2006	1	3	1800	1700D	2500V

* These fields contain the cluster centre.

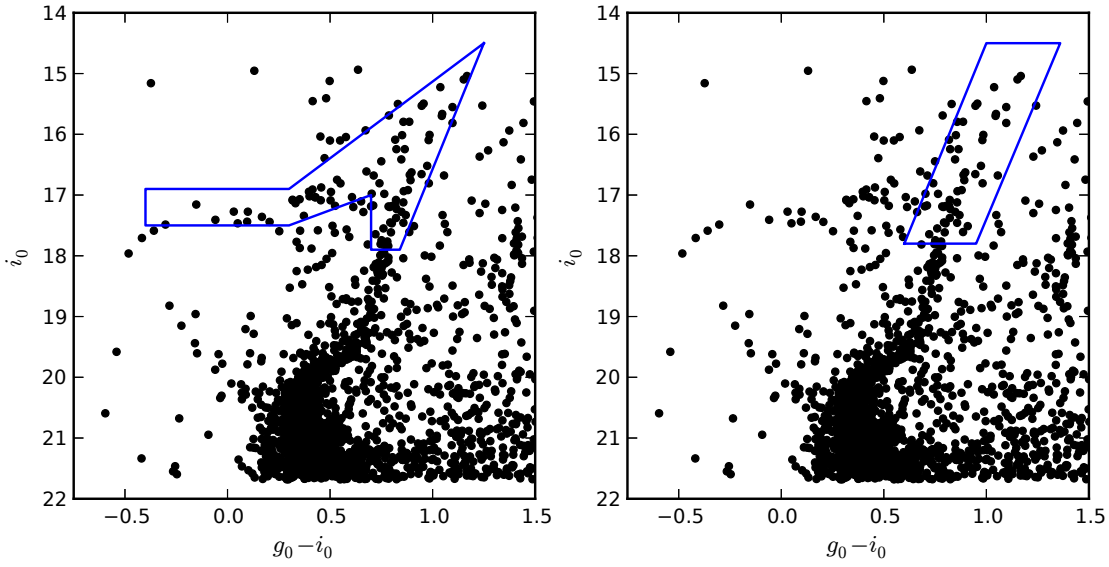

Figure 2.1: Both panels show a dereddened colour-magnitude diagram for Pal 5 using photometry from SDSS DR10 (Ahn et al. 2014). Only stars within 8.3′ of the cluster centre are plotted. In the left panel the blue polygon outlines the approximate target selection region for the observations conducted in 2006, 2009 March and 2010 May. The right panel shows the target selection region for the 2009 April observations.

2.2.2 Reduction and Techniques

Once the data had been extracted from the AAT archive, it was reduced using the 2dF data reduction pipeline, 2dfdr[3]. The approach was the standard one using fibre flats to set the location of the spectra, and arc lamp spectra for the wavelength calibration. The relative throughput of the fibres, necessary for the sky subtraction, was determined using the *SKYFLUX(MED)* approach, which determines the relative throughputs from the observed intensities of night-sky emission lines. At the end of the process the wavelength-calibrated sky-subtracted spectra from the individual integrations were median-combined to remove any cosmic-ray contamination. Typical signal-to-noise ratios (S/N) range from 15 to 70 pixel^{-1} in the vicinity of the Ca II triplet for the red spectra, and 10 to 40 pixel^{-1} in the vicinity of the Mg I lines in the blue-arm spectra.

Radial Velocities

The radial velocities of the stars were calculated from the red arm spectra via cross-correlation using the **IRAF**[4] routine *fxcor*. The template used for the correlation was

[3]Visit `http://www.aao.gov.au/2df/aaomega/aaomega_2dfdr.html` for more information
[4]Information and distribution of IRAF is available through `http://iraf.noao.edu/`.

an AAOmega 1700D grating, high signal-to-noise (>100) spectrum of the F6V star HD 160043 taken as part of the program described in Da Costa (2012). The strength of the Ca II triplet lines in this star match well with those in the program object spectra. The spectra were correlated over the wavelength interval $8450\text{Å} < \lambda < 8700\text{Å}$, a region relatively uncontaminated by night-sky emission line residuals. Heliocentric velocities of the targets were calculated with the **IRAF** command *rvcorrect*, and, as discussed in Da Costa (2012), the uncertainty in the zero point of the radial velocity system is ±0.8 km s^{-1}. Stars that had low correlation peak heights (<0.5) and/or high uncertainties in the correlation velocity (>5 km s^{-1}) were discarded from the subsequent analysis – generally these were spectra with low signal-to-noise.

A number of stars were observed across multiple fields. We used these multiple observations to estimate the overall accuracy of the velocities returned by the *fxcor* routine. The mean velocity of stars with two or more observations was calculated using the output errors of *fxcor* as weights. The corresponding estimate of the error for a single observation was then evaluated using the small number statistics formalism of Keeping (1995), which utilizes the range of the observations. In particular, the estimated standard deviation for a single observation is given by:

$$\sigma = R \times q_N \tag{2.1}$$

where R is the range in N observations and q_N is a multiplicative factor (e.g., $q_2 = 0.886$ and $q_3 = 0.591$). We then compiled these error estimates as a function of the median signal in the continuum region between the stronger Ca II lines, finding that for stars with a median continuum level above 1200 ADU the single observation error estimate was less than 1 km s^{-1}. As the continuum level decreases, the velocity error increases towards 2 km s^{-1} at continuum levels ∼700 ADU and then increases rapidly to ∼4 km s^{-1} at ∼200 ADU. These results are consistent with those of Da Costa (2012) who used a similar instrumental setup and analysis technique. We employed this (σ_v, continuum level) relation to generate the velocity uncertainty estimates for stars with only one observation. For stars with multiple observations the estimate was reduced by the square-root of the number of observations.

Photometric Discrimination

Although the primary targets were the stars in the selection boxes shown in Fig. 2.1, the actual observations included stars with a broader range of colours so that as many of the

available 2dF fibres were allocated as possible. However, no unusual stars were discovered, and since there is no reason to expect any Pal 5 tidal tail stars to lie significantly away from the principle sequences in the CMD, in the subsequent analysis we focus only on those stars that lie relatively near to the Pal 5 sequences in the CMD. A routine was created to remove stars from the data set if their CMD location did not lie within a polygon encompassing the Pal 5 CMD features, similar to that shown in the left panel of Fig. 2.1.

Giant/Dwarf discrimination

The principle contaminant in the fields containing the Pal 5 cluster and tidal tail stars, which are giants, are foreground dwarfs of approximately solar metallicity. A means of distinguishing these stars from the potential cluster and tidal tail members is therefore needed. We adopt a similar approach to that of Battaglia & Starkenburg (2012), which employs the gravity sensitivity of the Mg I line at λ8807Å, a line which is stronger in dwarfs than in giants of similar temperature and metallicity. The discrimination is aided by the fact that the Pal 5 giants are also metal-poor compared to the vast majority of field dwarfs. In left panel of Fig. 2.2, we show the relationship between the equivalent width (EW) of the Mg I λ8807Å line and the sum of the EWs of the two stronger Ca II triplet lines at $\lambda\lambda$8542 and 8662Å for the stars in the two fields which contain the cluster centre. The EW measurements were made using the routine *splot* in **IRAF**. The uncertainties in the line strengths were estimated from the stars with multiple observations and are typically 0.15Å in size. We also identify in the Figure stars that lie within our adopted radius for Pal 5 (8.3′; see §2.3) and within the velocity range encompassing cluster members. As expected, these probable giant stars occupy the lower part of the relationship. We therefore classify as dwarfs those stars with Mg I λ8807Å EWs exceeding 0.4Å, and apply this discriminant to all the observations for which the strength of this feature can be measured. The adopted value generates a substantial sample of candidate cluster and tidal tail stars while minimizing the contamination from field dwarfs. It is consistent with the results of Da Costa et al. (2014) who used a similar approach and a value of 0.35Å for the giant/dwarf discrimination. Our value is also broadly consistent with the approach used in Casey et al. (2013). For those stars in our sample where the S/N of the spectrum was too low to allow a reliable measurement of the Mg I line strength, an upper limit *of 0.14Å* for the EW value was adopted.

Wherever the 1700D filter was not available, the Mg I triplet at $\sim \lambda$5180Å observed

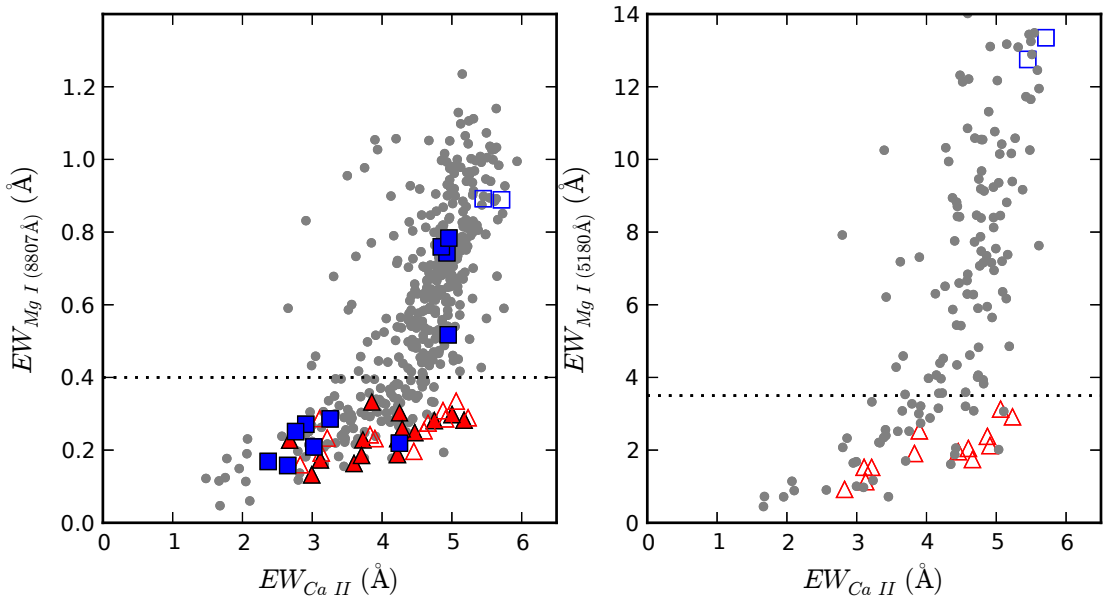

Figure 2.2: Left panel: Equivalent width (EW) of the λMg I 8807Å line as function of the sum of the EWs of the Ca II triplet lines at $\lambda\lambda$8542 and 8662Å for stars in fields F3 and F4, which contain Pal 5. Stars that lie beyond the adopted radius of the cluster (8.3′) are plotted as grey points. Blue squares show stars within the adopted cluster radius but outside the velocity range −65 to −50 km s^{-1}, while red triangles show stars within the adopted radius and within the velocity range. In both cases open symbols are used for stars that are also plotted in the right panel. Right panel: EW of the Mg I triplet features at $\lambda\lambda$5172Å plotted against the summed EW of the Ca II triplet lines, using the same symbols as for the left panel. The dotted line in both panels shows the Mg I EW values used to separate dwarfs from giants.

in the 580V grating in the blue arm was utilized. These features can also provide gravity discrimination (e.g., Casey et al. 2013). We therefore measured the total EW of the Mg I triplet lines and the resulting relation between the Mg I line strengths and the Ca II triplet EW is shown in the right panel of Fig. 2.2. Shown also in this panel are stars within the cluster radius whose Mg I λ8807Å line strengths are available. The form of the relationship is similar to that in the left panel and we adopt a Mg I triplet EW value of 3.5Å as the value to discriminate dwarfs from giants. The value is consistent with the dwarf/giant discrimination discussed in Casey et al. (2012), who used similar 580V observations.

Metallicity of stars

The 2010 on-line version[5] of the Milky Way Globular Cluster catalogue (Harris 1996a) lists the metallicity of Pal 5 as [Fe/H] = –1.41 dex. This value has its origin in the Washington

[5]http://physwww.physics.mcmaster.ca/~harris/mwgc.dat

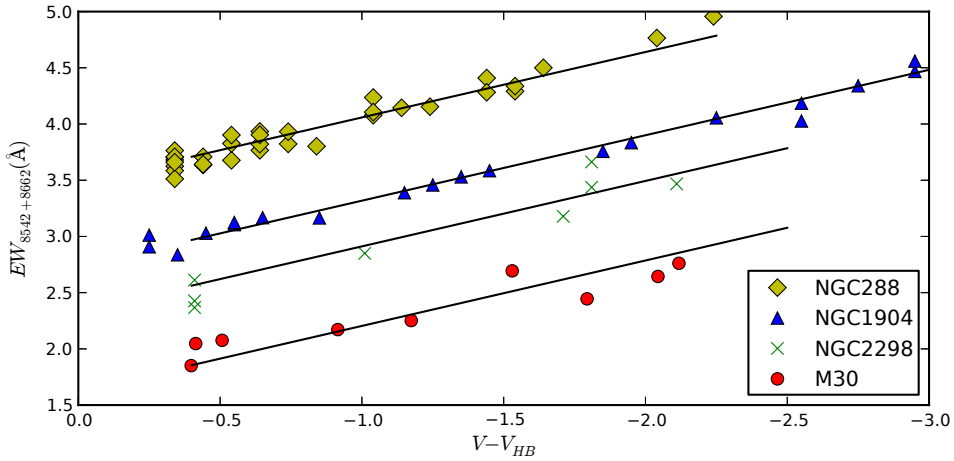

Figure 2.3: The summed EW of the $\lambda\lambda$8542 and 8662Å lines of the Ca II triplet are plotted against $V-V_{HB}$ for the calibration clusters M30 ([Fe/H] = –2.27), NGC 2298 (–1.92), NGC 1904 (–1.60) and NGC 288 (–1.32). The lines have a gradient α = −0.582 Å/mag.

system photometry of Geisler et al. (1997), which yielded [Fe/H] = –1.52 ± 0.28 (internal error), and in the high dispersion spectroscopy of 4 Pal 5 red giants analyzed by Smith et al. (2002) that gave [Fe/H] = –1.28 ± 0.03 (internal error). Since there is no evidence for any metallicity dispersion in Pal 5, (e.g., Smith et al. 2002) we can use metallicity as a further means to identity candidate cluster and tidal tail members.

Our metallicity determinations are based on the strength of the Ca II triplet lines in our spectra, following well-established techniques (e.g., Armandroff & Da Costa 1991). The calibration of the line strengths is determined from AAOmega 1700D spectra of red giants in four Galactic globular clusters obtained during other AAOmega observing programs. The calibration clusters are, in order of increasing metallicity, M30 (NGC 7099), NGC 2298, NGC 1904 and NGC 288. We measured the EWs of the two stronger Ca II lines in the calibration cluster spectra in the same way as for the Pal 5 program stars. The results are shown in Fig. 2.3 in which the line strengths are plotted against $V - V_{HB}$, where V_{HB} is the horizontal branch magnitude in the V-band for each cluster from the 2010 on-line version of the Harris (1996) catalogue. The V magnitudes of the red giant branch stars are generally taken from Stetson's on-line photometric catalogue[6].

The average gradient of the linear least-squares fit to the points for each calibration cluster is $\alpha = -0.58 \pm 0.03$ Å mag^{-1}, a value consistent with other studies. For example, Yong et al. (2014) find α = −0.60 from a similar set of AAOmega observations. If we

[6]http://www3.cadc-ccda.hia-iha.nrc-cnrc.gc.ca/community/STETSON/standards/

define the reduced equivalent width, EW_{red} by:

$$EW_{red} = EW_{CaII} + \alpha\,(V - V_{HB}) \tag{2.2}$$

where EW_{CaII} is the sum of the equivalent widths of the two stronger Ca II triplet lines, V is the magnitude of the star and V_{HB} is the magnitude of the horizontal branch, then the mean value of EW_{red} for each calibration cluster is equivalent to the value of the relations shown in Fig. 2.3 at $V = V_{HB}$. The resulting relation between these mean EW_{red} values and [Fe/H] is shown in Fig. 2.4. A linear least-squares fit to these points then yields the abundance calibration:

$$[Fe/H] = (0.524 \pm 0.043)EW_{red} - (3.104 \pm 0.041) \tag{2.3}$$

The rms about this relation is 0.04 dex and is shown by the dotted lines in Fig. 2.4. Consequently, for any given program star, we can calculate $V - V_{HB}$, assuming $V_{HB} = 17.51$ for Pal 5 (Harris 1996a), and thus the reduced equivalent width from the measured line strengths. Equation 2.3 then yields an abundance, which for members of the cluster and tidal tails, will be consistent with the known metallicity of Pal 5. In practice, we note first that for the stars in our sample, the SDSS *ugriz* photometry needs to be transformed to V magnitudes; we use the equations given in Jester et al. (2005). Second, equation 2.2 is generally only used for stars with $V - V_{HB} < 0$, while our sample potentially contains stars up to a magnitude fainter. Carrera et al. (2007), however, have shown that the relation between Ca II triplet line strength and M_V is linear to $M_V \approx 1.25$, i.e., $V - V_{HB} \approx 0.6$, although Saviane et al. (2012) have suggested the relation flattens for stars fainter than $V - V_{HB} \approx 0.3$. We have assumed the linear relation of equation 2.2 applies for all potential $V - V_{HB}$ values. Third, the combination of equations 2.2 and 2.3 strictly applies only to RGB stars. Asymptotic giant branch (AGB) stars, however, will have weaker EW_{CaII} values at a given $V - V_{HB}$ because of their higher temperatures, and as a result would be assigned a lower abundance. We have coped with these two effects by considering as plausible for membership a range in abundance about that determined from the Pal 5 RGB members (see §2.3.1). Finally, we note that Starkenburg et al. (2010) and Carrera et al. (2007) have shown that a linear relationship between EW_{red} and [Fe/H] is not appropriate when a large metallicity range is considered. This is not a issue here as we are concerned only with candidate Pal 5 members and the abundance of the cluster is within the range

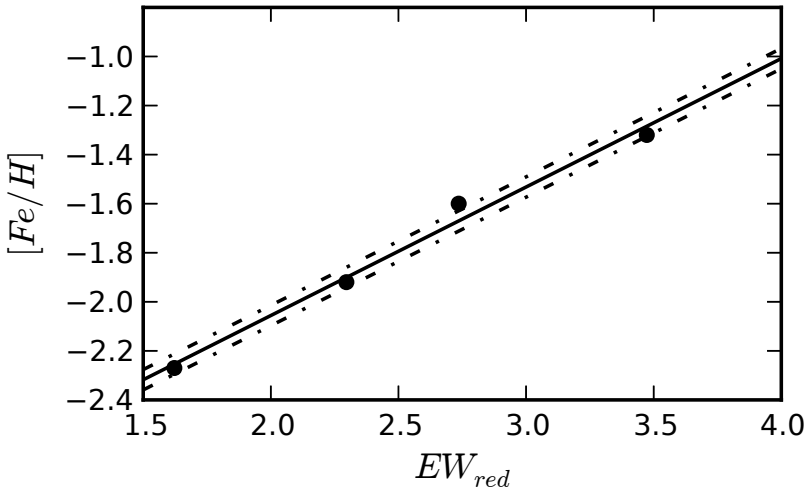

Figure 2.4: The solid circles are the reduced equivalent widths and [Fe/H] abundances for the calibration clusters. The solid line is a linear least-squares fit to these data, while the dotted lines show the rms for the fit.

spanned by the calibration clusters.

We now have velocities, photometry and Ca II and Mg I line strengths available for all the stars in our sample. In the next section, we will demonstrate how we employed these measurements to generate a list of probable members of Pal 5 and of its tidal tails.

2.3 Analysis and Discussion

The information described in the previous section is now employed to select candidate members of the cluster and of its tidal tails. However, the order in which the information was used was different depending on whether a particular star was a candidate cluster member or a candidate tidal tail member. The cluster member candidates are those that fall within our adopted radius for the cluster, while the tidal tail candidates are those beyond the adopted radius, whose value we now discuss. First, we note that using the core radius and concentration parameter given in the Harris catalogue (Harris 1996a) (2010 online edition), the nominal tidal radius of Pal 5 is 7.6′. On the other hand, the azimuthally averaged surface density profile given in Odenkirchen et al. (2003) shows a notable change in slope at about 12′ from the cluster centre, while the surface density profile in the directions perpendicular to the tidal tails show very few cluster stars beyond this radius. Dehnen et al. (2004), using similar data, found that the surface density profile of the cluster appeared to be truncated at ∼16′. Furthermore, Dehnen et al. (2004) calculated

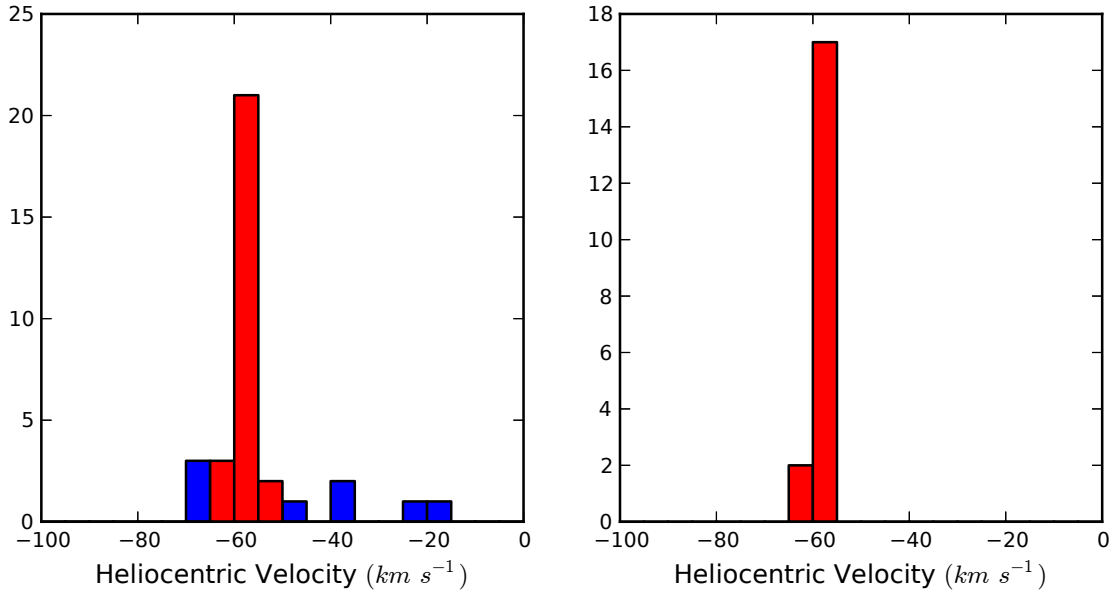

Figure 2.5: Left panel: Heliocentric velocity distribution for the red giant stars observed in fields F3 and F4 that are within a radius of 8.3′ from the centre of Pal 5. Stars that lie in the velocity range of –65 to –50 km s^{-1} are shown in red. Right panel: The velocity distribution of the 19 stars that remain after application of the dwarf/giant and Ca II line strength selection criteria.

a theoretical tidal radius for Pal 5 of 54 pc (8.0′) at the cluster's current position, while Mastrobuono-Battisti et al. (2012) adopted Dehnen et al. (2004)'s model A, which has tidal radius of 56 pc or 8.3′ at the cluster distance of 23.3 kpc. We decided to adopt this latter value as the radius at which to separate cluster member stars from stars which are likely members of the tidal tails. None of the following analysis is strongly dependent on the actual value used for the cluster radius.

2.3.1 Cluster Members

In the left panel of Fig. 2.5 we show the velocity histogram for the 34 candidate red giant stars observed in fields F3 and F4 that have velocities between –100 and zero km s^{-1}, and which lie within our adopted radius for the cluster. The bin size is 5 km s^{-1}, which is reasonable given that our largest velocity errors are ∼4 km s^{-1}. There is an obvious peak in the –60 to –55 km s^{-1} bin, which, since O02 give the velocity of Pal 5 as -58.7 ± 0.2 km s^{-1}, is clearly dominated by Pal 5 members. The velocity histogram, however, suggests that there remains a level of contamination from field star interlopers. We therefore have employed our selection criteria to increase the likelihood that the stars that survive the cuts are genuine cluster members. First, we use a photometric cut to remove stars that

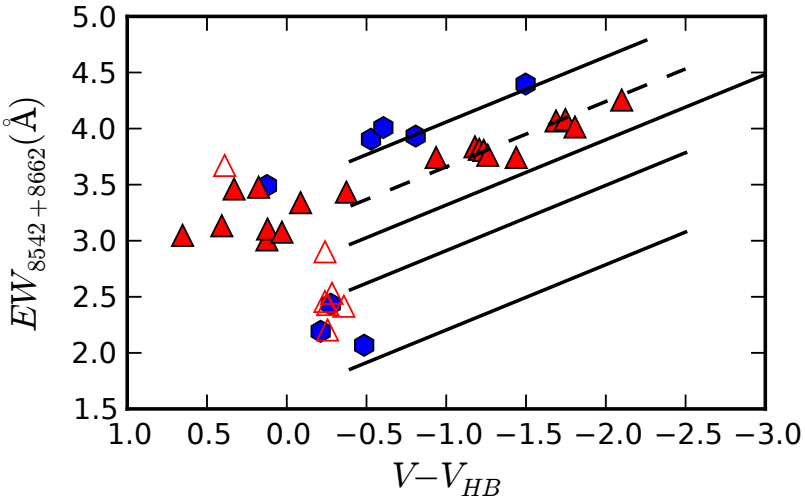

Figure 2.6: Ca II line strengths as a function of $V - V_{HB}$ are shown for the 34 stars in the left panel of Fig. 2.5. As in that figure stars in the velocity interval –65 to –50 km s^{-1} are plotted as red symbols and stars outside that velocity interval are shown as blue symbols. The solid lines are fiducial lines for the calibration clusters from Fig. 2.3. The dashed line shows the fit of a line of slope $\alpha = -0.58$ Å/mag to the 11 probable Pal 5 member stars with $V - V_{HB} < -0.2$. Fainter stars that are not considered likely members are shown as open red symbols.

lie far from the principal sequences in the Pal 5 CMD. We then applied our dwarf/giant separation criteria as illustrated in Fig. 2.2 to select against foreground dwarfs. The final criteria used was the requirement for consistency between observed Ca II line strength and the known metallicity of Pal 5. This is illustrated in Fig. 2.6, where for completeness we show the Ca II data for all the stars in the left panel of Fig. 2.5. As in that figure, stars in the velocity interval –65 to –50 km s^{-1} are plotted as red symbols, while stars outside that velocity range are plotted as blue symbols. Inspection of Fig. 2.6 shows a well-defined sequence of 11 red symbols with $V-V_{HB} <$ –0.2 that lies between, and parallel to, the fiducial lines for the calibration clusters NGC 1904 and NGC 288. Fitting a line of slope $\alpha =$ –0.58 Å/mag to these data, calculating the reduced equivalent width, and applying the abundance calibration of equation 2.3 then yields a mean abundance for these stars of $\langle$[Fe/H]$\rangle$ = –1.48 ± 0.10 dex. Here the uncertainty is the quadrature sum of the rms residual about the fitted line and the uncertainty in the abundance calibration. The derived abundance agrees well with the Pal 5 abundance ([Fe/H] = –1.41) given in the Harris catalogue and we conclude these stars are genuine Pal 5 cluster members. For the remaining fainter stars with velocities in the –65 to –50 km s^{-1} interval, which have $V-V_{HB}$ > 0, we use their location in this diagram and the errors in their line strength measures

to classify eight stars as likely cluster members. All these stars pass the CMD location and dwarf/giant separation tests, yielding a final sample of 19 Pal 5 cluster members. The velocity histogram of these stars is shown in the right panel of Fig. 2.5.

Cluster Kinematics

We now use our sample of 19 probable Pal 5 red giant members to investigate the kinematics of the cluster, using a maximum likelihood technique. Specifically, we follow the approach developed by Walker et al. (2006) in which the mean velocity V_r and the intrinsic velocity dispersion σ_{cl} of the cluster are derived from a set of N stars with velocities $\{v_1, \ldots, v_N\}$ and associated errors $\{\sigma_1, \ldots, \sigma_N\}$ via maximizing the joint probability function:

$$\ln(p) = -\frac{1}{2}\sum_{i=1}^{N} \ln\left(\sigma_i^2 + \sigma_{cl}^2\right) - \frac{1}{2}\sum_{i=1}^{N} \frac{(v_i - V_r)^2}{\left(\sigma_i^2 + \sigma_{cl}^2\right)} - \frac{N}{2}\ln(2\pi) \tag{2.4}$$

Application of the technique then yields a mean velocity for Pal 5 of $V_r = -57.4 \pm 0.3$ km s^{-1} and a velocity dispersion $\sigma_{cl} = 1.2^{+0.3}_{-0.2}$ km s^{-1}. The errors are determined by observing the parameter limits of the probability distribution of each variable that contains the central 68.3%. The mean velocity has an additional uncertainty of ± 0.8 km s^{-1} resulting from the uncertainty in the zero point of our velocity scale [7]. The velocity dispersion, despite its small value, represents a $>5\sigma$ detection. Odenkirchen et al. (2002), using a sample of 17 members, derived a mean velocity of –58.7 ± 0.2 km s^{-1} and a velocity dispersion of 1.1 ± 0.2 km s^{-1} for Pal 5. The velocity dispersion is in excellent agreement with our determination, while there is a difference (this work – previous) of 1.3 ± 0.4 km s^{-1} in the mean velocities. Given the ±0.8 km s^{-1} uncertainty in the zero point of our velocity scale, this difference is not significant.

Comparison with Odenkirchen et al. (2002)

As noted above, Odenkirchen et al. (2002) analysed the kinematics of Pal 5 using radial velocities derived from spectra taken with the UVES instrument on the VLT. From the 20 stars observed, all of which lie within 6′ of the cluster centre, 17 were classified as Pal 5 members primarily on the basis of radial velocity. Our Pal 5 sample includes 13 of these 17 stars, the other four were not included in the 2dF configurations. We categorize 12 of the stars in common as members of Pal 5, while one star, star 12 in O02 sample, we

[7] *This uncertainty is the standard deviation of the observed velocities about the catalogue values for eleven observations of four radial velocity standards*

Table 2.2: A comparison of the radial velocities derived here with those given by Odenkirchen et al. (2002) for the Pal 5 cluster stars in common.

Target	Star O02	v_{helio} (km s^{-1})	σ (km s^{-1})	v_{helio} O02 (km s^{-1})[a]	σ (km s^{-1})	Member[a]
P1205646	1	-57.9	0.7	–58.51	0.05	Yes
P1201565	2	-56.8	0.7	–58.31	0.05	Yes
P1206550	5	-56.0	0.6	–56.92	0.07	Yes
Pal5_229p5Oden148	6	–59.0	0.4	-58.72	0.09	Yes
P1203635	7	-57.7	0.8	–58.79	0.10	Yes
P1207360	9	-56.9	0.4	–57.35	0.15	Yes
P1204797	10	-56.4	1.0	–60.10	0.14	Yes
P1205893	11	-57.6	1.6	–58.90	0.09	Yes
Pal5_229p5Oden140	12	–55.6	3.9	-52.97	0.12	No
P1201384	13	-57.7	0.3	–58.98	0.08	Yes
Pal5_229p5Oden153	14	–60.9	3.3	-61.07	0.17	Yes
P1202728	17	-57.2	2.7	–58.54	0.06	Yes
P1205197	20	-55.6	1.5	–57.27	0.06	Yes

[a] Membership status as determined by applying our selection criteria.

classify as non-member on the basis of a Mg I line strength that exceeds our threshold. Our velocities and those of O02 are given in Table 2.2 for the stars in common, together with our membership classification. The (unweighted) mean velocity difference, in the sense (this work – O02), is 0.9 ± 0.4 km s^{-1} (std error of the mean), which is consistent with the difference in mean cluster velocity derived above. None of the velocity differences exceeds three times the standard deviation. The properties of the full sample of 19 Pal 5 red giant members, 12 in common with O02 and 7 new Pal 5 stars discovered in our analysis, are given in the first part of Table 2.4. The velocities presented are those derived here.

2.3.2 Tidal Tail Members

Although there is some existing information on the kinematics of the stars in the Pal 5 tidal tails (Odenkirchen et al. 2009), our spatial coverage is considerably more extensive. Consequently, it is not appropriate to use radial velocity as the primary selection criterion for membership in the tidal tails, rather we use the other selection criteria (Giant/Dwarf separation, CMD location and Ca II line strengths) first, and then investigate the radial velocities of the remaining stars. Specifically, we first excluded stars whose Mg I line strengths were above the cutoffs shown in Fig. 2.2. Second, we required consistency with the location of the Pal 5 member stars in the (Ca II line strength, $V - V_{HB}$) diagram (Fig.

2.6). Then we required consistency between the colour and magnitude of the stars and the principal sequences in the CMD of the cluster. Both these latter criteria implicitly assume that there is no substantial variation in distance from the Sun along the tidal tails compared to the distance to the cluster. This assumption is consistent with the results of Grillmair & Dionatos (2006), who, on the basis of their best-fit orbital model, indicate variations in the tidal tail distance modulus relative to that of the cluster of order 0.06 mag or less. Similarly, model A of Dehnen et al. (2004) shows variations in the distance modulus of the tidal tails that are relatively minor, insufficient to significantly affect the selection process. Only after we have a set of stars meeting these criteria did we consider the radial velocities, requiring candidate tidal tail members to have velocities in the range -70 to -35 km s^{-1}. This process resulted in a final sample of 47 candidate tidal tail members, 30 stars in the trailing tail and 17 stars in the leading tail. These candidate tidal tail stars cover the full extent of the area surveyed: for example, the most distant trailing tail star is ~17.5 deg, or 7.1 kpc in projection, from the centre of Pal 5. As an added check, we matched our candidates with the PPMXL (Roeser et al. 2010) and UCAC4 (Zacharias et al. 2013) catalogues. None of our stars possess measured proper motions in excess of the errors, consistent with their classification as (distant) giants.

In each of the 2dF fields in the outer parts of the trailing tail we have typically identified 3 candidate members per field. Given these small numbers we have used the Besançon model of the Galaxy (Robin et al. 2003) to investigate the extent to which any of our candidates might actually be field stars that, by chance, happen to meet our selection criteria. We generated 10 realizations from the Besançon model using the location of the outermost field F11 and the 2dF field-of-view. For each of these models we then randomly selected 10 sets of 330 stars (i.e., a typical observed sample) that lie within the selection window shown in the left panel of Fig. 1. Each set was then evaluated and the number of giants (i.e., log g < 3) with metallicities and velocities within our adopted ranges for Pal 5 recorded. We found that of the 100 trials, there were 11 occurrences where one model star met all our criteria and none where two or three were selected. Consequently, while we cannot rule out a minor level of contamination of our outer sample from field stars, it is not sufficient to significantly bias the results.

Table 2.3: A comparison of the radial velocities derived here with those give by Odenkirchen et al. (2009) for the Pal 5 tidal tail stars in common.

Target	Star O09	v_{helio} (km s^{-1})	σ (km s^{-1})	v_{helio} O02 (km s^{-1})[a]	σ (km s^{-1})	Member[a]
P1203859	20015	-58.7	1.4	–58.20	0.47	Yes
P1227758	20017	-59.1	1.3	–57.82	0.31	Yes
P1231315	20016	-56.7	2.3	–58.27	0.48	Yes
Pal5_231Oden_7	31076	–50.0	2.4	-51.73	0.22	Yes
Pal5_231Oden_6	20006	–56.5	2.6	-56.70	0.18	Yes
Pal5_231Oden_2	31023	–55.6	0.4	-55.44	0.22	Yes
Pal5S_113	30076	-57.8	1.1	–60.72	0.35	Yes
Pal5S_210	30218	-53.8	1.9	–60.89	0.28	Yes

[a] Membership status as determined by applying our selection criteria.

Comparison with Odenkirchen et al. 2009

In their study of the kinematics of the Pal 5 tidal tails, O09 identified 17 likely leading and trailing tidal tail members in a region covering approximately 8.5 deg on the sky. A comparison with our list of observed stars revealed 11 stars in common with O09, although 3 were subsequently discarded from our analysis as their spectra had unacceptably low signal-to-noise ratios. Reassuringly, the remaining 8 O09 stars were also classified as tidal tail members in our analysis. Table 2.3 compares our velocity measurements with the O09 values. Including all 8 stars, the (unweighted) mean velocity difference, in the sense (this work – O09), is 1.5 ± 0.9 km s^{-1} (std error of the mean). This value is consistent with that for the cluster-star comparison. The largest difference is for O09 star 30218 for which we find a velocity of –53.8 ± 1.9 km s^{-1}, 7.1 km s^{-1} higher than the –60.9 ± 0.3 km s^{-1} velocity given by O09. This star may be a binary. If it is excluded from the comparison, the mean velocity difference becomes 0.7 ± 0.6 km s^{-1}, indicating excellent agreement.

2.3.3 Blue Horizontal Branch Stars

As is apparent from the selection box in the left panel of Fig. 2.1, a number of the fields observed with 2dF include stars that are potentially blue horizontal branch (BHB) members ($(g-i)_0 \leq 0.25$) of the cluster and of the tidal tails. As these stars are hotter than their red giant counterparts, a different analysis approach was required. Clearly the requirement for agreement in colour and magnitude with the Pal 5 CMD sequence remains valid, but no metallicity estimate is possible as the Ca II triplet spectral region is now dominated by the hydrogen lines from the Paschen series. The principal contaminant of the candidate

BHB stars are foreground blue straggler stars. These were distinguished from genuine BHB candidates through the characteristically broader hydrogen lines of the higher gravity stars. Radial velocities were again calculated by cross-correlation, but this time the template employed was a high S/N spectrum of the field BHB star HD 86986, observed with the 1700D grating setup as part of a separate AAOmega program. We adopted the radial velocity given by SIMBAD for the star (9.5 ± 0.4 km s^{-1}); the uncertainty in the zero point of the resulting velocities is unlikely to exceed 2–3 km s^{-1}. Candidate BHB members of the cluster and the tidal tails were then chosen (after applying the photometric and gravity selection) on the basis of having velocities similar to velocities of red giant candidates in the same 2dF field. In the end only one BHB candidate was identified through this process. It lies just within our adopted cluster radius and its properties are given in the first part of Table 2.4. We have chosen not to include this star in the discussion of the cluster kinematics (see §2.3.1) because of the uncertainty in whether the velocity is on the same system as that for the red giants.

2.3.4 Final Tidal Tail Sample

The properties of the full sample of 47 Pal 5 tidal tail candidate members, of which 39 are new, are given in the second part of Table 2.4, where, for convenience, we present the stars in the leading and trailing tails separately. The location of these stars, and the cluster member candidates, are shown in the reddening corrected Pal 5 CMD of Fig. 2.7. Not surprisingly, the tidal tail stars conform closely to the principal cluster sequences in the CMD. In Fig. 2.8 we show the positions of the Pal 5 cluster and tidal tail stars over plotted on the contour diagram of Grillmair & Dionatos (2006), which uses photometry from SDSS DR4. Within approximately one degree or so of the cluster centre, our candidates align well with the surface density contours, which lie well above the background. At larger distances from the cluster, however, there is less of a correspondence between the location of the individual stars and the density contours, which lie closer to the background density. This comparative lack of correspondence can be ascribed to the small number of our candidates. A larger sample of fainter spectroscopically confirmed tidal tail stars should nevertheless coincide with the density contours, which, in the analyis of Grillmair & Dionatos (2006), are dominated by the location of the much numerous, as compared to red giants, main sequence stars.

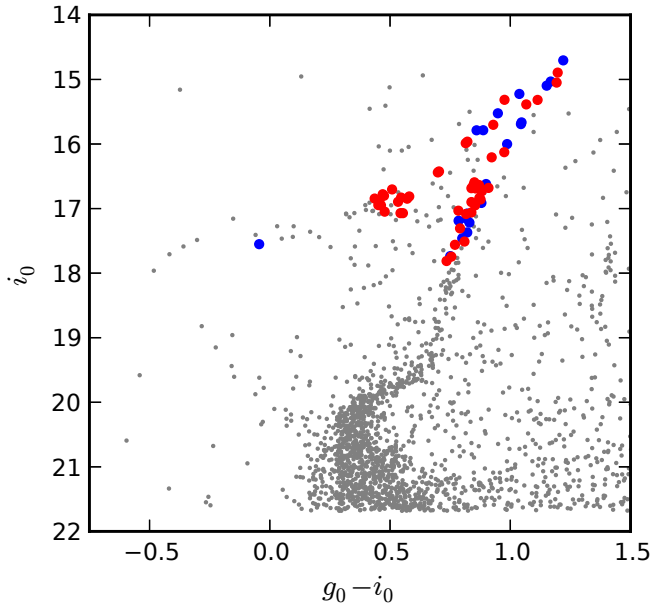

Figure 2.7: Location of candidate cluster and tidal tail member stars in the Pal 5 CMD from Fig. 2.1. Blue points indicate cluster stars, i.e., those within 8.3′ of the cluster centre. The red points show the tidal tail stars.

2.3.5 Velocity Gradient and Dispersion

In their study of the kinematics of the Pal 5 tidal tails, O09 revealed the presence of a linear gradient in the line-of-sight velocities of the tidal tail stars with angular position along the stream – velocities of the leading tail stars were more negative than that of the cluster, which in turn was more negative than the velocities of the trailing tail stars. The gradient determined was 1.0 ± 0.4 km s^{-1} deg^{-1} across an arc approximately 8.5 deg in extent, and for a sample of 15 candidate tidal tail members. O09 also determined the velocity dispersion in the tidal tails finding a value of 2.2 km s^{-1} for the same sample of 15 candidates, demonstrating that the tidal tails are a kinematically cold structure. Our study of the tidal tails covers a much larger angular extent than that of O09, particularly as regards the trailing tail, and thus it is important to evaluate whether the velocity gradient and the low velocity dispersion persist with increasing distance from the cluster centre.

In Fig. 2.9 we show the velocities of our tidal tail stars, i.e., those outside the cluster radius of 8.3′, against a, which we use to denote the angular distance in degrees of each star from the centre of Pal 5. We note that through the choice of the 2dF field centres, the candidate stars are at most ∼1 deg from the nominal stream centre in their vicinity, so that we can use a as valid measure of angular distance along the tidal tails. We note also that

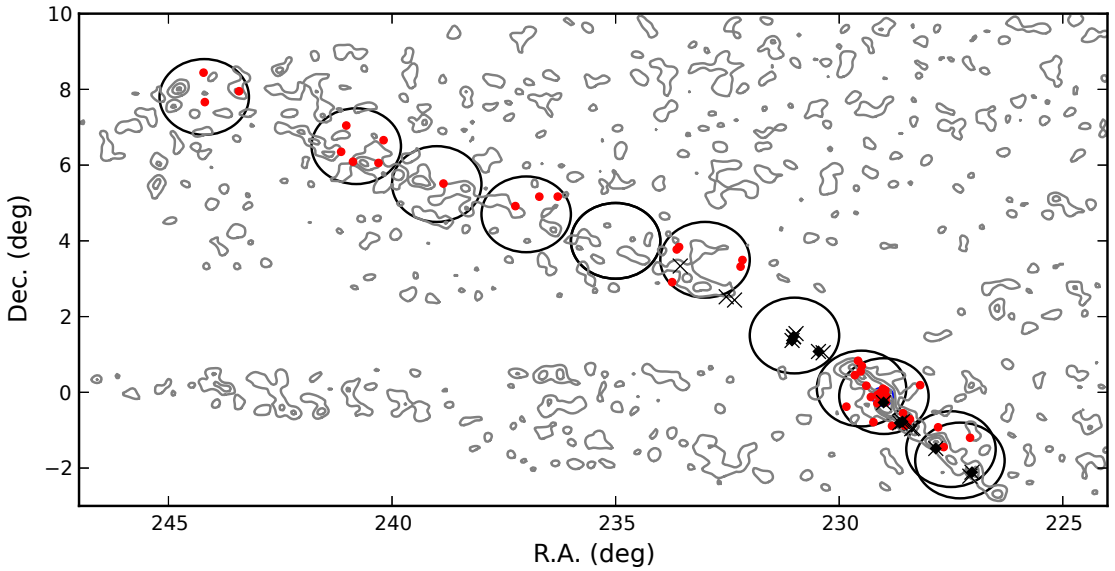

Figure 2.8: The positions of candidate members of the cluster, and of the tidal tails, compared to the surface density contours from Grillmair & Dionatos (2006). Red points indicate candidates found in this work. Black crosses show the tidal tail candidate stars from O09 and a superposed black dot indicates the star were also found in this study. The large circles indicate the 2dF fields studied, which are designated F1 – F11 in order of increasing Right Ascension.

a is positive in the trailing tail and negative in the leading tail, and that it is essentially equivalent to the quantity $\Delta l \cos b$ used by O09 for the region of the tails covered in their analysis.

If we consider first the region $-3^\circ < a < 6.5^\circ$, which coincides with the section of the tidal tails covered by O09, we find for our sample of 35 stars a linear gradient between v_r and a of 0.9 ± 0.3 km s^{-1} deg^{-1} through a weighted least-squares fit, where the weights are the inverse square of the velocity errors. This value is quite consistent with the gradient, 1.0 ± 0.4 km s^{-1} deg^{-1} found by O09. If we add to the sample the 7 tidal tail stars in O09's sample of 15 not observed by us, after adjusting their velocities by 0.7 km s^{-1} (see §2.3.2), the derived gradient is only marginally different 0.9 ± 0.1 km s^{-1} deg^{-1}. As regards the intrinsic velocity dispersion about this velocity gradient, we used the maximum likelihood approach described in §2.3.1 after first correcting the observed velocities by the velocity predicted at the a value of each star by linear velocity gradient. Such an approach is necessary since our velocity errors are notably larger than those of O09. We find that the intrinsic velocity dispersion in this region of the tidal arms is 2.0 ± 0.4 km s^{-1}, entirely consistent with the value of 2.2 km s^{-1} (no error given) found by O09. Increasing the

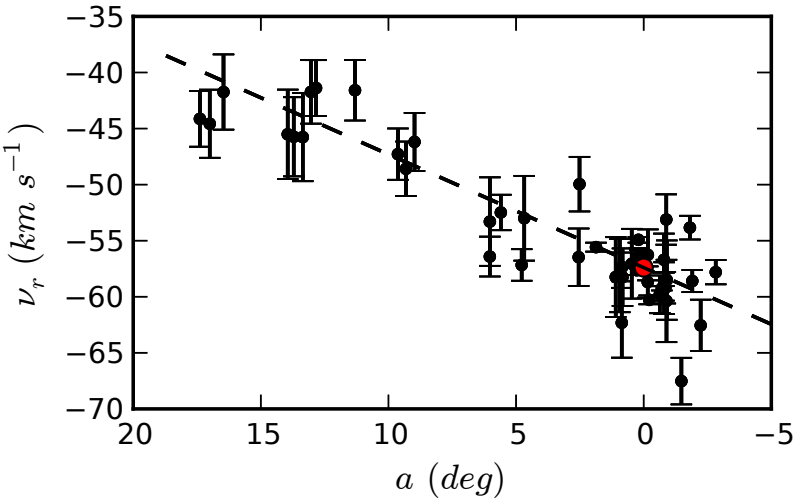

Figure 2.9: The radial velocities of the 47 Pal 5 tidal tail stars, i.e., those further than 8.3′ from the cluster centre, are plotted against a, the angular distance from the cluster centre in degrees. The red dot represents the mean velocity of the cluster stars, while the dashed line is the derived overall velocity gradient of 1.0 ± 0.1 km s^{-1}deg^{-1}.

sample with the additional 7 O09 stars does not appreciably change *the velocity dispersion (*1.8 ± 0.3*).*

We now consider the 12 trailing tail stars that lie beyond $a \approx 6$ deg, noting that currently there are no stars known in the leading tail at these distances from the cluster centre. Including the mean velocity for the cluster at $a = 0$, the derived gradient is 1.1 ± 0.1 km s^{-1} deg^{-1} which is not significantly different from the gradient shown by the inner sections of the tail. The intrinsic velocity dispersion was undetectable given the uncertainties of velocities. However, we can limit the velocity dispersion to less than 4.2 km s^{-1}, still characteristically low. If we consider only the data for these stars without including the mean velocity at $a = 0$, the calculated gradient becomes 0.4 ± 0.2 km s^{-1} deg^{-1}. This might indicate a decrease in the size of the velocity gradient in the outer parts of the trailing tail.

We now turn to determining the gradient and dispersion over the full almost 20 deg arc of tidal tails using the full sample of 47 tidal tail stars observed here. A first order fit yields a gradient of 1.0 ± 0.1 km s^{-1} deg^{-1} with an intrinsic dispersion about the gradient of 2.1 ± 0.4 km s^{-1}. The fit is shown in Fig. 2.9. Again these values are not appreciably different from those given in O09 despite the larger sample and the larger angular coverage. We also considered a quadratic fit to the data, but found that the quadratic term was not significant.

Our results reinforce the identification of the Pal 5 tidal tails as a kinematically cold structure, at least for the sections of the tidal tails that have kinematic data. The recent results of Carlberg et al. (2012) show that the trailing tail continues as a narrow feature for a total length of at least ∼23 deg; it may extend even longer as the Carlberg et al. (2012) analysis is limited by the boundary of the SDSS survey region. Kinematic studies of this extended region will be difficult, however, as the contrast of the tail features compared to the background is much reduced at lower Galactic latitudes. The current data on the surface density of the leading tail is also limited, at an angular extent of ∼6 deg, by the boundary of the SDSS survey region. In this case it is because the SDSS survey region does not penetrate to any significant extent south of the equator. The SkyMapper survey of the southern hemisphere sky (Keller et al. 2007) will, however, allow the leading tail to be mapped into the southern hemisphere. The SkyMapper filter system is designed to provide gravity and metallicity information (Keller et al. 2007) for survey stars, which should facilitate the selection of candidates for spectroscopic follow-up. It will be intriguing to see if a single velocity gradient and a constant velocity dispersion remain the best interpretation of the data when kinematic information is available for a comparable angular distance in the leading tail as is currently available for the trailing tail. Together with the results presented in this paper, such additional data would provide strong constraints on the orbit of Pal 5, on the tidal disruption process, and on the Galaxy's dark matter halo[8].

2.4 Conclusion

We have demonstrated here a detailed method for identifying members of Pal 5 and of its tidal tails. The approach distinguishes candidate members from contaminating field stars through a combination of kinematic, line strength and photometric information. The result is the selection of 67 candidate members of the cluster and its tidal tails, of which 47 are new objects. The sample consists of seven new red giant and one new BHB members lying within 8.3′ of the cluster centre, twelve reconfirmed cluster members, 27 new members of the trailing tail, three reconfirmed trailing tail stars, and 12 members of leading tail of which five were previously known. Our overall coverage is ∼20 deg along the tails, with the coverage of the trailing tail being substantially larger than in previous work.

For the Pal 5 cluster members we derive, through a maximum likelihood technique, a mean velocity of -57.4 ± 0.3 km s^{-1} and an intrinsic velocity dispersion of 1.2 ± 0.3 km

[8]See, for example, Küpper et al. (2015); Pearson et al. (2015).

s^{-1}, values that are consistent with previous determinations. Within the region of the tidal tails studied by O09, we find the same velocity gradient and velocity dispersion. Our angular coverage of the tidal tail is, however, considerably larger yet intriguingly we find that the velocity gradient and velocity dispersion do not change significantly from the O09 values. Our determination is a linear velocity gradient of 1.0 ± 0.1 km s^{-1} deg^{-1} and an intrinsic dispersion about this gradient of 2.1 ± 0.4 km s^{-1} across the almost 20 deg arc of the tidal tails studied here, although there is some indication that the gradient may be less at larger angular distances. The Pal 5 tidal tails are indeed kinematically cold structures. We note, however, that coverage of the leading tail is much less than that of the trailing tail, and we look forward to the outcomes of southern hemisphere sky surveys such as SkyMapper that will redress the situation. In summary, the results presented here provide a promising opportunity to further constrain the tidal disruption process, the orbit of Pal 5 and of the tidal tail stars, and in particular, the properties of the Galactic halo.

Table 2.4: A list of all stars determined to be members. The 'New Member' column denotes either the stars discovered here or those known from earlier work (O02 or O09).

Cluster Members							
Star Designation	R.A. (Deg, J2000)	Dec (Deg, J2000)	V_r (km s^{-1})	σ (km s^{-1})	Mag[a] (g–i)	Mag[a] (i)	New Member[b]
P1207696	15 15 48.19	–00 06 07	–55.9	1.2	0.84	17.85	Yes
P1207360	15 15 49.70	–00 07 01	–56.9	0.4	0.95	15.90	O02
P1206550	15 15 52.60	–00 07 40	–56.0	0.6	1.04	15.64	O02
P1205893	15 15 54.79	–00 06 55	–57.6	1.6	0.99	16.73	O02
P1205646	15 15 56.11	–00 06 06	–57.9	0.7	1.26	15.15	O02
P1205197	15 15 57.05	–00 08 50	–55.6	1.5	0.89	17.58	O02
P1204797	15 15 58.26	–00 09 47	–56.4	1.0	0.97	17.03	O02
P1204574	15 15 58.89	–00 05 17	–55.9	0.3	1.31	14.82	Yes
Pal5_229p5Oden148	15 15 59.52	–00 08 60	–59.0	0.4	1.08	16.12	O02
P1203635	15 16 02.00	–00 08 03	–58.0	0.8	0.97	16.75	O02
P1203153	15 16 03.61	–00 07 17	–57.7	2.5	1.14	15.81	Yes
P1202728	15 16 04.81	–00 06 28	–57.2	2.7	0.93	17.33	O02

Continued on next page.

[a] From SDSS catalogue.

[b] Denotes the origin of the membership classification: Yes for this paper, otherwise O02 or O09.

Star Designation	R.A. (Deg, J2000)	Dec (Deg, J2000)	V_r (km s^{-1})	σ (km s^{-1})	Mag[a] (g–i)	Mag[a] (i)	New Member[b]
P1202285	15 16 06.54	–00 07 01	–57.1	0.2	1.07	15.43	Yes
P1202039	15 16 07.75	–00 10 18	–60.6	0.3	1.14	15.78	Yes
Pal5_229p5Oden153	15 16 08.51	–00 05 10	–60.9	3.3	1.13	15.34	O02
P1198266	15 16 19.83	–00 01 08	–56.9	1.0	0.98	15.90	Yes
P1197361	15 16 23.11	–00 03 24	–58.0	2.5	0.88	17.31	Yes
P1194244	15 16 34.71	–00 04 25	–58.2	3.8	0.92	17.20	Yes
P1201565	15 16 08.66	–00 08 03	–56.8	0.7	0.91	17.27	O02
P1201384	15 16 09.58	–00 02 40	–57.7	0.3	1.25	15.21	O02
Trailing tail Members							
P1206410	15 15 52.84	00 03 22	–55.7	0.6	1.20	15.43	Yes
P1205450	15 15 56.21	00 02 25	–55.9	0.7	0.94	17.06	Yes
P1202648	15 16 05.26	00 05 42	–54.3	0.3	0.92	17.49	Yes
P1184727	15 17 09.99	–00 07 25	–57.0	0.4	0.93	16.10	Yes
P1178230	15 17 34.55	00 10 26	–56.5	3.1	1.02	16.81	Yes
P1172002	15 17 58.32	01 41 56	–57.5	3.3	0.86	17.67	Yes

Continued on next page.

[a] From SDSS catalogue.

[b] Denotes the origin of the membership classification: Yes for this paper, otherwise O02 or O09.

Star Designation	R.A. (Deg, J2000)	Dec (Deg, J2000)	V_r (km s^{-1})	σ (km s^{-1})	Mag[a] (g–i)	Mag[a] (i)	New Member[b]
Pal5_229p5_224	15 18 04.96	01 33 05	–57.7	2.6	1.04	16.43	Yes
P1166550	15 18 18.92	01 49 58	–57.6	3.6	0.97	16.84	Yes
P1161723	15 18 35.89	00 27 10	–56.7	1.3	1.30	15.01	Yes
P1149198	15 19 21.42	–00 22 43	–61.7	3.1	0.65	17.20	Yes
Pal5_231Oden_2	15 21 51.16	01 04 43	–55.6	0.4	0.94	16.79	O09
Pal5_231Oden_6	15 24 04.85	01 28 13	–56.5	2.6	0.96	16.78	O09
Pal5_231Oden_7	15 24 13.00	01 22 09	–50.0	2.4	0.96	16.72	O09
P1001405	15 28 39.20	03 29 37	–56.6	1.4	0.93	17.18	Yes
P0997712	15 28 49.34	03 19 10	–52.4	3.8	0.64	17.18	Yes
P0901878	15 34 19.31	04 50 15	–55.8	1.8	0.92	16.78	Yes
P0897761	15 34 31.90	04 46 24	–52.7	4.0	0.63	16.93	Yes
P0885066	15 34 56.51	03 54 34	–51.9	1.6	1.28	15.14	Yes
P0706090	15 45 10.57	05 10 06	–45.6	2.6	0.57	17.16	Yes
P0672715	15 46 49.44	05 10 01	–48.0	2.4	0.56	17.07	Yes
P0626179	15 48 57.99	05 55 04	–46.7	2.3	0.69	17.00	Yes
P0503947	15 55 24.13	06 30 47	–41.0	2.7	0.55	16.98	Yes

Continued on next page.

[a] From SDSS catalogue.

[b] Denotes the origin of the membership classification: Yes for this paper, otherwise O02 or O09.

Star Designation	R.A. (Deg, J2000)	Dec (Deg, J2000)	V_r (km s^{-1})	σ (km s^{-1})	Mag[a] (g–i)	Mag[a] (i)	New Member[b]
P0420925	16 00 45.41	07 39 29	–41.1	2.8	0.79	16.55	Yes
P0404276	16 01 12.59	06 03 23	–40.8	2.5	1.02	15.81	Yes
P0364040	16 03 29.59	06 05 26	–45.2	3.9	0.93	17.01	Yes
P0366470	16 04 05.53	07 02 43	–44.9	4.0	0.54	17.06	Yes
P0347248	16 04 33.28	06 21 07	–45.1	3.5	0.57	16.91	Yes
P0226451	16 13 40.97	08 57 05	–41.1	3.4	0.53	16.96	Yes
P0172773	16 16 44.79	08 39 50	–44.0	3.0	0.68	16.93	Yes
P0185610	16 16 51.73	08 26 29	–43.5	2.5	0.96	16.94	Yes
Leading tail Members							
Pal5S_113	15 08 07.15	–02 06 39	–57.8	1.1	1.00	16.82	O09
P1340251	15 08 17.50	–01 11 59	–62.0	2.3	0.63	16.85	Yes
P1298414	15 10 39.02	–01 26 45	–58.0	1.0	1.11	16.29	Yes
P1288424	15 11 09.04	–01 55 24	–66.9	2.1	0.92	16.11	Yes
Pal5S_210	15 11 21.70	–01 29 02	–53.8	1.1	1.03	17.04	O09
P1258991	15 12 45.44	00 11 23	–52.5	2.2	0.56	16.89	Yes
P1242532	15 13 40.44	–01 42 29	–58.6	1.4	1.04	16.35	Yes

Continued on next page.

[a] From SDSS catalogue.

[b] Denotes the origin of the membership classification: Yes for this paper, otherwise O02 or O09.

Star Designation	R.A. (Deg, J2000)	Dec (Deg, J2000)	V_r (km s^{-1})	σ (km s^{-1})	Mag[a] (g–i)	Mag[a] (i)	New Member[b]
P1238216	15 13 54.40	–01 49 09	–59.8	3.7	0.85	17.95	Yes
P1234307	15 14 09.32	–01 52 40	–57.9	3.5	0.87	17.89	Yes
P1232006	15 14 17.18	–01 33 08	–59.2	1.7	0.92	17.65	Yes
P1231315	15 14 20.71	–01 46 22	–56.7	2.3	0.94	17.23	O09
P1227758	15 14 34.63	–01 48 27	–59.1	1.3	0.91	17.46	O09
P1216792	15 15 16.47	–01 53 10	–58.6	2.3	0.65	17.04	Yes
P1207226	15 15 50.43	–00 15 45	–55.7	2.3	0.88	17.15	Yes
P1203859	15 16 01.54	–00 16 08	–58.7	1.4	1.08	16.13	O09
P1194127	15 16 34.95	–00 17 26	–59.7	0.4	1.17	15.51	Yes
P1188878	15 16 56.20	–01 47 20	–58.7	0.2	0.82	16.57	Yes

[a] From SDSS catalogue.

[b] Denotes the origin of the membership classification: Yes for this paper, otherwise O02 or O09.

2.5 Appendix

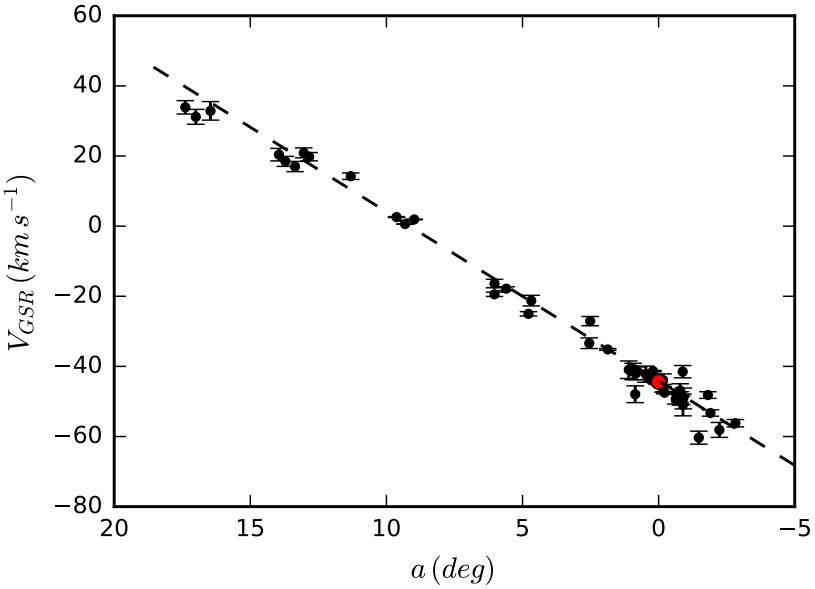

Figure 2.10: The Galactocentric velocities (V_{GSR}) against angular distance. The points are the same as what was presented in Fig. 2.9. The dashed line indicates the velocity gradient (4.7 ± 0.1 km s^{-1}deg^{-1}).

After this work was published, a discussion with Prof. Ken Freeman about the velocity gradient observed in the tidal tails led us to complete an additional analysis. In this chapter, we presented the existence of a linear velocity gradient along the tails. However, it is possible that this could be, at least in part, an artefact of the reference frame we have performed our calculations in; our reference in this chapter is heliocentric (V_r). It is worth exploring whether a linear gradient remains the best interpretation when considering the velocities of our targets relative to the Galactocentric standard of rest. After applying the appropriate correction, we replotted the velocities as a function of radial distance from the center of Palomar 5 (as in Fig. 2.9), and this is displayed in Fig. 2.10. We explored a linear and quadratic fit to the galactocentric velocities, and found that a linear description remains the best interpretation. Here, the velocity gradient is 4.7 ± 0.1 km s^{-1} deg^{-1}, with an associated velocity dispersion about the gradient in the tails of 3.0 ± 0.4 km s^{-1}.

2.6 Addendum

See the following articles for more information on the topics discussed in this chapter:

- The definition of tidal radius: von Hoerner (1957) and Allen et al. (2006).
- Apperance of tidal tails: Montuori et al. (2008) and Klimentowski et al. (2009).
- Detections of tidal tails in globular clusters: Belokurov et al. (2006a); Chen & Chen (2010); Niederste-Ostholt et al. (2010); Jordi & Grebel (2010); Sollima et al. (2012); Balbinot et al. (2011); Myeong et al. (2017) and Navarrete et al. (2017).

Chapter 3

The Outer Envelopes of Globular Clusters - I. NGC 7089 (M2)

This chapter is based on the published article "The Outer Envelopes of Globular Clusters - I. NGC 7089 (M2)", P. B. Kuzma, G. S. Da Costa, A. D. Mackey, T. A. Roderick, 2016, Monthly Notices of the Royal Astronomical Society, 461, p.p. 3639. Minor typographical and grammatical changes have been made as a result of the Examiner Reports. Significant alterations to the original text, as suggested from the Examiner Reports, are shown in italics.

We present the results of a wide-field imaging survey of the periphery of the Milky Way globular cluster NGC 7089 (M2). Data were obtained with MegaCam on the Magellan Clay Telescope, and the Dark Energy Camera on the Blanco Telescope. We find that M2 is embedded in a diffuse stellar envelope extending to a radial distance of at least $\sim 60'$ ($\sim$ 210 pc) – five times the nominal tidal radius of the cluster. The envelope appears nearly circular in shape, has a radial density decline well described by a power law of index $\gamma = -2.2 \pm 0.2$, and contains approximately 1.6% of the luminosity of the entire system. While the origin of the envelope cannot be robustly identified using the presently available data, the fact that M2 also hosts stellar populations exhibiting a broad dispersion in the abundances of both iron and a variety of neutron capture elements suggests that this object might plausibly constitute the stripped nucleus of a dwarf Galaxy that was long ago accreted and destroyed by the Milky Way.

3.1 Introduction

In the ΛCDM cosmological model, present-day large galaxies form hierarchically (e.g., Steinmetz & Navarro 2002). Dark matter clumps merge and combine at early times to

form protogalaxies, which themselves merge into larger systems, and so on. Stellar halos around large galaxies are thought to arise as a by-product of these processes (e.g., Bullock & Johnston 2005; Cooper et al. 2010); the growth of this component continues even at late times via the accretion of dwarf galaxies into massive systems, contributing stars and globular clusters into the diffuse halo region. The seminal work of Searle & Zinn (1978) provided some of the first observational evidence for this scenario in the Milky Way, by demonstrating that globular clusters outside the solar circle do not exhibit the correlation between Galactocentric distance and metallicity observed among innermost globular clusters. More recent work has revealed that a substantial fraction of Milky Way globular clusters follow a clear age-metallicity relationship that is consistent with their formation in external systems (e.g., Marín-Franch et al. 2009; Dotter et al. 2010; Leaman et al. 2013); there are also distinct similarities between many outer halo globular clusters in the Milky Way and globular clusters seen in nearby dwarf galaxies (e.g., Mackey & Gilmore 2004; Mackey & van den Bergh 2005). Collectively this evidence suggests that the current halo globular cluster population is a mixture of objects of extra-Galactic origin and those that formed in the Milky Way.

Direct evidence for the build up of the Galactic halo via the accretion of smaller galaxies came with the serendipitous discovery of the disrupting Sagittarius dwarf (Ibata et al. 1994). The stream associated with this system can be traced in a complete loop around the Milky Way (e.g., Yanny et al. 2009a, and references therein), and a number of globular clusters have been linked with the dwarf – either directly (namely M54, Arp 2, Terzan 7 and Terzan 8, Da Costa & Armandroff 1995), or through possible association with the stream (Ibata et al. 1995; Bellazzini et al. 2003; Martínez-Delgado et al. 2004; Law & Majewski 2010a).

However, despite the interaction between Sagittarius and the Milky Way unravelling before us, and the discovery, to date, of nearly two dozen much smaller stellar streams, there is an apparent dearth of large-scale substructures in the Milky Way halo when compared to the situation observed in our neighbouring spiral galaxy, M31. The Pan-Andromeda Archaeological Survey (PAndAS; McConnachie et al. 2009) has utilised deep wide-field imaging to reveal that the M31 halo contains an abundance of large streams and over-densities (e.g., Ibata et al. 2014), as well as a substantial globular cluster population extending to very large Galactocentric radii (Huxor et al. 2014). Many of these remote globular clusters are spatially coincident with, and share the same velocity as, underlying

stellar streams (Mackey et al. 2010b, 2013, 2014; Veljanoski et al. 2013, 2014), indicating that they were formed in satellite dwarfs that were subsequently accreted into the M31 halo.

It is not clear whether the apparent lack of large streams in the Milky Way halo compared to the M31 halo reflects an intrinsic difference between the two galaxies, or is the result of observational bias. Finding large-scale structures in M31 is certainly a considerably easier task than for the Milky Way – the angle subtended by the M31 halo is tiny compared to the all-sky surveys required, at similar photometric depth, to probe to commensurate radii in the Milky Way halo. At present our best efforts come from major surveys such as the Sloan Digital Sky Survey (SDSS, Fukugita et al. 1996; Gunn et al. 1998; York et al. 2000) and the Pan-STARRS1 3π survey (Tonry et al. 2012); however these are comparatively shallow and trace the Milky Way halo *out to* ~ 50 *kpc at high contrast (e.g., Grillmair 2009)*. Probing to larger distances requires the use of rare tracers, such as blue horizontal branch stars, RR Lyrae variables, or M giants, that are not necessarily well suited to detecting very low surface brightness substructures.

One alternative possibility is to employ a deep targeted survey. Since most of the globular clusters in the outer M31 halo reside in or near stellar streams, there are globular clusters known to be embedded in the Sagittarius stream, and many other remote Milky Way clusters are hypothesised to be accreted objects, it is plausible that globular clusters in the Milky Way might act as efficient tracers for distant large scale halo structures. Indeed, an attempt to search for streams around a variety of Galactic globular clusters has been performed recently by Carballo-Bello et al. (2014). While between six and ten clusters in their sample of 23 show promising evidence for minor stellar populations beyond their tidal radii, ultimately the lack of a sufficiently large field of view left the authors unable to draw any firm conclusions as to whether these populations might represent large streams, globular cluster tidal tails, or some other kind of extended structure. A handful of other similar studies have been performed in the past decade (e.g., Leon et al. 2000; Chun et al. 2010; Jordi & Grebel 2010), and while some globular clusters have been reported to have tidal tails, no large scale streams have been discovered.

We are conducting our own search for stellar streams in the outer Galactic halo by studying globular clusters and their surroundings. Modern wide-field mosaic imagers such as the Dark Energy Camera (DECam; Flaugher et al. 2015) on the 4-m Blanco Telescope at Cerro Tololo Inter-American Observatory (CTIO) and MegaCam (McLeod et al. 2015)

on the 6.5-m Clay Telescope at Las Campanas Observatory (LCO), are perfect instruments for this task. We have predominantly targeted clusters that have properties indicative of a possible extra-Galactic origin. As well as large-scale streams belonging to destroyed dwarf galaxies, it is possible that we may reveal tidal tails that belong to the globular clusters themselves. Such structures are already known for several Galactic globular clusters – the prototypes being Palomar 5 (e.g., Odenkirchen et al. 2001; Grillmair & Dionatos 2006; Odenkirchen et al. 2009) and NGC 5466 (e.g., Belokurov et al. 2006a; Grillmair & Johnson 2006). They exhibit a characteristic two-arm structure, and have a width that is approximately that of the progenitor cluster. This differentiates them from debris due to a lost dwarf galaxy host, which is expected to be much broader on the sky such that it surrounds a cluster in all directions.

In this paper we report results for the first target of our survey, NGC 7089 (M2). This cluster possesses a variety of unusual characteristics, some of which are suggestive of an extra-Galactic origin. Grillmair et al. (1995) explored the outskirts of M2 through star counts from photographic plates and found indications of extended structure surrounding the cluster, including significant deviations in the radial density profile from the expected King (1962) shape. They concluded it was likely that M2 possesses tidal tails. More recently, it has been revealed that M2 hosts stellar populations with a broad dispersion in iron abundance – Yong et al. (2014) detected a dominant peak at [Fe/H] ≈ -1.7 and weaker peaks in the distribution at [Fe/H] ≈ -1.5 and -1.0, though these results have been challenged by Lardo et al. (2016). Furthermore, Yong et al. (2014) also presented evidence for significant star-to-star variation in a number of neutron capture elements (see also Lardo et al. 2013), and variations in light element abundances have been found by Lardo et al. (2012). These properties are unusual, observed in only a handful of Galactic globular clusters. They have been reinforced photometrically – precision multi-band measurements from the *Hubble Space Telescope* have revealed a complex colour-magnitude diagram that, in particular, exhibits multiple sub-giant branches (Milone et al. 2015), corresponding well with the peaks in the metallicity distribution published by Yong et al. (2014). Combined, these properties render M2 rather similar to other anomalous massive clusters such as ω Cen and M54. The former has long been suggested as the remaining core of a long-defunct dwarf galaxy (e.g., Freeman 1993), while the latter resides at the centre of the Sagittarius dwarf (e.g., Ibata et al. 1995; Layden & Sarajedini 2000).

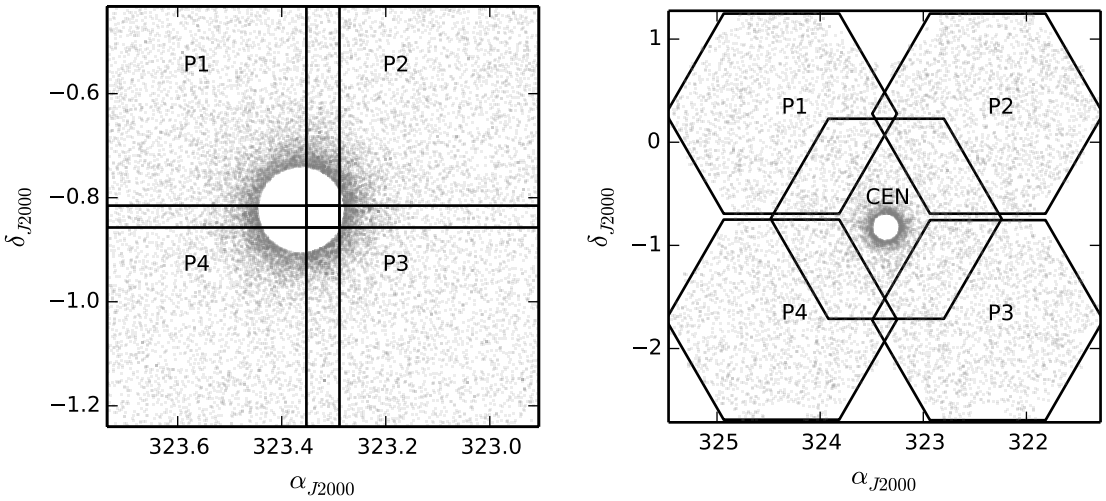

Figure 3.1: Our observed fields around M2 from MegaCam (left) and DECam (right). Detected sources are marked with grey points. The crowded central regions of the cluster have been excluded; the radii of the excluded regions are 5′ for MegaCam and 7′ for DECam.

3.2 Observations and Data reduction

3.2.1 Observations

This work utilises two sets of observations, as summarised in Table 3.1. The first set was obtained with the MegaCam instrument on the 6.5m Magellan Clay telescope at LCO on 2013 September 10. MegaCam is a mosaic wide field imager that utilises 36 2048 x 4608 CCDs arranged in a 9×4 array, allowing for a $25' \times 25'$ field of view (McLeod et al. 2015). The 2×2 binned pixel scale is 0.16 arcsec/pixel. We obtained a mosaic of four pointings, with the cluster located in the corner of each field (Figure 3.1; left) in order to maximise the area imaged around its outskirts. Each field was observed in the g and i bands for 3×90 seconds and 3×300 seconds respectively. The exposures were dithered to allow complete coverage by filling the gaps between the CCDs. Altogether, our four pointings cover a $0.8^\circ \times 0.8^\circ$ region centred on M2. The image quality during this set of observations varied, with that in g ranging between $0.6'' - 0.9''$, and that in i between $0.5'' - 0.9''$. Basic processing of the data – bias subtraction, flat-fielding, astrometric calibration and image stacking – was conducted using the MegaCam reduction pipeline[1] available at the Harvard-Smithsonian Center for Astrophysics (see McLeod et al. 2015).

[1] `http://hopper.si.edu/wiki/piper/Megacam+Data+Reduction`

Table 3.1: *Observations employed in this work.*

Camera	Date	Field	Field Centre		N_{exp}	Exp. Time	Filter	Seeing (arcsec)		
		Name	R.A. (J2000)	Dec. (J2000)		per frame (s)		1	2	3
MegaCam	2013 Sept 10	P1	21:34:03	-00:38:42	3	90	g	0.83	0.86	0.70
					3	300	i	0.89	0.60	0.56
		P2	21:32:31	-00:38:42	3	90	g	0.65	0.63	0.66
					3	300	i	0.51	0.65	0.60
		P3	21:32:31	-01:01:42	3	90	g	0.64	0.64	0.69
					3	300	i	0.56	0.58	0.64
		P4	21:34:03	-01:01:42	3	90	g	0.91	0.80	0.86
					3	300	i	0.68	0.73	0.67
DECam	2013 Sept 26	CEN	21:33:27	-00:44:31	3	300	g	1.17	1.13	1.17
					3	300	i	1.03	1.05	1.02
		P1	21:29:30	00:16:38	3	300	g	1.16	1.11	1.19
					3	300	i	1.08	1.00	1.02
		P2	21:37:31	00:16:51	3	300	g	1.10	1.04	1.05
					3	300	i	1.00	1.00	1.16
		P3	21:29:30	-01:43:15	3	300	g	1.06	1.09	1.09
					3	300	i	1.09	1.00	1.17
		P4	21:37:30	-01:43:12	3	300	g	1.33	1.33	1.49
					3	300	i	1.11	1.09	1.24

The second set of observations was obtained with DECam on the 4-m Blanco telescope at CTIO on 2013 September 26 as part of program number 2013B-0617 (PI: Mackey). DECam (Flaugher et al. 2015) is a mosaic wide field imager boasting a three square degree field, comprised of a roughly hexagonal arrangement of 62 2048 x 4096 CCDs with an associated pixel scale of 0.27 arcsec/pixel. We observed five fields with DECam, arranged symmetrically in a cross-shape around M2 which was placed at the middle of the central field (see Figure 3.1; right). Combined, our DECam data spans an approximately 13 square degree region around M2. As with MegaCam, individual exposures at each pointing were dithered three times; each single exposure had an integration time of 300 seconds in both g and i. For four of the five fields (CEN though to P3), the image quality was relatively consistent for both g ($\approx 1.1'' - 1.2''$) and i ($\approx 1.0'' - 1.1''$); however for the fifth field (P4) the image quality was noticeably poorer, particularly in the g band (see. Table 3.1). Basic processing of our DECam observations was carried out via the community pipeline[2] (Valdes et al. 2014).

We note that MegaCam and DECam are complementary to each other for the present study. MegaCam has a comparatively higher spatial resolution and can perform deeper imaging in given exposure time than DECam, while DECam has a significantly larger field of view. Thus observations with MegaCam are perfect for exploring the crowded central regions of clusters, while DECam is ideal for exploring the vast space surrounding the cluster. Unless stated otherwise, the following discussion of our photometry procedures and data analysis is similar for both the MegaCam and DECam observations.

3.2.2 Photometry

Photometric measurements were obtained using Source Extractor[3] (SExtractor; Bertin & Arnouts 1996). SExtractor is a software package that detects and performs photometry on sources in images, providing a variety of customisable parameters for the extraction. For this work, we utilised the aperture photometry feature from SExtractor to conduct our measurements[4]. SExtractor was run twice on each image; the first run implemented a high detection threshold (25σ above the mean pixel value) to find the brightest point sources in the field. These are predominately stars, and the measured median full-width

[2] `http://www.ctio.noao.edu/noao/content/dark-energy-camera-decam`

[3] `https://www.astromatic.net/software/sextractor`

[4] *We acknowledge that PSF-fitting photometry may provide comparably better results, particularly in the faint limit. However, we do not believe its application would significantly change the results of the thesis. Application of the technique is being considered for future analysis of similar data for other clusters.*

at half-maximum (FWHM; $\bar{F}$) was used to define two aperture sizes ($1 \times \bar{F}$ & $2 \times \bar{F}$) for a deeper subsequent application of SExtractor. This deeper extraction employed a detection threshold of 1.5σ[5], a level that allows detection of the faintest objects in the image while maintaining a minimal number of spurious detections. This methodology delivered a photometric catalogue for all individual frames, and the corresponding stacked frames, per pointing per filter.

We initially intended to work with the stacked images at each pointing. However, we found that variations in the seeing between each of the individual exposures in a stack led to irregular variations in the stellar PSF across the field of view, resulting in sub-optimal photometry. This was true for both the MegaCam and DECam observations. Therefore, we chose to work with SExtractor measurements from the individual exposures, cross-matching the resulting catalogues and averaging the photometry for each given detection. This alleviated all of the problems arising from the use of the stacked images. We explored the possibility of systematically variable seeing across individual images, and while we observed a slight difference in some cases, we found that application of fixed apertures for each single frame provided sufficient photometric stability for our purposes.

An inevitable outcome of the photometric pipeline discussed above is the extraction of non-stellar objects, together with poor-quality and/or spurious detections. These are due to a variety of different source types – background galaxies, blends between neighbouring stars, CCD defects, and, especially in single images, cosmic rays. It is imperative that we remove these unwanted detections from the SExtractor catalogues; to do this we employed a multi-step approach. First, SExtractor itself helped with the process via its internal diagnostic tools: the star/galaxy classifier and internal quality flags. The star/galaxy classifier is a number assigned to each detection that varies between zero and one, with zero referring to a definite galaxy and one to a definite star. Observing the distribution of this flag amongst fainter objects, there is a clear bimodal distribution at flag values at 0 and 1, as well as large number of stars gathering between a flag value of 0.5 and 0.35. With the possibility of losing photometric depth if performing too stringent a cut, we decided to remove objects with a star/galaxy classification of 0.35 and below. However, none of the results presented here are strongly sensitive to the actual value adopted. The internal quality flags indicate the reliability of a given photometric measurement. A value of zero indicates a source that is located in a region bereft of nearby stars and that is not near the

[5]The sigma is a true (local) pixel-to-pixel standard deviation. However, SExtractor has a number of algorithms in place to help reduce the number of spurious detections that appear at this level.

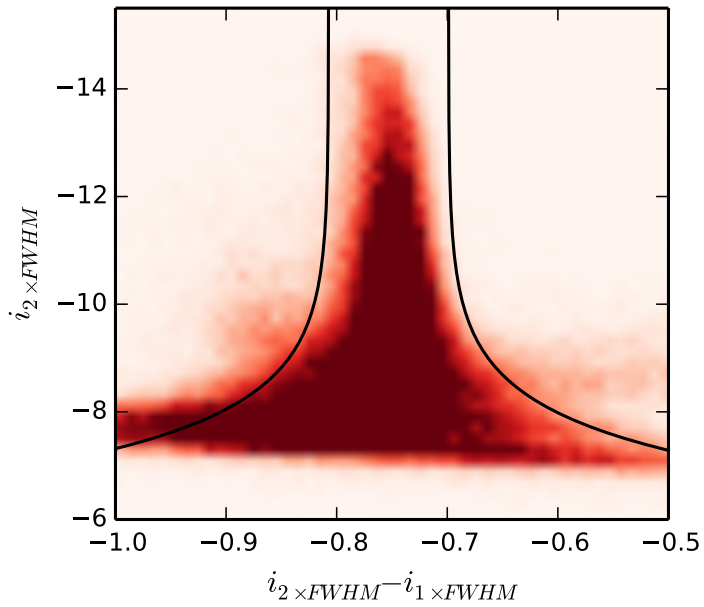

Figure 3.2: An example of the cleaning technique discussed in text *displayed with instrument magnitudes*. The boundaries delineate the regions where objects were removed from the sample as non-stellar detections – most notably excluding the plume of galaxies on the left and probable cosmic rays on the right. *Further, possible superposition of faint stars is seen in the asymmetry of the distribution.*

edge of a CCD. Lower quality photometry is represented by non-zero values[6]. We removed all objects with a non-zero quality flag.

These combined SExtractor diagnostics were, however, insufficient to give satisfactory cleaning of galaxies and cosmic rays in the SExtractor output. We therefore implemented an additional step to help refine the stellar catalogues, by performing a cut based on the difference in magnitude between our two different aperture sizes. This difference in magnitudes should be consistent for stars (which share a similar light profile across a given image), but more negative for objects with a broader light profile (e.g., galaxies), and more positive for objects with a sharper light profile (e.g., cosmic rays). In Figure 3.2, the brightest point sources populate a narrow magnitude difference and this spread becomes broader as the stars become fainter. This is indicative of uncertainties in the photometry increasing at lower magnitudes. Splitting the distribution in half about the median value of the aperture magnitude difference for stars $-13 \leq i \leq -11$, we fit an exponential curve to the right side of the distribution to define a boundary to eliminate non-stellar sources as well as point sources with unusually large uncertainties. This boundary was reflected

[6]Please refer to the SExtractor manual for more information regarding the flags.

about the median value to the left side of the distribution and objects that lay outside these boundaries (i.e., galaxies on the left and possible cosmic rays on the right side of the distribution) were removed. We performed this cut only on the i-band catalogues, as the seeing was typically better in this filter than in the g filter.

We next desired to merge our individual catalogues and unify the photometric scales. First, for each g and i exposure pair (i.e., in a given field at matching dither points) the catalogues from our cleaning procedure were cross-matched using the command-line package Stilts (Taylor 2006) to create lists containing stellar sources with good quality measurements and detections in both filters. Next, we cross-matched the three individual photometric catalogues for each pointing to create a single stellar catalogue for that field. For a given pointing the exposure with the deepest photometry was determined to be the master frame, and photometry from the remaining exposures was calibrated to the same scale as for the master. We did this by utilising the stars observed across multiple exposures to calculate the median photometric offsets, and then applied these to place all exposures on the same scale as the master. Once all the three exposures were on the same photometric scale, the catalogues were combined – stars that were observed in either two or three of the images had their photometry calculated as the weighted mean of the SExtractor output photometry, using the inverse square of the uncertainties on the photometry reported by SExtractor as the weights. Finally, we repeated this process to merge all of the individual pointings for a given camera into a final catalogue, resulting in one catalogue for MegaCam observations and one for DECam observations. Overlapping regions between different fields were used to determine the offsets necessary to shift photometry for all pointings onto the same scale.

As a final step, we used photometry for the M2 region from the SDSS data release 12 (Alam et al. 2015) to place our measurements onto an absolute scale. Stars recovered by our pipeline were cross-matched with the SDSS catalogue, and then used to fit to a linear relationship, plus a colour term, in order to transform from our instrumental magnitudes to the SDSS system. Table 3.2 displays our zero points and coefficients for the colour term for both MegaCam and DECam. Once both the catalogues were calibrated to the SDSS photometry, we dereddened all magnitudes (denoted as g_0 and i_0) using the values contained in the SDSS catalogue, which originally come from the maps provided by Schlegel, Finkbeiner, & Davis (1998). Each star from our catalogues that was matched with an SDSS source was corrected by the corresponding reddening value listed in the

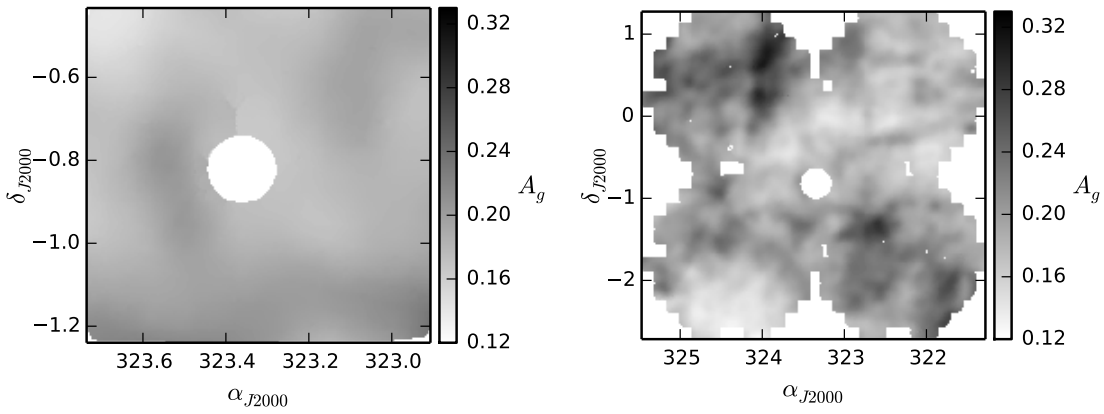

Figure 3.3: The A_g extinction map for sources appearing in SDSS DR12 (Ahn et al. 2014), based on the reddening maps of Schlegel et al. (1998), and smoothed with a gaussian function of width 36′. The MegaCam field of view is on the left, and DECam on the right. The excised inner cluster regions are the same as in Figure 3.1.

Table 3.2: The parameters used to calibrate our instrumental photometry to the SDSS system.

Camera	Filter	Calibration	
		Zero Point	Colour Coeff.
MegaCam	g	31.104 ± 0.024	−0.050 ± 0.009
	i	31.542 ± 0.021	0.038 ± 0.008
DECam	g	31.104 ± 0.005	0.059 ± 0.002
	i	31.165 ± 0.003	0.072 ± 0.001

SDSS catalogue, while those stars that did not have a match were given a correction that corresponded to that for the nearest star in the SDSS catalogue. Figure 4.3 shows the extinction across both fields of view for both cameras – the reddening is mild but quite spatially variable.

3.2.3 Artificial Star Tests

Since this study is concerned with searching for low surface *density* structures across large areas of sky, it was imperative to explore the completeness of our photometry as a function of magnitude and spatial position. If not properly accounted for, variable completeness levels across the different images in our mosaics could potentially result in detections of low surface brightness features that are not real. To quantify the completeness levels, we randomly placed 10000 artificial stars into each DECam field and 2000 artificial stars into

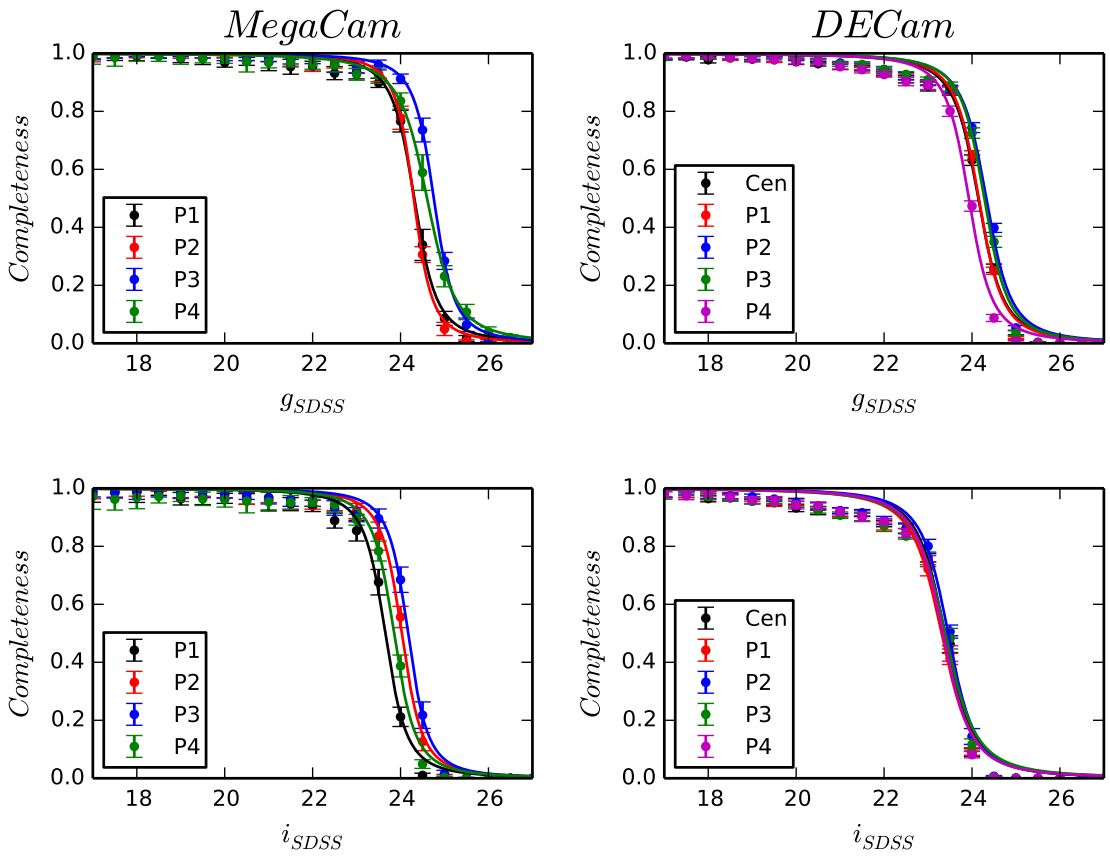

Figure 3.4: Completeness functions for each of our observed fields. The top row displays the g-band observations and the bottom row presents the i-band observations. The left column corresponds to MegaCam, and DECam is on the right. The completeness functions have been fit with the interpolation model from Fleming et al. (1995), which is marked by the solid line for each field.

each MegaCam, using the IRAF[7] command *mkobject*. The artificial stars had magnitudes between 17 and 27.5, with a higher proportion of stars at faint magnitudes to better reflect the luminosity function. After the artificial stars were placed in the fields, the images were run through the pipeline described in §3.2.2, including the cleaning steps. The artificial stars were deemed as detected if they were found in the photometric catalogs after the cleaning steps. This process was repeated ten times per field, per camera, leading to 100000 simulated stars per field for DECam and 20000 stars for MegaCam.

The completeness function for each field, along with a corresponding fit using the interpolation model from Fleming et al. (1995) [8] is displayed in Figure 3.4. To ensure uniformity across each of the two mosaics we decided to cut our catalogues at a level

[7] `http://iraf.noao.edu/`

[8] textitThe Fleming models may not fit the data perfectly above 85%, but our 90% completeness cut off is based on the test data, not the models themselves.

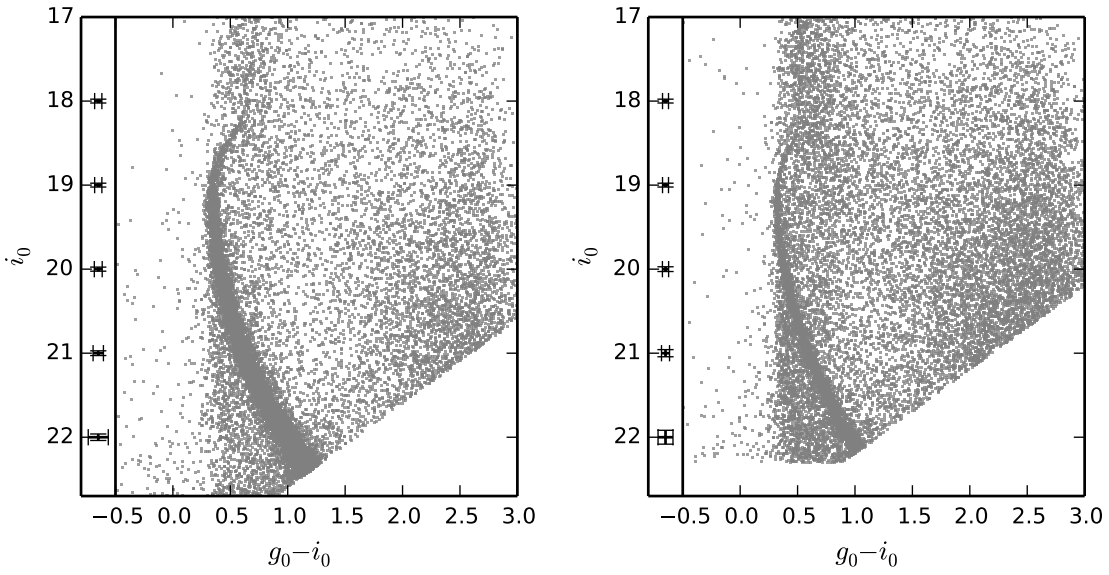

Figure 3.5: Colour-magnitude diagrams of our final stellar catalogues for MegaCam (left) and DECam (right). Both plots are accompanied by the typical photometric uncertainties at different brightness levels. Empty regions are caused by the 90% completeness cuts that we applied. Note that for the DECam catalogue we only plot stars within 40′ of the cluster centre to maintain visibility of the cluster sequences against the background.

corresponding to 90% completeness in the field with the shallowest photometry. With respect to our DECam measurements, we find the g–band cut-off to be at $g = 23.2$ and the i-band cut-off to be at $i = 22.3$. For our MegaCam measurements, the limits are at $g = 23.6$ and $i = 22.7$.

3.2.4 Complete Catalogue

Application of the completeness limits was the last step in obtaining our final photometric catalogues. The resulting colour-magnitude diagrams (CMDs) are displayed in Figure 4.4. In both plots the main sequence and the main sequence turn-off (MSTO) of M2 are clearly seen, and it is these features that we focus on for the remainder of this work because they are the locations on the CMD where the signal of M2 populations is greatest with respect to background contamination.

We performed photometric cuts to remove surplus stars in regions of the CMD that were not important for this study. Specifically, we removed the region occupied by red dwarfs in the foreground (belonging to the Galactic disk), which have $(g - i) > 1.6$, as well as stars with an i magnitude brighter than 18. This latter cut excluded the lower red giant branch of the cluster, but in this region of the CMD the number of M2 members

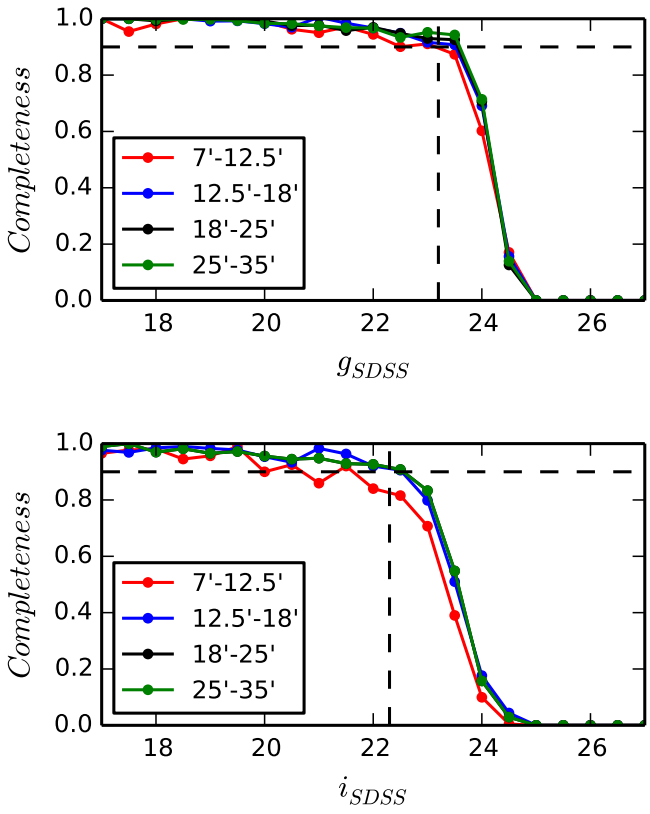

Figure 3.6: DECam completeness as a function of distance: g-band completeness is displayed in the top panel and i-band in the bottom panel. The vertical and horizontal dashed lines indicate the 90% completeness level and the corresponding magnitude adopted.

relative to contaminants is low, especially at large radii from the cluster (this can be seen towards the top of the DECam CMD in Figure 4.4). Also excluded are blue horizontal branch stars belonging to M2 – although these are often used as tracers due to the low levels of contamination at blue colours, they are sufficiently bright that the majority of this population was saturated in all images such that the photometry was unreliable.

Finally, we note that the cluster centre, in both sets of imaging, is too crowded for us to retrieve any meaningful photometry. The effects of crowding can be observed by constructing the completeness function at different radii from the cluster centre. For example, Fig. 3.6 displays the completeness function for the DECam data at different radii. Outside the nominal tidal radius of $\sim 12.5'$ arcmin there is no evident variation in the completeness function. Inside $12.5'$, the completeness is noticeably degraded when we begin to include data at radii down to $\sim 7'$, although note that above the 90% cut-off that we assume across all pointings, the difference is marginal. By observing the radial dependence in this way, we set an inner limit of $7'$ for the DECam data and $5'$ for the

MegaCam data. This provides an acceptable balance between probing more central regions of the cluster (for example, to accurately determine the locus of cluster populations on the CMD) and limiting the effects of crowding on the photometric uncertainties and detection completeness. We emphasise, however, that our analysis is almost completely focused on regions well beyond the nominal tidal radius of 12.5′, where the spatial variation of the completeness curve is negligible.

3.3 Results

In this Section we describe our search for *low surface density* features in the vicinity of M2. Unless stated otherwise, the techniques we apply are identical for both the MegaCam and DECam photometric catalogues.

3.3.1 Over-density Detection

Selection of Cluster Members

The locus of M2 members is easily visible in both the MegaCam and DECam CMDs, and our aim is to reliably separate those M2 stars from the non-members – primarily foreground stars belonging to the Milky Way. To do this, we adopted an isochrone from the Dartmouth Stellar Evolution Database[9] (Dotter et al. 2008) and fit it to the M2 sequence. We found that an isochrone with age= 13 Gyr, $[Fe/H] = -1.7$, and $[\alpha/Fe] = +0.4$ provided a good description of the data – these parameters are a reasonable match for those in the literature (e.g., Dotter et al. 2010). We adopted the absolute distance modulus listed in the 2010 edition of the Harris (1996a) catalogue but allowed small changes to obtain the best fit between the isochrone and the cluster main sequence. All stars in our catalogues were then assigned a "weight", according to a Gaussian distribution with the standard deviation set to be the colour difference from the isochrone value at a given i magnitude in units of the mean photometric uncertainty (determined from the rms of the photometry of stars observed in multiple images) in the measured colour at that magnitude. The Gaussian function was normalised such that a star falling on the isochrone would have a weight of 1.0. Stars were then separated into two sets, "cluster" and "foreground", based on their assigned weight[10]. The threshold used to separate stars into the two sets was determined

[9] `http://stellar.dartmouth.edu/~models/index.html`

[10] *We acknowledge that application of a full matched-filter technique (e.g., Rockosi et al. 2002; Grillmair 2009) may have produced improved results, though we expect that use of the technique would not affect the results significantly.*

empirically to encompass the observed width of the M2 main sequence, and corresponds to a weight value of 0.1 for MegaCam and 0.2 for DECam. Above these values stars are classified as belonging to the cluster; below them, to the foreground. Figure 3.7 shows the results of our weighting scheme. Note that our set of cluster members still has some level of contamination due to non-members that happen, by chance, to lie near the isochrone. We attempt to account for this contamination in our subsequent analysis.

Radial Density Profile

Milky Way globular clusters typically have radial density profiles that are well described by the family of (empirical) King (1962) models:

$$n(r) = k\left(\frac{1}{\sqrt{1+(r/r_c)^2}} - \frac{1}{\sqrt{1+(r_t/r_c)^2}}\right)^2 , \tag{3.1}$$

where r_c and r_t are the core and tidal radii respectively, and r is the distance from the cluster centre. The coefficient k is proportional to the central surface density (but is not the central density itself, as can easily be seen by setting r to zero in the above equation). These models exhibit a characteristic sharp truncation as r approaches r_t; King (1966) later showed that such a truncation arises due to the influence of an external tidal field (in which case the velocity distribution takes a lowered Maxwellian form). The signature of *low surface density* structure surrounding a globular cluster is the lack of this truncation; in such cases the outer density profile commonly exhibits a power-law decline – for example due to tidal tails (as observed around Pal 5 Odenkirchen et al. 2001) or a diffuse envelope (as seen around NGC 1851 Olszewski et al. 2009). Stars in this region are commonly referred to as "extra-tidal".

To create a radial profile for M2, we split our catalogues into circular annuli about the cluster center, each of which was then sub-divided into eight sections. We calculated the density of cluster stars in each of these sub-sections and used the mean value as the annular density, and the standard deviation as the corresponding uncertainty in this value. We allowed the width of our annuli to increase with radius, to help suppress uncertainties due to the declining number of cluster stars at large distances from the cluster centre. Also at large radii, portions of each annulus began to fall off the edge of our imaged mosaic, decreasing the effective area observed. To remedy this problem, for each impacted annular sub-section we performed a Monte Carlo simulation whereby a large number of points was

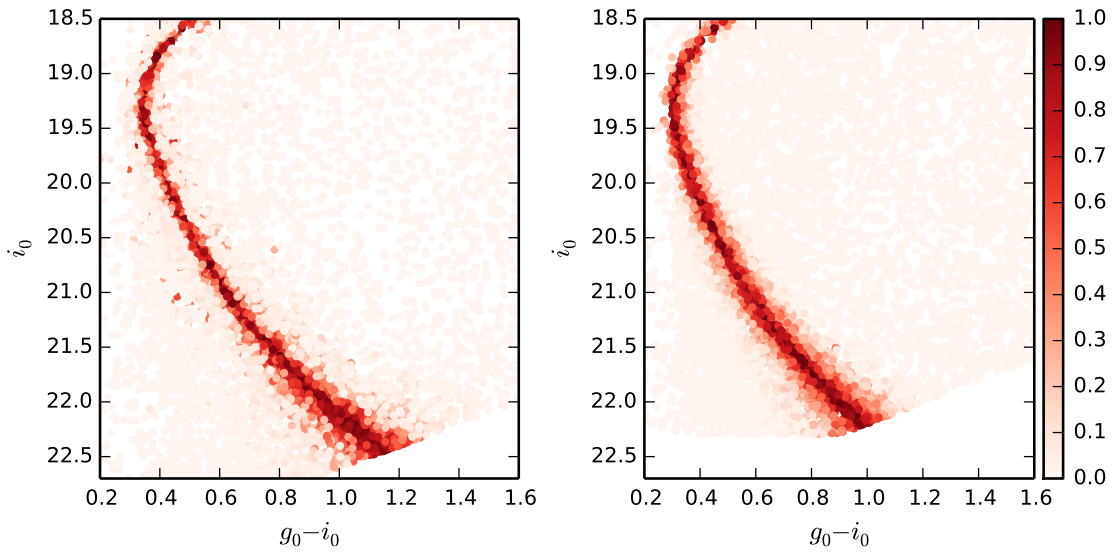

Figure 3.7: The isochrone-based weighting scheme for the CMDs show in Fig 4.4 – each star has been coloured according to their assigned weight. As before, the CMD from our MegaCam catalogue is on the left, and from our DECam catalogue on the right.

uniformly generated in the region, and each point was determined to lie either inside, or outside, the field of view. We used the ratio of points that fell within the field to the total number placed to scale the calculated density to the correct level. If the ratio was less than 30%, it was considered to be too low and the corresponding ring section was disregarded from further analysis.

We first created a profile without accounting for any residual contamination due to non-members of the cluster, and observed that the profile flattened to an approximately uniform value at a radial distance beyond $\approx 60'$. We estimated the foreground level by randomly sampling multiple sub-regions surrounding the cluster, $10'$ in diameter, centred at radii between $60' - 110'$, and generating a distribution of foreground densities. The foreground density ultimately subtracted from the profile was the mean of this distribution, and the uncertainty in this level was its standard deviation.

Our final radial density profile for M2 is plotted in Figure 3.8. Our DECam measurements have been scaled to match those from MegaCam (which are deeper) by applying a vertical shift calculated in the region of overlap near the tidal radius. As our star counts do not sample the centre of the cluster, and we are unable to make integrated light measurements because the unresolved cluster centre is severely saturated in our images, we supplement our data with aperture photometry from Kron & Mayall (1960), Hanes & Brodie (1985) and Peterson (1986). Since these observations were made in different filters,

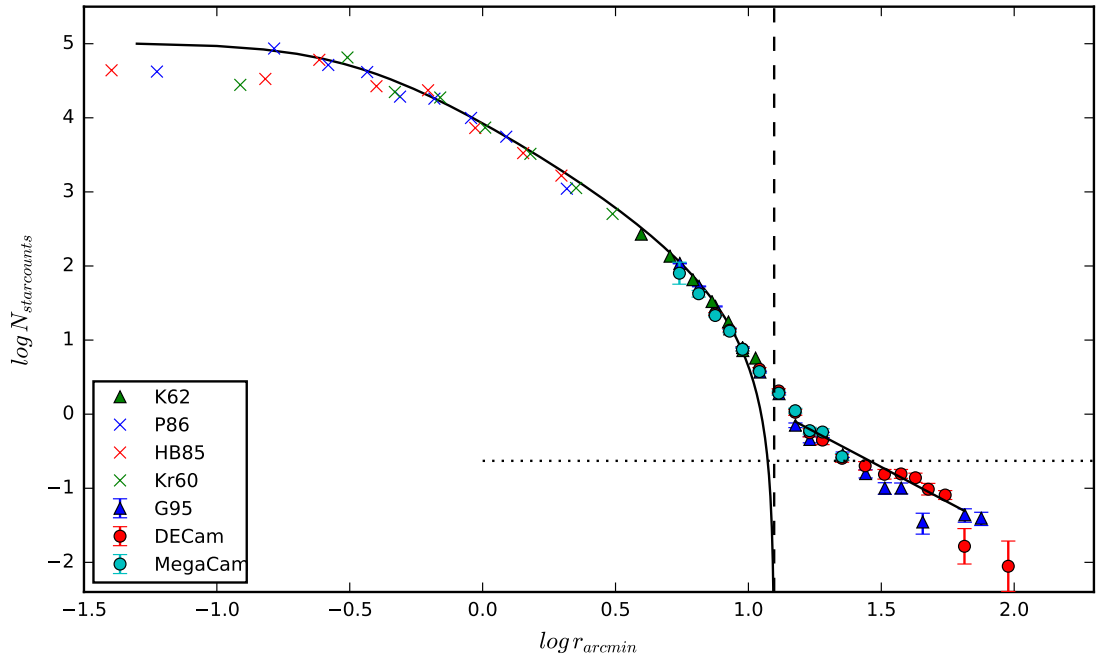

Figure 3.8: Our azimuthally averaged background-subtracted radial density profile for M2. This shows our measurements from both MegaCam and DECam, together with data from the literature. In general, solid symbols correspond to star count measurements, while crosses indicate aperture photometry. A King (1962) profile, using structural parameters from Harris (1996a) (2010 edition), is marked with a solid black line. The nominal tidal radius of 12.5′ for this model is indicated with a dashed vertical line, while the horizontal dotted line shows our calculated background level. Measurements in the cluster outskirts follow a power-law decline beyond the nominal tidal radius; *the plotted profile has* $\rho \propto r^{-2.2}$. All literature measurements have been normalised to our MegaCam profile. *Key: G95: (Grillmair et al. 1995), K62: (King 1962), P86:(Peterson 1986), HB85: (Hanes & Brodie 1985), Kr60: (Kron & Mayall 1960).*

we have applied a vertical shift to match them to our MegaCam star counts. Also plotted are star counts from King (1962) and Grillmair et al. (1995), again shifted to match our measurements. We further present a King (1962) model, again normalised to our MegaCam data, using the core and tidal radii from Harris (1996a) (2010 edition): $r_c = 0.32'$ and $r_t = 12.5'$.

It is immediately obvious from Figure 3.8 that our profile does not exhibit a sharp truncation, but instead follows a much more gradual decline with radius. Measurements by Grillmair et al. (1995) first presented possible evidence for extra-tidal features around M2, and this is strongly confirmed by our much higher quality data. According to our measurements the entire field of view of our MegaCam mosaic is occupied by M2 stars, even though the nominal tidal radius sits well within its footprint. Beyond the MegaCam

Table 3.3: Parameters used to calculate the 2D density maps.

Parameter	MegaCam	DECam
Bin width	$7'' \times 7''$	$36'' \times 36''$
Smoothing width	$35''$	$4.8'$
Masked region (radii)	$12.5'$	$60'$

observations, our DECam profile follows the findings of Grillmair et al. (1995) quite closely. The outer profile of M2 is reasonably well described by a power-law decline, with an index $\gamma = -2.2 \pm 0.2$. In the next section we investigate how this extra-tidal structure is distributed on the sky.

Foreground Subtraction and 2D Density Distribution

To explore the spatial density distribution of M2 members we created, for each camera, a 2D histogram of star counts using stars classified as cluster members according to their CMD weight. The number of bins along the spatial dimensions of the histogram (in this case α and δ) is different between the two cameras, reflecting the different regions of the cluster the two different mosaics were focused on. Table 4.7 displays the bin sizes used for the two separate data sets.

As described above, each catalogue of cluster members still suffers from some degree of contamination. To account for this, we constructed a second 2D histogram of star counts for each camera, using stars classed as foreground members. For a given camera, both the "cluster" and "foreground" 2D distributions were normalized by dividing the number of stars in a bin by the total number of stars in the sample, then dividing by the area of the bin. We then fit a 1×1 bi-variate polynomial to the foreground distribution, and subtracted this from the density distribution of cluster stars to create a contamination corrected 2D density distribution, which had any large-scale gradients or fluctuations due to the foreground removed. The resulting maps were smoothed using a gaussian kernel of different widths for the two cameras. The width of the smoothing function for both data sets is presented in Table 4.7.

Next, we searched these corrected distributions for regions harbouring over-densities of M2 stars. Our basic methodology was to define a region far from the cluster centre (as listed in Table 4.7), measure the mean and standard deviation of the bin densities in this region, and then examine fluctuations across the entire field of view in units of the number of standard deviations above or below the mean. For our DECam data this procedure was

straightforward. Based on our radial density profile we masked out everything within a radius of 60′ of the cluster, and used all bins outside this radius to calculate the relevant statistics. We then experimented to determine what constituted a suitable threshold above the mean to consider a fluctuation as a *bona fide* over-density of M2 stars. If the threshold was set too low, too many peaks corresponding to random noise in the background were detected. Conversely, if the threshold was set too high, only the central region of the cluster was detected. Ultimately we explored a series of detection thresholds, beginning at 1σ and extended to 3σ, to see how structures detected at lower significance were related to statistically more robust features.

For MegaCam, the situation was more complex. We previously observed that the entire field of view of our MegaCam mosaic is occupied by M2 stars. Hence, even the outskirts of the footprint did not constitute a clean non-cluster region for the purposes of determining the background statistics. As a result, while we went ahead and employed the same methodology using the region outside the nominal tidal radius of 12.5′, we did not enforce a specific detection threshold when analysing the MegaCam results. Nonetheless, this allowed us to determine the overall shape of the distribution of M2 stars in the MegaCam footprint, and search for any substantial over-densities.

Our 2D density distribution maps are displayed in Figures 3.9 (MegaCam) and 3.10 (DECam). The first of these confirms that that stars belonging M2 can be observed across the entire area covered by our MegaCam imaging. Despite the difficulty in identifying a suitable region for determining the background statistics, the MegaCam map further reveals that the M2 stars are evenly spread, with no evident divergence from an approximately circular distribution, and no large scale over-densities. Moving to the DECam map, the extent of the envelope seen in the radial profile and the MegaCam map is revealed. We observe a large extended outer envelope, rather evenly spread in azimuth instead of constituting distinct tidal tails as suggested by Grillmair et al. (1995). To the south-west, the envelope connects to a 3σ detection through a low-significance feature, and consequently we present that over-density as part of the overall structure that we have detected. We find that the envelope extends to a radial distance of $\approx 60'$ (~ 210 pc) at the 3σ threshold. While the radial profile hints at features possibly extending as far as $\sim 100'$ (~ 335 pc), the overall shape of that potential structure is not evident from our 2D density distribution as it occurs at low significance.

We employed a bivariate gaussian fit to the debris over the region $12.5' - 70'$ to explore

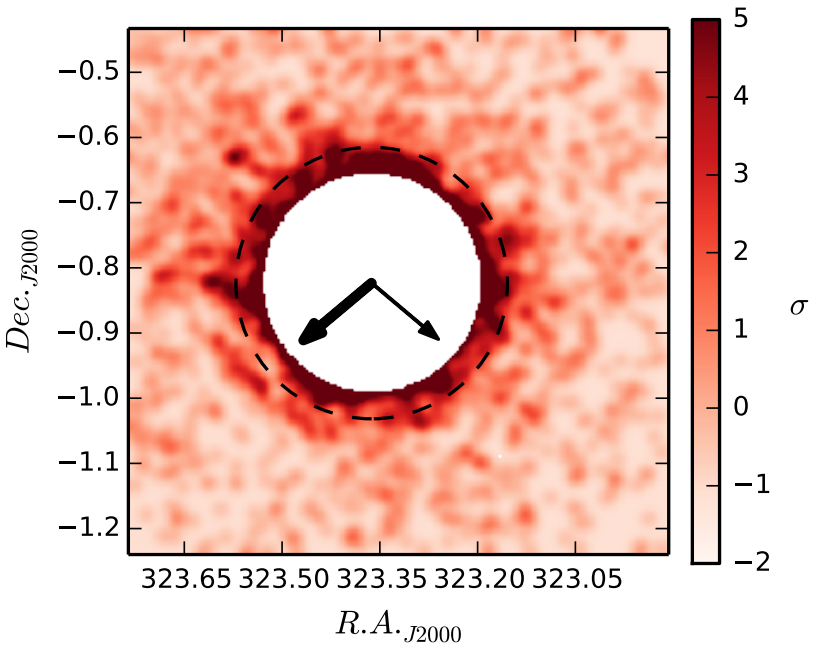

Figure 3.9: Stellar density distribution for the MegaCam catalogue, split into $7'' \times 7''$ bins and smoothed using a gaussian kernel of width $35''$. The colour scale represents the number of standard deviations above the mean background value that a given bin sits. To enhance clarity in this map, a circular region of radius $10'$ has been masked at the cluster centre. The two arrows indicate the direction of the proper motion of M2 (the bold arrow; *Dinescu et al. (1999)*) and the direction of the Galactic centre. The dashed ring indicates the nominal tidal radius of $12.5'$.

the shape of the extended of M2 envelope and whether the structure has a distinct major axis direction. We performed this calculation using the python AstroML module[11], finding an ellipticity of $e = 0.11 \pm 0.06$ with the major axis oriented with a position angle $\theta = 69° \pm 16°$ east of north. *This agrees rather well with findings of Grillmair et al. (1995).* This ellipticity is a reasonable match for that determined for more central regions of the cluster, within $12.5'$, for which we find $e = 0.07 \pm 0.03$. However, the position angle of the major axis for this central region, $\theta = 138° \pm 11°$ east of north, is somewhat different from the envelope and may possibly indicate isophotal twisting (although this is not clearly evident from the density maps).

Significance of Individual Substructures

Beyond the main envelope of M2 exists a number of over-densities detected at the 2σ level in the DECam map. We label, and show the locations of these regions, in Figure 3.11.

[11] `http://www.astroml.org/`

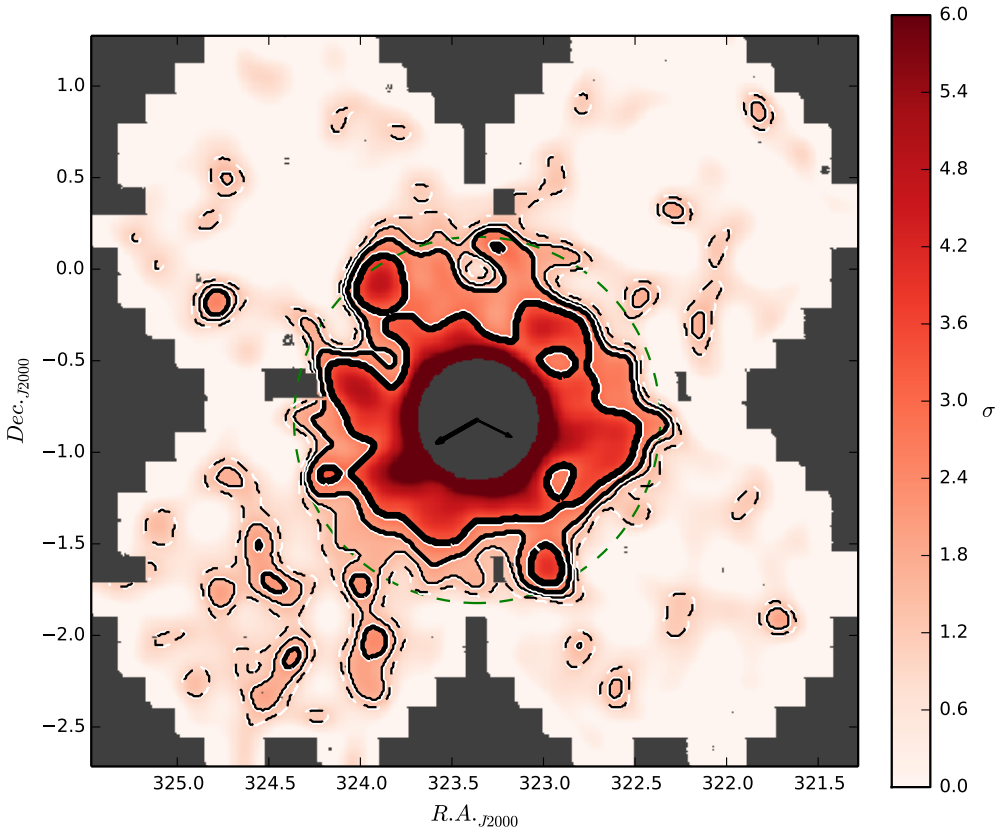

Figure 3.10: Stellar density distribution for the DECam catalogue split into $36'' \times 36''$ bins and smoothed using a gaussian kernel of width $4.8'$. As for Figure 3.9 the colour scale represents the number of standard deviations above the mean background value that a given bin sits. The dashed contours indicate a level corresponding to 1σ above the mean bin density. Contours representing the 1.5σ, 2σ and 3σ levels are shown by solid lines, increasing in thickness. A circular region of radius $20'$, almost twice the size of the nominal tidal radius, has been masked at the cluster centre. The outer dashed ring indicates a radius of $60'$. The arrows are the same as Figure 3.9.

Following Roderick et al. (2015), we employed a Monte Carlo simulation to investigate the significance of the number of cluster stars within any given over-density with respect to the typical number of stars obtained in a random sampling of the stellar catalogue. This allowed us to determine whether the number of cluster stars within the over-density was most likely just due to a random fluctuation in the field, or represented a grouping potentially related to M2. To begin, the complete sample of DECam stars (cluster and foreground stars alike) was sorted into different sets based on their location inside an identified over-density or not. We defined a control group to be the set of all stars not located inside the 2σ over-density in question, creating two sets of stars per over-density. For each region, we counted both the total number of stars and the number of these with

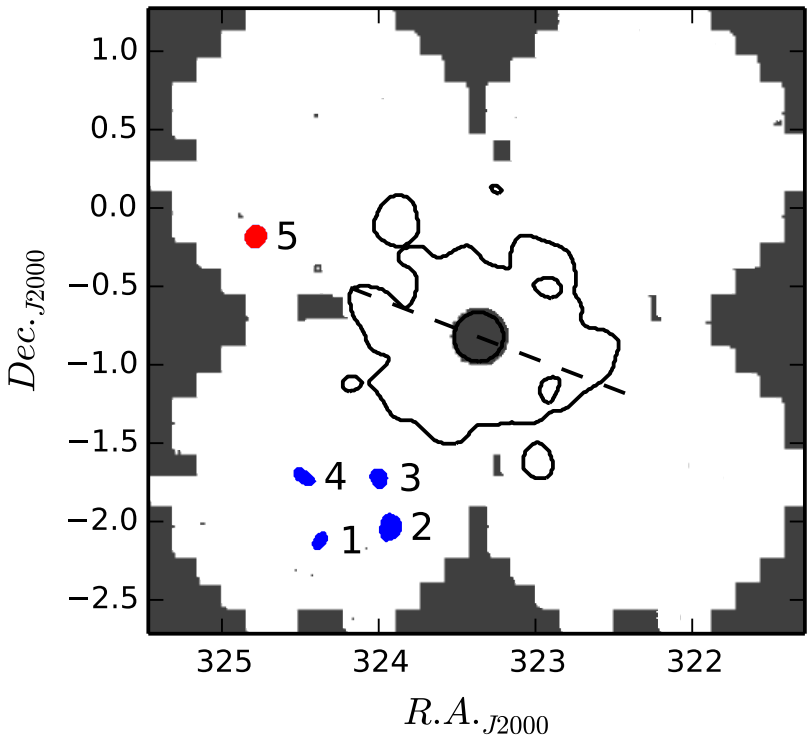

Figure 3.11: Over-density detections at the 2σ level in the DECam map. The red detection is considered significant ($\zeta > 3$), while the blue indicates $\zeta < 3$ detections. The dashed line indicates the position angle of 69°. The envelope of M2 at the 3σ level is also plotted. The binning and smoothing parameters are the same as for Figure 3.10.

weight > 0.2. Next, for a given over-dense region, we randomly selected the same total number of stars from the corresponding control sample, and determined the number of these with weight > 0.2. We repeated this sampling process 1000 times per region, and then compared the observed number of stars with weight > 0.2 for a given region to the distribution bootstrapped from the control set. Specifically, we assigned each over-dense region a value, ζ, defining how many standard deviations the true observed number of high-weight stars (N_{OD}) sits away from the mean of the control distribution ($\overline{N}_{CS}$) (see Roderick et al. 2015):

$$\zeta = \frac{N_{OD} - \overline{N}_{CS}}{\sigma_{CS}} \tag{3.2}$$

The mean and standard deviation (σ_{CS}) of each control distribution was determined by fitting a gaussian function to the sampled counts. The results of this significance testing are given in Table 3.4. We deemed a detection to be significant if the number of high-weight stars in that over-density was 3σ or more above the mean of the control distribution

Table 3.4: Over-dense regions and the results of our significance testing procedure.

Detection	N_{OD}	$\overline{N}_{CS}$	σ_{CS}	ζ
1	8	3.99	1.81	2.19
2	12	8.23	2.60	1.45
3	11	5.70	2.26	2.35
4	8	5.46	2.21	1.15
5	18	7.44	2.65	3.94

(i.e. $\zeta > 3$); Only one of the five potential over-densities (number 5) was found to be significant. The CMD for the over-dense region is presented in Figure 3.12, together with the respective ζ value.

3.4 Discussion

3.4.1 Nature of the Substructure Around M2

Using deep imaging from MegaCam and DECam we have revealed the existence of an extended, diffuse stellar envelope surrounding the globular cluster M2. This structure extends to a radius of at least $60'$, or ≈ 210 pc, from the centre of the cluster (according to the 3σ contour in our DECam density map), and possibly as far as $\sim 100'$, or ≈ 335 pc (according to our radial surface density profile). This corresponds to at least five times the nominal tidal radius of M2 from the literature (see Harris 1996a). We find the envelope to be rather smooth and nearly circular – its ellipticity is very mild ($e \approx 0.11$) and there is no obvious two-arm structure that might indicate the presence of classical tidal tails as seen around, for example, Palomar 5 or NGC 5466 (e.g., Odenkirchen et al. 2001; Belokurov et al. 2006a; Grillmair & Johnson 2006). This differs from the conclusions of Grillmair et al. (1995), who found extra-tidal stars surrounding M2, but suggested this was likely in the form of tidal tails.

The surface density of the envelope surrounding M2 follows a power-law decline with radius, of index $\gamma = -2.2 \pm 0.2$. Integrating the radial density profile allows us to estimate the ratio of mass in the envelope to the total mass of the cluster+envelope system. Examining our density profile (Figure 3.8) we see that at radii smaller than $\sim 10'$ the literature King (1962) model provides a good parametrization of the data; our new star counts begin diverging from the model outside this radius. We thus integrated the King model out to $10'$, and beyond this our DECam profile out to the 3σ detection limit of the envelope at $60'$. We consider everything outside the nominal literature tidal radius

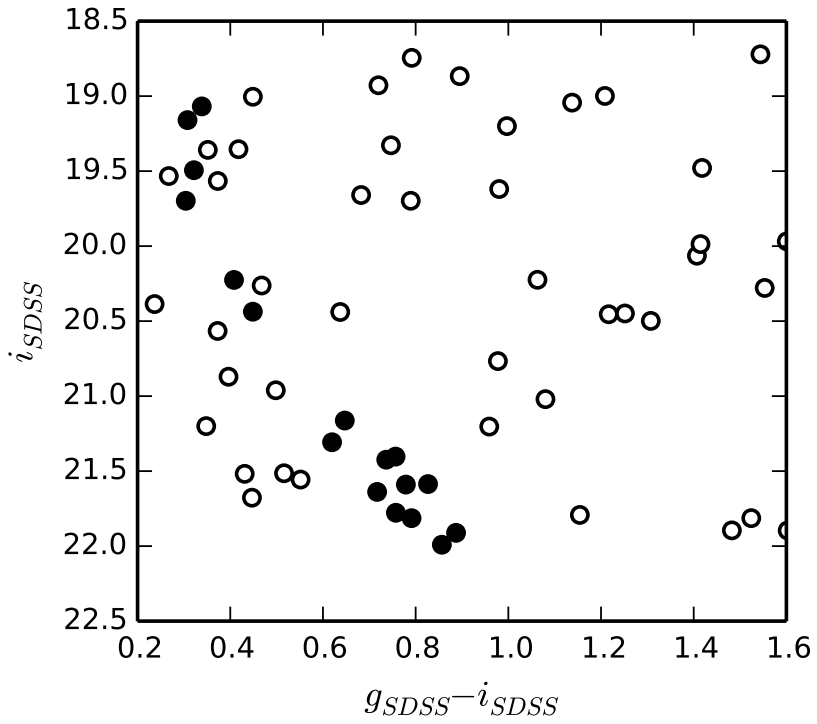

Figure 3.12: DECam CMD for detection 5 with a $\zeta = 3.94$. The point style indicates the weight value – filled points have weight ≥ 0.2, while empty points correspond to weights < 0.2.

of 12.5′ to constitute the envelope. With this definition, and ignoring the effect of mass segregation towards the cluster centre, our calculations reveal that the envelope comprises $\sim 1.6\%$ of the total mass of the cluster+envelope system.

One other Milky Way globular cluster, NGC 1851, is known to possess a substantial extended envelope component similar to that which we have revealed around M2 (e.g., Olszewski et al. 2009; Marino et al. 2014). The size of the envelope belonging to NGC 1851 is ≈ 250 pc in radius, very similar to what we have observed for the envelope surrounding M2. It is also seen to follow a power-law decline in surface density with radius, although the slope may be shallower than we have observed for M2, with index $\gamma = -1.24 \pm 0.66$, and it likely contains a smaller fraction ($\sim 0.1\%$) of the total mass of the system (Olszewski et al. 2009).

Beyond the apparent edge of the M2 envelope, we have discovered a statistically significant over-density of cluster-like stars (detection 5; see Figure 3.12). On the sky this over-density is located along the axis suggested by the orientation of the major axis of the envelope, which sits at a position angle $\theta = 69^\circ \pm 16^\circ$ east of north (see Figure 3.11). This

may suggest a preferred axis for the overall M2 system; interestingly, this axis is quite well aligned with the direction of the Galactic centre from M2 (see Figure 3.10). It is not clear whether the over-densitiy that we have detected might constitute an individual piece of M2 or its envelope, perhaps stripped via tidal forces, or whether it could represent a density peak in an even more extended envelope component that falls below the faint surface-brightness detection limit of our observations (note that the apparent "edge" of the envelope as seen in Figure 3.10 is due to our imposing a 3σ cut-off to the contouring, rather than actually comprising a physical boundary to the system).

The origin of M2's diffuse stellar envelope is not clear from the presently available data. We can think of two simple scenarios: (i) the envelope is a natural product of the dynamical evolution of the cluster, perhaps driven by external tidal forces or shocks, or (ii) M2 is a globular cluster that belonged to, or was the nucleus of, a dwarf galaxy that was accreted by the Milky Way and destroyed, leaving behind the cluster+envelope system.

We first explore the possibility that the envelope is a product of the dynamical evolution of M2. Proper motion measurements and orbital models from Dinescu et al. (1999) place M2 on a rather elliptical orbit ($e \approx 0.7$) with a period of $\sim 650 - 850$ Myr, a perigalactic radius of ~ 6 kpc, and an apogalactic radius of up to ~ 40 kpc. Assuming this has not evolved significantly in the past, over a Hubble time M2 would have traversed of order ≈ 15 orbits, and, as a consequence, has undergone multiple disk passages and shocks. Such events are known to accelerate the escape of stars from clusters, and hence speed up their dynamical evolution and ultimate disruption (e.g., Gnedin & Ostriker 1997).

Models of globular cluster evolution show that stars that become energetically unbound upon crossing the Jacobi radius (where the internal gravitational acceleration equals the tidal acceleration) through the Lagrange points to form tidal tails which can be very long but have a width roughly equivalent to that of the cluster (see e.g., Combes et al. 1999; Küpper et al. 2010a; Renaud et al. 2011, and references therein). A number of striking examples are known in the Milky Way halo – for example, Palomar 5 and NGC 5466 as noted above. M2 presently sits about 7 kpc below the Galactic plane, and has a large velocity component in the negative Z direction (i.e., away from the plane Dinescu et al. 1999). Hence it is likely that M2 has recently passed through perigalacticon and suffered a disk shock, such that its extended envelope, and indeed the more remote over-densities, might plausibly reflect a wave of escaping stars. However, we find no evidence for narrow tidal tails, – the envelope is rather evenly distributed in azimuth and is, in any case, *much*

wider than the cluster.

Models of the formation of tidal tails (see e.g., Küpper et al. 2010b) show that stars with sufficient energy to escape the cluster can take many dynamical times to move through the Lagrange point. During this stage these stars preferentially populate the outermost regions of the cluster and can form a halo-like structure that deviates from a King profile around the Jacobi radius. However, we do not believe the envelope of M2 is due to this type of process. Küpper et al. (2010b) find that except for clusters near core collapse, the King tidal radius fitted from a surface density profile is in general a reasonably close approximation to the Jacobi radius, with r_t/r_J in the range $\sim 0.8 - 1.2$. For M2, we find that the tidal radius of $12.5'$ listed in the Harris catalogue provides a good description of the surface density profile; indeed we observe deviation to a power-law profile to begin at approximately this radius. Küpper et al. (2010b) further show that beyond the Jacobi radius, unbound material tends to obey a power-law fall-off with a slope of $\gamma \sim -4$ to -5. Steep profiles like this are seen for many globular clusters (e.g., Carballo-Bello et al. 2012), but we observe a much shallower profile with $\gamma = -2.2$ for M2. Küpper et al. (2010b) find that clusters near apogalacticon can have shallower power-law indices up to $\gamma \sim -1$. Note however that, according to the orbit calculation by Dinescu et al. (1999) and Allen et al. (2006), M2 should be currently far from apogalacticon, although significant uncertainties in its actual orbital path are present[12].

Simulations modelling the formation of tidal tails (e.g., Lee et al. 2006) show that the debris lost from a cluster ought to appear spatially elongated at a few Jacobi radii from the centre. However, we do not observe substantial elongation of the M2 envelope out to ~ 5 times the Jacobi radius. While we cannot rule out the possibility that we are seeing tidal tails lying along, or close to, the line-of-sight vector, i.e., seen end on, this projection is statistically unlikely.

It is also relevant that that M2 is not particularly vulnerable to disk shocks due to its relatively high mass; Gnedin & Ostriker (1997) find that the combined effect of disk and bulge shocks on M2 (as quantified by the "destruction rate" due to these processes) is comparable to that of internal two-body relaxation (see also Dinescu et al. 1999; Allen et al. 2006).

Given that M2 spends a large proportion of its orbit at much larger Galactocentric

[12] *It should be noted, as well, that the slope of the observed power-law profile may be different for different viewing angles to the cluster. Therefore, the power-law description we have found may not be strong enough evidence on its own to disregard an origin of the tidal debris from dynamical processes.*

radii than where it is presently located, it is reasonable to ask whether evolution in a more benign environment might facilitate the production of a diffuse envelope. It is known that very isolated clusters tend to build up a surrounding halo of stars that have been scattered on to radial orbits by two- or three-body encounters in the inner regions of the cluster, and that the resulting density profile ought to possess a power-law decline, in projection, of index $-2.5 \lesssim \gamma \lesssim -2.3$ (see e.g., the discussion in Mackey et al. 2010a). This is quite similar to what we observe for the envelope of M2; moreover, the time-averaged tidal radius for the cluster would be a factor of several larger than at its present location, which might allow the envelope to become populated. Arguing against this scenario is that it takes many relaxation times to establish the core-halo structure, and, furthermore, it is not clear whether this would survive repeated pericentre passages and disk shocks. It is relevant that the half-mass relaxation time for M2 is ~ 2.5 Gyr (Harris 1996a), which is substantially longer than its orbital period.

We now turn to the possibility that M2 was once part of a dwarf galaxy that was accreted and destroyed by the Milky Way. This hypothesis has previously been advanced to explain the envelope surrounding NGC 1851 (Olszewski et al. 2009), and the abundance patterns observed for stars in the envelope of NGC 1851 are compatible with this idea (Marino et al. 2014). Simulations performed by Bekki & Yong (2012) have demonstrated that a diffuse envelope can indeed form around the compact nucleus of a dwarf galaxy after the original host has been largely stripped away by tidal forces. M2 shares a number of unusual attributes in common with other Milky Way globular clusters that have been suggested to be remnant dwarf nuclei. In particular, it exhibits an internal dispersion in iron abundance in the form of three distinct stellar populations (Yong et al. 2014), that further subdivide into sub-populations according to variations in s-process element abundances, light element abundances, and helium abundances (Lardo et al. 2012, 2013; Milone et al. 2015). In this regard it is similar to ω Cen (e.g., Villanova et al. 2014), which has long been hypothesized to be a former dwarf galaxy nucleus; to M54 (e.g., Siegel et al. 2007; Carretta et al. 2010a), which is either the nucleus, or central globular cluster, of the Sagittarius dwarf (Ibata et al. 1995; Bellazzini et al. 2008); and indeed to NGC 1851 (e.g., Carretta et al. 2010c; Yong et al. 2015). It is also relevant that the overall size of the envelope that we have observed around M2, with a radius of *at least* ~ 210 pc, is not dissimilar in size to the half-light radii of many typical dwarf galaxies in the Local Group (McConnachie 2012).

The number of stripped dwarf nuclei with masses between $10^5 - 10^6$ $M_\odot$ in the Milky Way halo has been proposed by Pfeffer et al. (2014) to be between one and three, based on the Millennium II simulation and semi-analytic modelling[13]. However, as noted by these authors, this is lower than the number of objects already hypothesised to be stripped nuclei of this type. According to the criterion specified by Pfeffer et al. (2014) – that a globular cluster which is a former dwarf nucleus ought to have an internal spread in age and/or heavy element abundances – and the discussion above, M2 should also be considered a member of this category, increasing the possible tension between simulation and observation. However, the authors note that the Poisson uncertainties on their estimate are substantial, and could accommodate a larger number of systems. Moreover, it is not clear that their specified criterion uniquely identifies stripped dwarf nuclei. It is possible that the presence of an extended outer structure, as we have observed for M2, could constitute an additional marker.

If it is true that M2 was once a member of a now-defunct dwarf, the lack of a large stellar stream in the vicinity of the cluster (as is seen, for example, for the disrupting Sagittarius dwarf) may suggest that the dwarf galaxy that housed M2 was accreted very long ago. In this respect, the over-density that we have detected beyond the main envelope is potentially the only remaining fragment of that stellar stream in our field of view. As noted above, this over-density might also signify the presence of an even more extended envelope – perhaps stream-like in nature – that connects it to M2 but falls below the faint surface brightness threshold of our observations. In this regard, probing even further down the M2 main sequence could help detect such a feature, although the fact that this will have to be done over a relatively large area of sky might mean that we will need to wait for the advent of facilities such as the Large Synoptic Survey Telescope (LSST, Ivezic et al. 2008). Apart from this, spectroscopic follow-up of stars in the M2 envelope and the nearby over-density should help identify whether the envelope exhibits abundance patterns similar to those of the cluster, and confirm whether the over-density is truly related the cluster or not.

[13] *Due to the uncertainty in scaling the simulations, given the uncertainty in the mass of the Milky Way (e.g., McMillan 2017), the predicted number of stripped dwarf nuclei has a large uncertainty.*

3.5 Conclusions

We have searched the region surrounding the Milky Way globular cluster M2 for the presence of low surface brightness substructures, using deep wide-field imaging mosaics from MegaCam and DECam. We use the observed colour-magnitude diagram to identify likely cluster members across the respective fields of view, and find that a composite radial surface density profile indicates substantial extra-tidal populations extending well beyond the literature value for the tidal radius of 12.5′. The surface density declines with radius according to a power law with index $\gamma = -2.2 \pm 0.2$. These remote M2 populations entirely fill our $0.8^\circ \times 0.8^\circ$ MegaCam mosaic, and it is only with a ~ 13 square degree mosaic from DECam that we are able to identify a diffuse, extended envelope surrounding the cluster to a radial distance of at least 60′ (~ 210 pc), five times larger than the nominal tidal radius. Our two-dimensional density map reveals the envelope to be mildly elliptical, with $e = 0.11 \pm 0.06$ and the major axis oriented at a position angle of $\theta = 69^\circ \pm 16^\circ$ east of north. There is no evidence for a distinct stellar stream or tidal tails, although we identify a small but statistically significant over-density of M2 stars beyond the apparent edge of the envelope, that follows a potential axis extending from north-east to south-west in broad agreement with the orientation of the envelope.

The nature and origin of the diffuse envelope surrounding M2 is not well understood. One possibility is that this structure is due to the dynamical evolution of the cluster, although how external factors such as tidal shocking might give rise to such an envelope, as opposed to the distinct tidal tails observed around disrupting globular clusters and seen in numerical simulations, is not clear. Numerous globular clusters have been found with power-law extended profiles (e.g., Correnti et al. 2011; Carballo-Bello et al. 2012, 2014; McLaughlin & van der Marel 2005) without tidal tails, though none of these studies have a found an envelope to the size of, or exhibiting a profile a shallow as, M2. An alternative scenario is that M2 was originally formed in a dwarf galaxy that was later accreted into the Milky Way halo and destroyed – in this case the envelope might constitute the final remaining vestiges of the host. A similar structure has been observed to surround the globular cluster NGC 1851 (e.g., Olszewski et al. 2009; Marino et al. 2014), and simulations of this system have shown that the nucleus of a dwarf galaxy can possess a halo-like structure surrounding the dense core long after the majority of the original dwarf and its dark matter halo have been stripped away and lost (Bekki & Yong 2012). In this context it is intriguing that M2 is a member of a small group of massive Milky Way globular

clusters (also including NGC 1851) observed to exhibit internal dispersions in both iron abundance and s-process elements (e.g., Yong et al. 2014). Deeper imaging of the region around M2, together with spectroscopic velocity and abundance measurements of stars in the envelope, will be required to understand the origin of this structure with greater certainty.

3.6 Addendum

Please visit the works listed below for more information on the following topics:

- The ΛCDM cosmological model: Riess (1998); Peacock et al. (2001) and Planck Collaboration et al. (2016).
- Detections of tidal tails in globular clusters: Belokurov et al. (2006a); Chen & Chen (2010); Niederste-Ostholt et al. (2010); Jordi & Grebel (2010); Sollima et al. (2012); Balbinot et al. (2011); Myeong et al. (2017) and Navarrete et al. (2017).
- Chemical abundance variations in globular clusters: Marino et al. (2015).

Chapter 4

The Outer Envelopes of Globular Clusters - II. NGC 1261, NGC 1851 and NGC 5824

This chapter is based on the submitted article "The Outer Envelopes of Globular Clusters - II. NGC 1261, NGC 1851 and NGC 5824", P. B. Kuzma, G. S. Da Costa, A. D. Mackey. Submitted to the Monthly Notices of the Royal Astronomical Society. Minor typographical and grammatical changes have been made as a result of the Examiner Reports. Significant alterations to the original text, as suggested from the Examiner Reports, are shown in italics.

We present a second set of results from a wide-field photometric survey of the environs of Milky Way globular clusters. The clusters studied are NGC 1261, NGC 1851 and NGC 5824: all have data from DECam on the Blanco 4m telescope. NGC 5824 also has data from the Magellan Clay telescope with MegaCam. We confirm the existence of a large diffuse stellar envelope surrounding NGC 1851 of size at least 240 pc in radius. The radial density profile of the envelope follows a power-law decline with index $\gamma = -1.5 \pm 0.2$ and the projected shape is slightly elliptical. For NGC 5824 there is no strong detection of a diffuse stellar envelope, but we find the cluster is remarkably extended and is similar in size (at least 230 pc in radius) to the envelope of NGC 1851. A stellar envelope is also revealed around NGC 1261. However, it is notably smaller in size with radius ~105 pc. The radial density profile of the envelope is also much steeper with $\gamma = -3.8 \pm 0.2$. We discuss the possible nature of the diffuse stellar envelopes, but are unable to draw definitive conclusions based on the current data. NGC 1851, and potentially NGC 5824, could be stripped dwarf galaxy nuclei, as their large radial extent, and their internal spreads in iron

and s-process abundances make them akin to other globular clusters already suggested to be dwarf galaxy core remnants such as ω Cen, M54 and M2. On the other hand, the different characteristics of the NGC 1261 envelope suggest that it may be the product of dynamical evolution of the cluster.

4.1 Introduction

In recent times, a small group of Milky Way Globular Clusters (GCs) have been discovered to possess cluster-like stellar populations beyond their tidal boundaries. The spatial distributions of the extra-tidal populations are found to take two different forms. One takes the shape of two long axisymmetric streams that lead out from the cluster centre, otherwise known as tidal tails (e.g., Palomar 5; Odenkirchen et al. 2003; Grillmair & Dionatos 2006). This feature is suggested to form through the disruption of the parent GC by both internal processes and external tidal forces exerted by the Galaxy (e.g., Küpper et al. 2010b). The other is a diffuse stellar envelope that surrounds the cluster beyond its tidal radius (e.g., Olszewski et al. 2009; Carballo-Bello et al. 2014). It is currently unclear how diffuse stellar envelopes can form, as there are at least two different theories suggested for their origin.

One is that the diffuse stellar envelope may be a natural product of GC evolution in the Galactic tidal field. Simulations of tidal tail formation do show that a diffuse envelope may form during the disruption process, as stars begin to populate the outermost regions of the cluster before entering the tidal tails (Küpper et al. 2010b). Indeed, a number of Galactic GCs do show evidence of stellar envelopes, based on their surface density profiles, that possess similar traits to those seen in the simulations (e.g., see Carballo-Bello et al. 2012). Recent work has also shown that observational biases might influence the detection of tidal tails or a stellar envelope in some cases (Balbinot & Gieles 2017). The other suggested origin regards the stellar envelope as evidence for a cluster having an extra-galactic origin. Studies such as Olszewski et al. (2009) and Kuzma et al. (2016) have uncovered stellar envelopes that are unlike those expected to be produced during the formation of tidal tails. Further, the envelopes appear to embed massive clusters that have peculiar stellar properties, such as Fe and s-process element variations, which already make them distinct from more ”classic” Galactic GCs.

A number of Galactic GCs, whether they have peculiar stellar populations or not, have been linked to an extra-galactic origin. For example, a small handful of GCs are related to the tidal remains of the Sagittarius dwarf galaxy (Ibata et al. 1994; Da Costa &

Armandroff 1995; Law & Majewski 2010a); whose debris is in the form of a stellar stream that completely wraps around the Milky Way (e.g., Majewski et al. 2003; Yanny et al. 2009a, and references therein). Even in M31, our largest galactic neighbour, GCs are seen to inhabit or lie near to large scale stellar structures generated by the tidal disruption of dwarf galaxies (e.g. Ferguson et al. 2002; Mackey et al. 2010b, 2014; Huxor et al. 2014). Therefore, the envelopes may be the remnants of a long since accreted dwarf galaxy, with the rest of the stream remaining undetected.

We are searching for large scale streams in the Galactic halo, using GCs as potential tracers (Kuzma et al. 2016, hereafter Paper I). As GCs are seen to lie in or nearby streams in M31, looking at GCs in the Milky Way that hint at an extra-galactic origin with wide field photometry may result in the discovery of streams or some other kind of structure that may be the remnants of the GCs parent dwarf galaxy. Paper I introduced the survey and presented the results of the first cluster examined, NGC 7089 (M2). M2 has peculiar properties that hint at a potential accreted origin (see Paper I and references therein), and wide field imaging revealed that M2 is embedded in a low-mass stellar envelope, detected to a radius of at least ~ 210 pc, with no signs of a stellar stream or tidal tails. The next set of targets of this survey are the halo GCs NGC 1851, NGC 5824 and NGC 1261.

Many studies of NGC 1851 over the past decade have revealed that the cluster is not a typical Milky Way GC. NGC 1851 is a relatively massive globular cluster, $M_v = -8.33$, located at 12.1 kpc from the sun (Galactocentric distance: 16.6 kpc) (Harris 1996b, 2010 edition). Amongst its peculiarities is a double sub-giant branch in the colour-magnitude diagram (Milone et al. 2008). Other anomalies include a range in C+N+O abundance among the cluster red giants (Yong et al. 2009; Ventura et al. 2009; Yong et al. 2015, and references therein), and star-to-star variations in [Fe/H] and s-process elements (Yong & Grundahl 2008; Carretta et al. 2010c; Gratton et al. 2012b). The two sub-giant branch populations correlate with the observed abundance variations, as the brighter sub-giant branch is metal-poor and under-abundant in s-process elements compared to the fainter sub-giant population. Lastly, Olszewski et al. (2009) uncovered the existence of a stellar halo surrounding the cluster, that is at least 500pc in diameter. NGC 1851 halo stars have been identified through radial velocities (e.g., Marino et al. 2014; Navin et al. 2015) and have been found to exhibit the same s-process abundance patterns as the bright sub-giant branch stars within the cluster, confirming that the envelope is directly related to NGC 1851 (Marino et al. 2014).

The origin of the halo embedding NGC 1851 has been the source of much speculation. Olszewski et al. (2009) discussed its formation in terms of originating from the cluster. This scenario is suggested as unlikely due to the lack of evidence for tidal tails in their observations. The second suggestion made by the authors is that the halo is evidence for NGC 1851 being the core a dwarf galaxy that has been accreted by the Milky Way. As discussed above, NGC 1851 has anomalies in common with a group of Milky Way GCs that all have been linked to the remains of, or belonging to, an accreted dwarf galaxy (e.g., M54, ω Cen, M2). Bekki & Yong (2012) modelled the halo/cluster system of NGC 1851, exploring different potential formation scenarios. They found NGC 1851 could have formed in the central regions of a dwarf galaxy as a product of GC-merging at the center, or be the actual nucleus itself. Regardless of which scenario, the models predict what we currently observe as regards the envelope of NGC 1851.

NGC 5824 ($M_v = -8.85$, heliocentric distance: 32.1 kpc), the third target of this study, shows some of the same characteristics as NGC 1851 and M2. It may have a [Fe/H] abundance spread: Da Costa et al. (2014) investigated the alluring result of a possible Fe spread in NGC 5824 by Saviane et al. (2012), inferred from medium-resolution spectroscopy of the Ca II triplet. Da Costa et al. (2014) found a ~ 0.3 dex range in [Fe/H] across their sample of red giant branch stars. However, a recent analysis based on high dispersion spectra of NGC 5824 red giants by Roederer et al. (2016) excluded the existence of a Fe-spread of this size. Nevertheless, Roederer et al. (2016) also showed that NGC 5824 has a large [Mg/Fe] variation and that one star in their sample has significantly higher s-process element abundances than the others.

The cluster also satisfies the criteria of possessing cluster stars that exist beyond the tidal radius. Grillmair et al. (1995) included NGC 5824 in their search for GCs with tidal tails. Their star counts revealed a radial profile that deviates from a King model near the tidal radius and continues to drop off at rate well described by a power law, $\gamma = -2.2 \pm 0.1$ (Da Costa et al. 2014). More recently, Carballo-Bello et al. (2012) presented a density profile of NGC 5824 in their sample of globular clusters observed with the ESO Wide Field Camera and also found a profile that is described by a power law ($\gamma = -2.62$). Newberg et al. (2009) presented a possible connection of NGC 5824 with the Cetus Polar stream, based on orbit calculations for the stream. However, later follow up analysis of the spatial distribution of cluster stars by Carballo-Bello et al. (2014) did not reveal any extended structure.

Table 4.1: A brief list of parameters for the clusters in this paper.

Parameter	NGC 1261	NGC 1851	NGC 5824
R. A.[1]	03:12:16	05:14:07	15:03:59
Dec.[1]	–55:12:58	–40:02:48	–33:04:06
l	270.54	244.51	332.56
b	-52.12	-35.03	22.07
$[Fe/H]$[2]	–1.27	–1.18	–1.94
Solar dist. (kpc)	16.3	12.1	32.1
Galactocentric dist. (kpc)	18.1	16.6	25.9
M_v[3]	-7.8	-8.33	-8.85

References: [1] Goldsbury et al. (2010), [2] Carretta et al. (2009), [3] Harris (1996a) (2010 edition)

The fourth and final cluster in this paper is NGC 1261. It is slightly further away than NGC 1851, 16.3 kpc, and it is a little fainter, $M_v = -7.80$. It has no known measured internal Fe-dispersion, though there is tantalising suggestion of a potentially small population with a heavy element dispersion in the chromosome maps of Milone et al. (2017). This metal-poor cluster was part of the Carballo-Bello et al. (2014) sample, and these authors claim the potential existence of stellar population beyond 1.5 times the tidal radius determined in Carballo-Bello et al. (2012). The authors do not suggest whether this extra population is in tidal tails, or is an envelope, or a sign of a larger stellar stream. They lament their lack of sufficient spatial coverage to investigate more fully the origin. Quite recently, Balbinot et al. (2016) present a new discovery of a stellar stream, the Phoenix stream, in the Dark Energy Survey's first year data that lies in the direction of NGC 1261, presenting a promising connection at first. However, the authors comment that there is no clear connection between NGC 1261 and the Phoenix stream. The authors also dismiss a potential connection between the stream, NGC 1261 and the newly discovered Eridanus-Phoenix over-density, a stellar structure that is same direction and at a similar heliocentric distance (Li et al. 2016) as the cluster.

This paper presents the results of wide-field imaging, using MegaCam and the Dark Energy Camera (hereafter DECam), of NGC 1851, NGC 5824 and NGC 1261. A brief list of parameters for these clusters is presented in Table 4.1. The observations and the reduction techniques involved are discussed in the following section, while in section 3 we present our results. We analyse our findings in section 4 and discuss the results in section 5. Our concluding comments are presented in section 6.

4.2 Observations and Data reduction

4.2.1 Observations

The observations of NGC 1851 and NGC 5824 were taken with the Dark Energy Camera (DECam; Flaugher et al. 2015) on the 4-m Blanco telescope at Cerro Tololo Inter-American Observatory. DECam, a mosaic imager, has 62 CCDs arranged in a near circular pattern with each CCD containing 2048 x 4096 pixels. Each cluster was observed as sets of three dithered exposures in the g and i filters with five separate pointings. The pointings are a central one and four locations along the diagonals that define an x-shape (see Fig. 4.1). The observations for NGC 1851 were taken on February-17, 2013, while the observations for NGC 5824 were performed on the August-13, 2013, and February-26, 2014. The exposure time for NGC 1851 was 200 sec for both filters, and saw mostly consistent seeing: g seeing was between 0.92″ - 1.02″ and 0.83″ - 0.96″ for the i images. We adopted the seeing as the full-width at half-maximum (FWHM) of the stellar images. NGC 5824 had a slightly longer exposure time, 360 seconds per exposure for both filters, and more variable seeing. The g observations had seeing between 1.25″ - 1.67″, and the i observations had a range of 1.13″ - 1.25″. A second set of observations for the central pointing of NGC 5824 was obtained with significantly shorter exposure time, 10 seconds, on March-06, 2016, in both filters for the purposes of photometric calibration.

The final set of DECam observations, for NGC 1261, was obtained on February-28, 2014. Unlike NGC 1851 and NGC 5824, NGC 1261 had only one field taken, dithered three times, with the cluster in the center. Exposures were shorter for g (250s) with rather consistent seeing conditions (1.03″ - 1.07″) than for i (360s), which had slightly variable seeing (0.80″ - 0.92″). All the observations were processed through the DECam community pipeline reduction pipeline[1] (Valdes et al. 2014). NGC 5824 also had a set of observations obtained with MegaCam (McLeod et al. 2015) on the 6.5-m Magellen Clay telescope at Las Campanas Observatory, undertaken on June-14 and June-15, 2013. Nine pointings, dithered three times, were observed in a three by three grid, with the central observation containing NGC 5824 itself (Fig. 4.1, bottom right). The g observations were exposed for 90 seconds, and saw seeing variability between 0.96″ - 1.33″. The i observations used a 300 second exposure time, and had seeing in the range 0.77″ - 1.15″. The observations were processed and reduced at the Harvard-Smithsonian Center for Astrophysics with the

[1] `http://www.ctio.noao.edu/noao/content/dark-energy-camera-decam`

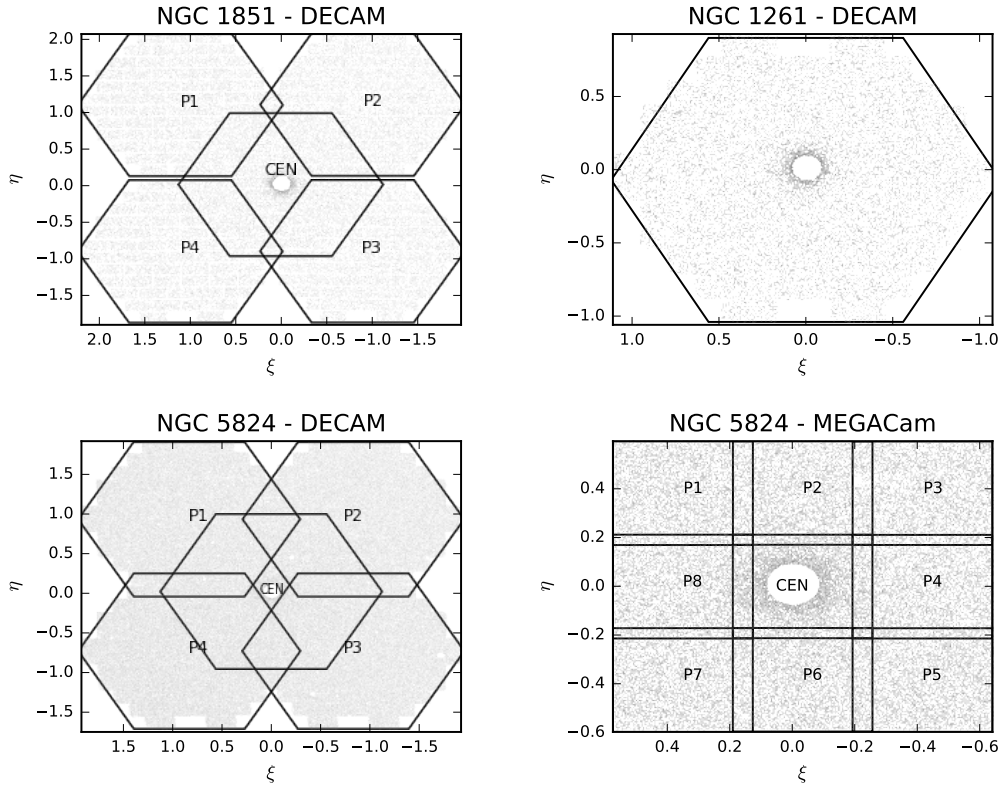

Figure 4.1: Locations of the fields of view in this study, plotted on the gnomonic projection (ξ, η) in degrees. Also plotted are the stars extracted from the images. Due to crowding, we have excluded the inner regions of the clusters. North is up and East is to the left. Regions excluded: NGC 1851 - 6 arcmin radius, NGC 1261 - 5 arcmin, NGC 5824 (both cameras) - 5 arcmin.

MegaCam pipeline [2] (see McLeod et al. 2015). *Table 4.3 presents the details of the NGC 5824 MegaCam observations utilised in this work.*

4.2.2 Photometry

The entire pipeline that takes the reduced photometric images to a workable photometric catalog is discussed in detail in Paper I; here we will outline the major components. The software package Source Extractor[3] (SExtractor; Bertin & Arnouts 1996) was used to perform aperture photometry on the non-stacked, individual photometric images. Each resulting image catalog was cleaned of spurious and non-stellar objects through a combination of SExtractor output flags and magnitude differences between different aperture sizes. The cleaned g and i catalogs for each image were cross-matched using the freely available software, Stilts (Taylor 2006).

[2] `http://hopper.si.edu/wiki/piper/Megacam+Data+Reduction`
[3] `https://www.astromatic.net/software/sextractor`

Table 4.2: Listing of the observations from DECam employed in this work.

Cluster	Date	Field Name	Field Center		N_{exp}	Exp. Time	Filter	seeing (arcsec)		
			R.A. (J2000)	Dec. (J2000)		per frame (secs)		1	2	3
NGC 1851	17-Feb-2013	CEN	05:14:38	-39:57:10	3	200	g	0.97	1.02	0.96
					3	200	i	0.87	0.86	0.83
		P1	05:09:30	-38:57:10	3	200	g	1.02	0.96	0.93
					3	200	i	0.86	0.83	0.89
		P2	05:19:49	-38:57:11	3	200	g	0.96	0.93	0.92
					3	200	i	0.83	0.89	0.88
		P3	05:09:22	-40:57:17	3	200	g	0.93	0.92	1.01
					3	200	i	0.89	0.88	0.85
		P4	05:20:00	-40:57:17	3	200	g	0.92	1.01	0.95
					3	200	i	0.88	0.85	0.96
NGC 5824	26-Feb-2014	CEN	15:04:02	-33:08:10	3	360	g	1.62	1.67	1.61
					3	360	i	1.25	1.21	1.14
	13-Aug-2013	P1	15:00:03	-32:08:44	3	360	g	1.67	1.61	1.59
					3	360	i	1.21	1.14	1.15
		P2	15:07:55	-32:08:40	3	360	g	1.61	1.59	1.41
					3	360	i	1.14	1.15	1.16
		P3	14:59:58	-33:48:46	3	360	g	1.59	1.41	1.25
					3	360	i	1.15	1.16	1.13
		P4	15:07:59	-33:48:46	3	360	g	1.41	1.25	1.38
					3	360	i	1.16	1.13	1.16
	06-Mar-2016	CEN	15:04:02	-33:08:10	3	10	g	1.54	1.54	1.64
					3	10	i	1.38	1.36	1.25
NGC 1261	28-Feb-2014	CEN	03:12:26	-55:16:07	3	250	g	1.06	1.03	1.07
					3	360	i	0.92	0.83	0.80

Table 4.3: Listing of the observations from MegaCam employed in this work.

Cluster	Date	Field Name	Field Center		N_{exp}	Exp. Time	Filter	seeing (arcsec)		
			R.A. (J2000)	Dec. (J2000)		per frame (secs)		1	2	3
NGC 5824	15-Jun-2013	CEN	15:03:49	-33:04:06	3	90	g	1.07	1.22	1.24
					3	300	i	0.86	1.15	1.03
	15 -Jun-2013	P1	15:05:38	-32:41:06	3	90	g	1.22	1.26	1.06
					3	300	i	1.15	1.03	0.78
	14-Jun-2013	P2	15:03:49	-32:41:06	3	90	g	1.24	1.06	1.15
					3	300	i	1.03	0.78	0.93
	14-Jun-2013	P3	15:01:59	-32:41:06	3	90	g	1.06	1.15	1.33
					3	300	i	0.78	0.93	1.13
	14-Jun-2013	P4	15:01:59	-33:04:06	3	90	g	1.15	1.33	1.24
					3	300	i	0.93	1.13	0.95
	15-Jun-2013	P5	15:01:59	-33:27:06	3	90	g	1.33	1.24	1.07
					3	300	i	1.13	0.95	1.01
	15-Jun-2013	P6	15:03:49	-33:27:06	3	90	g	1.24	1.07	1.28
					3	300	i	0.95	1.01	0.90
	15-Jun-2013	P7	15:05:39	-33:27:06	3	90	g	1.07	1.28	1.12
					3	300	i	1.01	0.90	0.81
	15-Jun-2013	P8	15:05:39	-33:04:06	3	90	g	1.28	1.12	0.96
					3	300	i	0.90	0.81	0.77

Table 4.4: The parameters used to calibrate our instrumental photometry to the SDSS system.

Cluster	Filter	Calibration	
		Zero Point	Colour Coeff.
NGC 1851	g	30.755 ± 0.002	-0.016 ± 0.001
	i	31.753 ± 0.002	0.002 ± 0.001
NGC 1261	g	30.829 ± 0.002	-0.015 ± 0.001
	i	31.289 ± 0.002	0.001 ± 0.001

Once each image had their g and i catalogs generated, all catalogs belonging to the same field were combined to create a single stellar catalog for each field. Before this occurred, however, the catalogs were adjusted to be placed on the same photometric scale. The image with the deepest photometry was designated the master image, and the remaining two images were adjusted to the master by determining the median photometric difference with stars observed in other two images. The single stellar catalogs for each field were then calibrated to a master field using the same techniques: for DECam and MegaCam, that field was the central pointing (CEN). NGC 1261 only had one pointing, therefore no cross-field calibrations were necessary.

Finally, the complete catalogs were transferred to a known photometric scale from the raw instrumental magnitudes. For NGC 1851 and NGC 1261, we cross matched stars with a catalog belonging to the Dark Energy Survey (DES; The Dark Energy Survey Collaboration 2005), which is calibrated to the Sloan photometric scale and is presented in Koposov et al. (2015). Table 4.4 displays our photometric calibration corrections (zero point and colour terms) for those two clusters. As for NGC 5824, the short exposure set of DECam observations for the central pointing (CEN) was used to calibrate the instrument photometry to APASS (Henden et al. 2009, 2015), which is also on the Sloan photometric scale. Using stars in common again, we calibrated the shallower photometry to the APASS catalog. From there, the deeper imaging was calibrated to the shallow DECam imaging. Finally, the MegaCam catalog was then scaled to APASS through the stars that were mutually observed in DECam and MegaCam. Table 4.5 lists the zero points and colour terms of the NGC 5824 photometric corrections.

4.2.3 Artificial Star Tests

To test the recovery rate of the pipeline and to explore the completeness across the mosaics, we have performed artificial star tests on all the observations *using a Moffat function for the*

Table 4.5: The parameters used to calibrate our NGC 5824 instrumental photometry to the APASS system.

Camera	Filter	Calibration	
		Zero Point	Colour Coeff.
MegaCam → APASS	g	30.987 ± 0.006	−0.174 ± 0.003
	i	31.610 ± 0.002	0.012 ± 0.001
DECam → APASS	g	31.321 ± 0.006	−0.028 ± 0.006
	i	31.285 ± 0.0008	0.039 ± 0.007

PSF. 10000 stars and 2000 stars were inserted for DECam and MegaCam respectively. The artificial stars were the brightest at 18^{th} magnitude, and increased in frequency towards the faint limit of 27^{th} magnitude. Stars were deemed 'recovered' if they passed through the same pipeline described in the previous section. This process was repeated 10 times, to create a sizeable sample of stars for each camera. For DECam, this amounted to 100000 stars per field, and 20000 stars for MegaCam.

To ensure variable completeness does not influence the results we limited all the photometry to the 90% completeness magnitude for the field with the shallowest photometry (see Fig. 4.2). With respect to NGC 1851, this photometric limit was set in g by P3: g= 23.0, while in i each field appeared consistent with each other and the limit is i= 22.3. The corresponding 90% completeness for NGC 1261 are 23.4 in g and 22.6 in i. As for NGC 5824, the cluster is considerably more distant than the others. Therefore, to maximise coverage of the main sequence, we adopted a 50% cut rather than 90%. This allowed increased photometric depth without the photometric uncertainties becoming too large. For DECam, this corresponded to 23.4 in g and 22.7 in i. MegaCam's corresponding magnitudes were 23.7 and 22.8 for g and i respectively. We also explored the completeness as a function of radius from the cluster center to examine the radius that relative completeness becomes affected by crowding. When completeness became significantly affected, we excluded all detections within the corresponding radius. This radius was $6'$ for NGC 1851 and $5'$ for NGC 1261 and NGC 5824. However, we affirm that our analysis is predominately undertaken outside the limiting radii of our clusters. At these distances, the completeness curves in our fields do not vary significantly.

4.2.4 Extinction

Fig. 4.3 displays the extinction in the field of view for our observations from the dust maps presented by Schlegel et al. (1998). NGC5824 is affected by a severe amount of variable

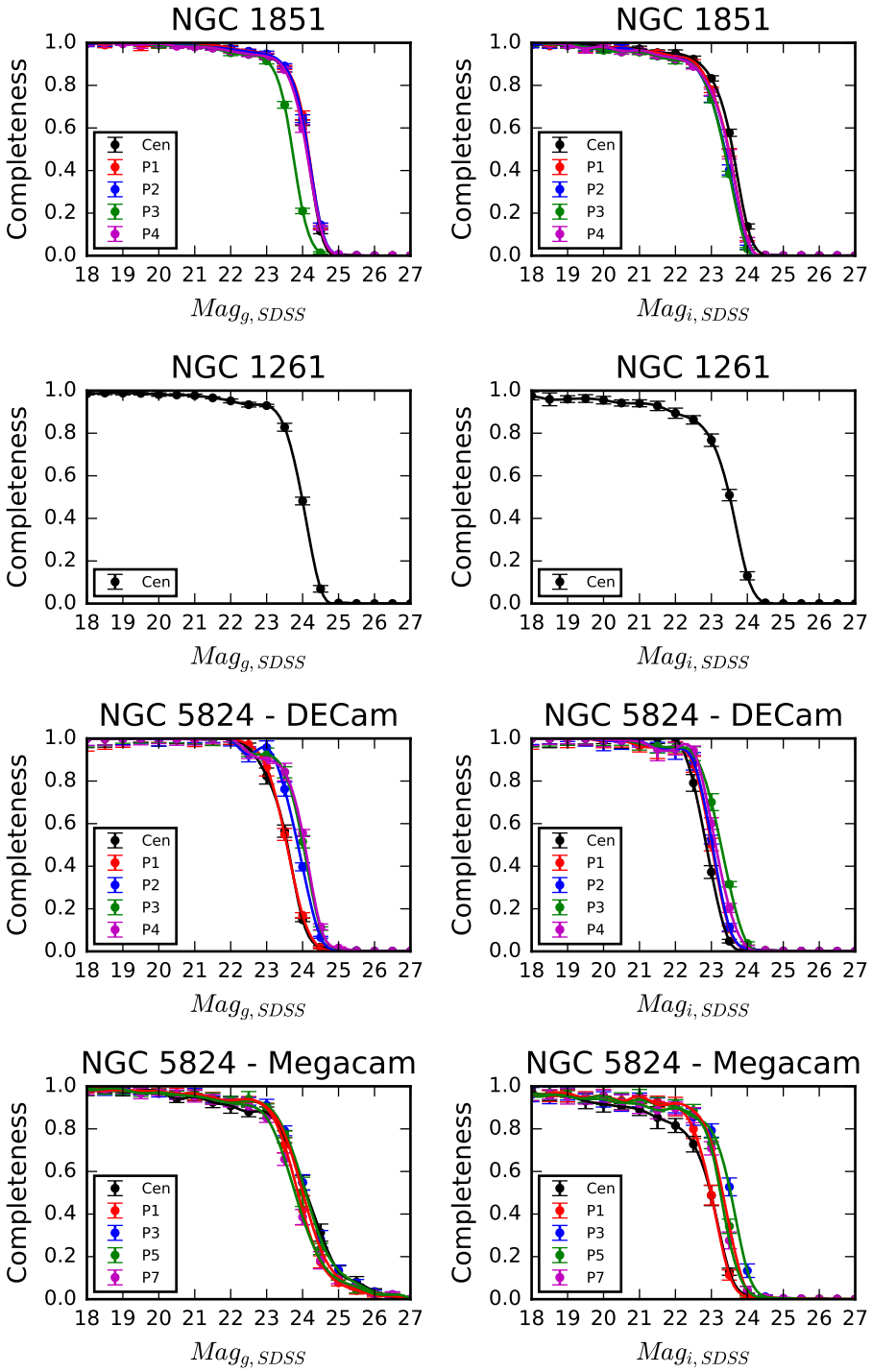

Figure 4.2: Completeness for our set of observations, along with a best fit cubic spline. For clarity, we display only a subset of completeness curves for the MegaCam observations of NGC 5824.

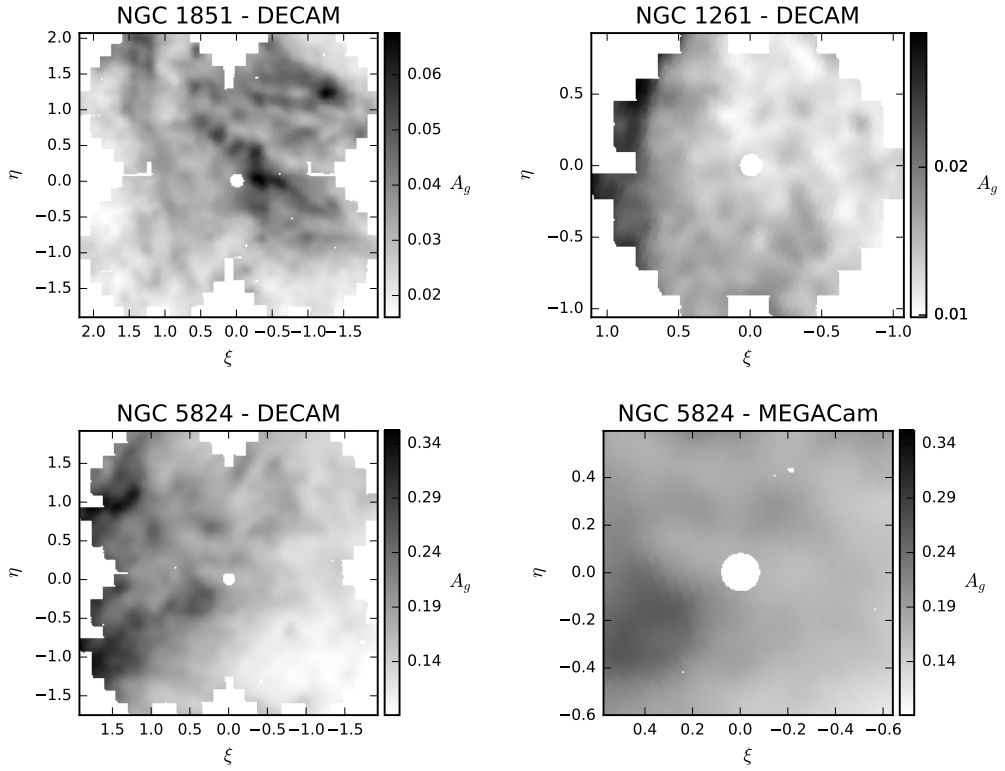

Figure 4.3: The A_g extinction maps for across the fields (Schlegel et al. 1998; Schlafly & Finkbeiner 2011). Note the strong variable reddening across the DECam imaging of NGC 5824.

reddening along our line of sight, $0.09 \leq A_g \leq 0.35$. This is seen as well for NGC1851 and NGC 1261 ($0.01 \leq A_g \leq 0.07$ and $0.01 \leq A_g \leq 0.03$, respectively), though not at the same level of severity. If not taken into consideration, much like relative completeness across the fields of view, the variable reddening may lead to apparent low surface brightness features that are a product of reddening and not real. After the photometric cuts due to completeness, we corrected each star individually for reddening (now denoted g_0 and i_0) and performed another photometric cut based on the level of reddening. We found the region in the fields that had the most severe level of extinction and removed all stars from the catalogs that were fainter than the limiting magnitude of that region. This meant all stars fainter than 22.7 in g_0 and 22.2 in i_0 were removed for NGC 1851. As for NGC 5824, the new DECam limits were 22.9 and 22.1 in g_0 and i_0 respectively, and 22.9 (g_0) and 22.4 (i_0) for MegaCam. Finally, the new photometric limits for NGC 1261 are 23.2 in g_0 and 22.5 in i_0.

4.2.5 Complete Catalog

The complete DECam photometric catalogs of our three clusters are displayed in the colour-magnitude diagrams (CMD) in Fig. 4.4. The main sequence and the main sequence turn-off are clearly visible in all clusters, as well as a noticeably populated blue horizontal branch for NGC 5824. We have removed the field dwarfs from any subsequent analysis as they are clearly contaminants not related to the cluster population. This means we removed stars with $(g_0 - i_0) > 1.6$ in the catalogs belonging to NGC 1851 and NGC 1261, and $(g_0 - i_0) > 0.8$ for NGC 5824. As is evident in Fig. 4.4, the red giant branch in all three cluster CMDs is essentially undetectable against the field contamination, while the main sequences are readily visible. Consequently, we decided to use only stars fainter than approximately the level of the main sequence turnoff in the analysis. The cutoff magnitudes were $i_0 = 18.5, 19.0$ and 20.5 for NGC 1851, NGC 1261 and NGC 5824, respectively. Fig. 4.5 displays the CMD for the NGC 5824 MegaCam catalog. This catalog underwent the same photometric cuts as the DECam catalogs.

4.3 Results

In this section we present our results using the techniques previously discussed in depth in Paper I, unless otherwise specified. As the techniques are described briefly here, we refer any reader requiring more information about the techniques to Paper I. The techniques are common between both cameras and clusters: any differences or cluster specific techniques are mentioned and any new techniques introduced in this analysis will be explicitly stated.

4.3.1 Field Identification and Subtraction

For all these clusters, as shown in Figs. 4.4 and 4.5, the main sequence is pronounced and it is these stars that we will use to construct the radial density profiles. The main sequences were fit with isochrones from the Dartmouth Stellar Evolution Database[4] (Dotter et al. 2008). The isochrones employed were NGC 1851: age = 10.5 Gyr, [Fe/H] = −1.18, [α/Fe] = +0.4; NGC 1261: age = 10.5 Gyr, [Fe/H] = −1.27, [α/Fe] = +0.4; NGC 5824: age = 10.2 Gyr, [Fe/H] = −1.91, [α/Fe] = +0.4. While the isochrone ages are slightly younger than the usually accepted ages of globular clusters, they provide the best description of the main sequences and main sequence turn-offs in the CMDs. Using the isochrones, we can

[4] `http://stellar.dartmouth.edu/~models/index.html`

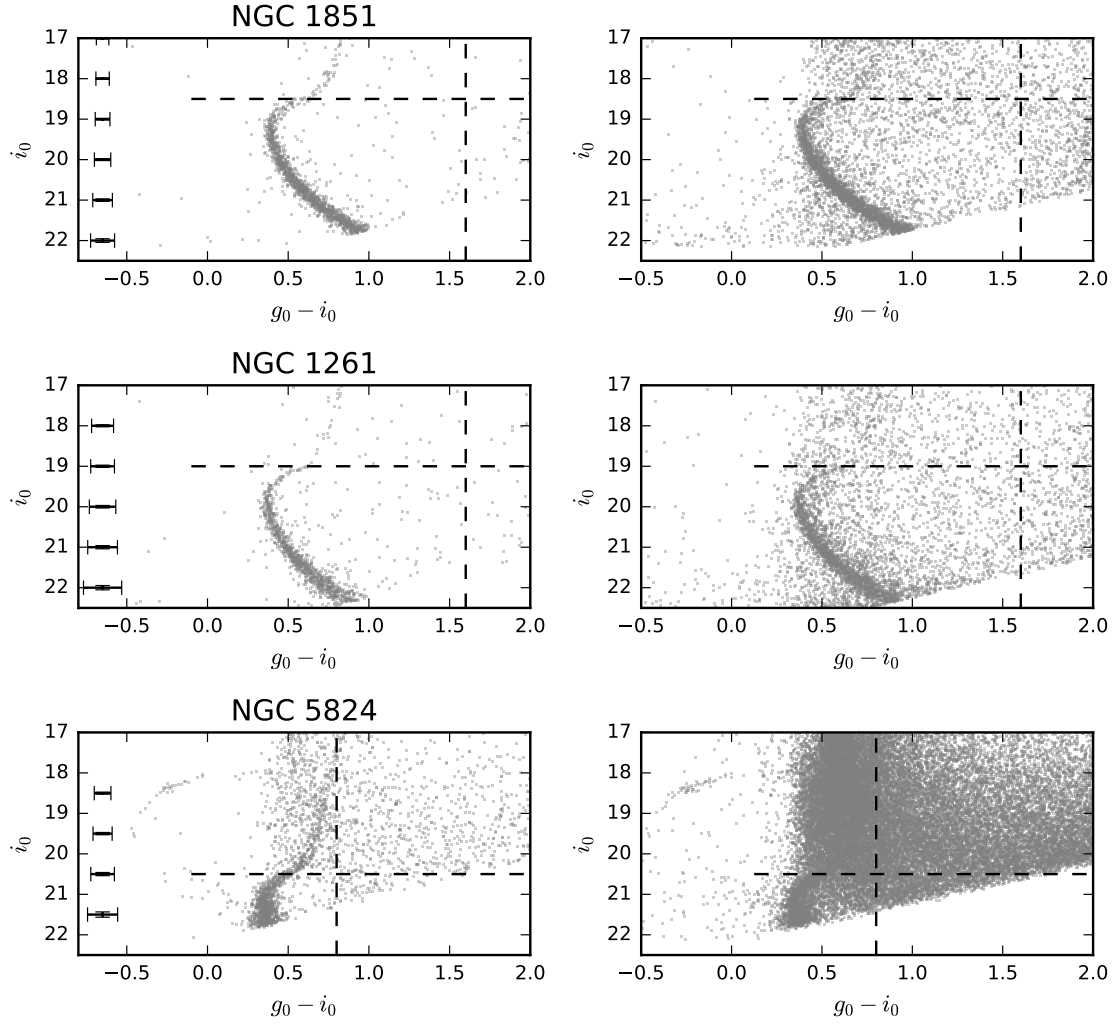

Figure 4.4: Colour-magnitude diagrams (CMD) of our clusters from our DECam images. Left col: All stars detected at distances from the cluster center $6' < r < 10'$ for NGC 1851, $5' < r < 10'$ for NGC 1261 and NGC 5824, are plotted to show the cluster main sequences. Right col: All stars at $6' < r < 40'$ for NGC 1851 and $5' < r < 40'$ for NGC 1261 and NGC 5824. The horizontal and vertical dashed lines indicate the photometric cuts undertaken in this paper.

Table 4.6: Fitted structural parameters from the LIMEPY surface brightness models.

Cluster	Model[1]	W	r_c	r_t	r_h	c
(1)	(2)	(3)	(4)	(5)	(6)	(7)
M2	K	7.05 ± 0.053	0.33 ± 0.003	11.64 ± 0.287	1.34 ± 0.020	1.54 ± 0.026
	W	6.18 ± 0.014	0.44 ± 0.003	33.04 ± 0.385	1.28 ± 0.005	1.88 ± 0.014
NGC1261	K	5.86 ± 0.090	0.35 ± 0.003	5.84 ± 0.309	0.89 ± 0.035	1.20 ± 0.054
	W	5.17 ± 0.173	0.42 ± 0.016	12.65 ± 1.019	0.88 ± 0.028	1.48 ± 0.089
NGC1851	K	7.99 ± 0.064	0.10 ± 0.002	6.40 ± 0.266	0.67 ± 0.028	1.83 ± 0.047
	W	7.21 ± 0.013	0.12 ± 0.003	41.54 ± 0.696	0.64 ± 0.008	2.55 ± 0.030
NGC5824	K	8.20 ± 0.124	0.08 ± 0.009	6.28 ± 0.693	0.66 ± 0.074	1.90 ± 0.158
	W	7.61 ± 0.011	0.08 ± 0.002	57.17 ± 0.694	0.61 ± 0.074	2.88 ± 0.158

(1) Cluster Name, (2) Type of model fit: K - King (1966), W - Wilson (1975), (3) Dimensionless central potential, (4) core radius in arcmin, (5) truncation radius in arcmin, (6) half-mass radius in arcmin, (7) central concentration, $c \equiv \log r_t/r_c$

begin removing unwanted foreground and background stars that contaminate our stellar catalogs. To do this, we used an isochrone-weighting scheme that is the same technique as presented in paper I. For each cluster, stars were assigned a weight value w with values between 0 and 1, that was based on their $g_0 - i_0$ colour difference with respect to the isochrone at the i_0 of the star. The weight is a Gaussian probability of the observed colour difference given the observational error in colour at the star's magnitude (Roderick et al. 2015). For example, a star on the isochrone has weight 1.0 and a $\pm 1\sigma$ colour error deviate has weight 0.61. For a pure cluster star population the distribution of weight values is strongly peaked towards higher values, while for a pure foreground population the distribution of w values is approximately uniform. The CMD diagrams for the clusters, coded by the w values are shown in Fig. 4.6.

For each cluster the distribution of w values was evaluated to establish the appropriate *separation weight* w_{sp} used to distinguish 'cluster stars' ($w \geq w_{sp}$) from 'field' stars ($w < w_{sp}$). A large w_{sp} value imposes a narrow window on the CMD about the fitted isochrone maximising the relative number of cluster stars but reducing the total sample. A small value of w_{sp} generates a larger sample but necessarily increases the number of field stars included. Given the different levels of field contamination, the distribution of the w values for each cluster are different, and, as a consequence, the adopted value of the separation weight for each cluster varied. We adopted the separation weight as the value that reproduced the appearance of the cluster main sequences shown, for example, in the left panels of Fig 4.4. The w_{sp} values adopted were 0.2 for NGC 1851, 0.3 and 0.15 for NGC 5824 (DECam and MegaCam, respectively), and 0.4 for NGC 1261. Admittedly the

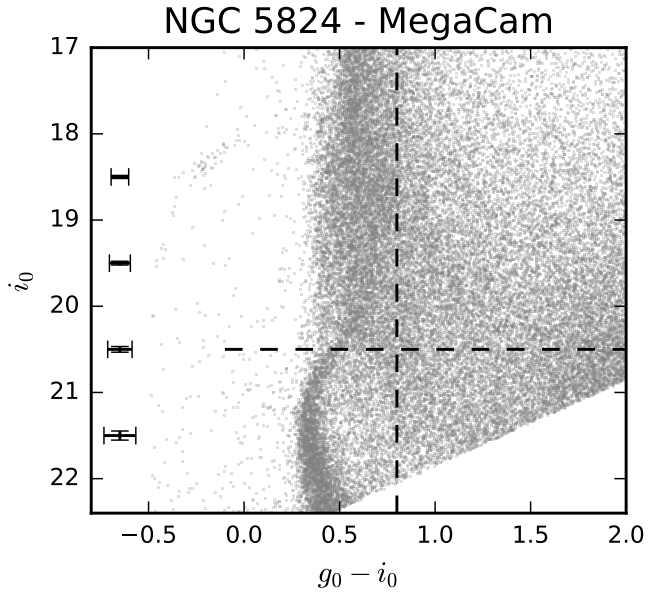

Figure 4.5: CMD of NGC 5824 from our MegaCam observations. Stars shown lie within 5 and 40 arcmin of the cluster center. Horizontal and vertical dashed lines indicate the photometric cuts as in Fig. 4.4.

choice of the w_{sp}values used is a judgement call, but trials conducted with varying the w_{sp}values used indicated that changes of order 0.05 do not alter the results. Substantially larger values reduce the sample sizes making it difficult to detect cluster stars at large radii, while substantially small values increase the field contamination which swamps the cluster-star signal at large radii.

We note, however, that not all the stars above the adopted separation weights are necessarily cluster member stars: field stars that happen to fall within the cluster-star window in the CMD will remain. We address this issue in the following analysis.

The successful removal of the field contamination is important for the validity of any extra tidal detections. To remove the field star contamination within our 'cluster-stars' sample, we first calculated azimuthally-averaged radial profiles from the 'cluster stars' sample using a gnomonic coordinate projection. The density profiles were computed using the same method as described in Paper I: densities were calculated for a series of concentric circular annuli of increasing radius from the cluster center. Any underlying contamination that is still present in our 'cluster stars' sample will be most pronounced at the largest distances from the cluster centre. In particular, the field star density level can be identified from the onset of a uniform density value in the radial density profile with increasing radii, which is clearly seen for all 4 clusters. The radius range in the density profiles used to

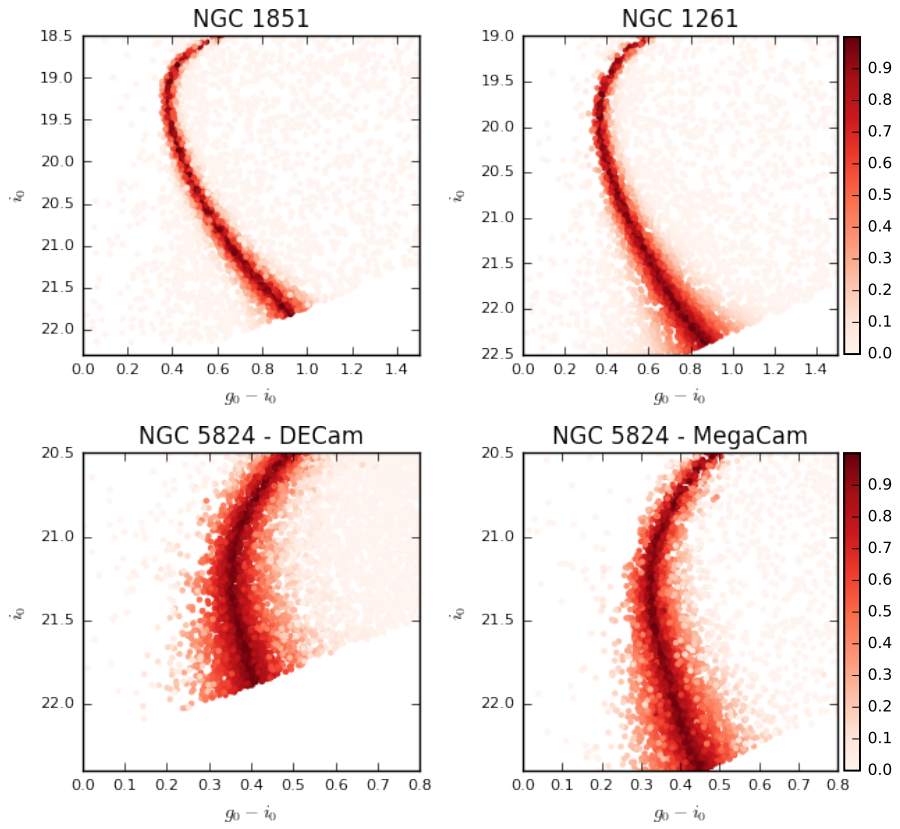

Figure 4.6: The isochrone-based weighting scheme for the globular clusters in this study for stars in the radial regions depicted in the right column of Fig. 4.4. Starting top right moving clockwise: NGC 1851, NGC 1261, NGC 5824 MegaCam and NGC 5824 DECam. The points have been colour-coded to show their given weight.

determine the field star density was set as from the point where the flattening begins to the outermost annulus that had 100% areal coverage within the field of view. The radial range used for each cluster was 60 – 100 arcmin for NGC 1851 and M2, 30 – 110 arcmin for NGC 5824 and 30 – 55 arcmin for NGC 1261. We then subtracted these field star densities from the total densities to generate the cluster radial density profiles.

4.3.2 Radial Density Profile

The resulting field-subtracted radial density profiles (along with the star counts of M2 from Paper I) are displayed in Fig. 4.7. Accompanying our star counts, we have incorporated the surface brightness data from Trager et al. (1995) that was scaled to our data in the regions they overlap. This allowed us to have coverage into the central regions of the clusters. We have then used the code LIMEPY, a *python*-based solver of distribution functions (Gieles & Zocchi 2015) to fit the surface density distributions. We fit King (1966) and

Wilson (1975) model profiles to our star counts through a least-squares method, and the parameters of the best-fit models are displayed in Table 4.6. While both the King and Wilson models will give similar descriptions of the central regions of the cluster, the Wilson model has a more extended profile than the King model. This is due to the addition of an extra linear term in the distribution function compared to the King model description. This generates a more extended profile for the same central potential (see McLaughlin & van der Marel 2005). Fig. 4.7 shows that the Wilson models describe the data better than the King models in the outer parts. Having said that, it is easily seen that for most of the observed profiles, the outer parts deviate from both models. We fit power laws to the profiles from the point of deviation from the models for NGC 1851 and NGC 1261. NGC 1851 sees a deviation from the Wilson model near 16.5 arcmin, and the profile declines at a rate of $\gamma = -1.5 \pm 0.2$ beyond this point. NGC 1261 declines at a sharper rate ($\gamma = -3.8 \pm 0.2$) beyond the apparent deviation from the Wilson model near 6.3 arcmin. These profiles suggest that there are cluster stars beyond the limiting radius of both the King and Wilson models, or stars that are "extra tidal". Both these clusters have been previously suggested to posses extra tidal stars (e.g., Carballo-Bello et al. 2012) and NGC 1851 is definitively known to possess an extended envelope (Olszewski et al. 2009), though the overall morphology of the envelope is unknown.

The NGC 5824 profile, however, is well fit by a large c-value Wilson model over most of the observed radial range. We also find that outside of the core radius (0.08 arcmin), the observed profile is well described by a power-law with index $\gamma = -2.2 \pm 0.02$ until a radius of ~ 5.5 arcmin where the observed profile (and the Wilson model fit) begin to curve downwards. Additionally, at the largest radii, there is tentative evidence for an upwards deviation from the model fit similar to what is seen in the other clusters. This deviation commences at about 25 arcmin and the density points beyond this radius are described by a power-law with index $\gamma = -1.3 \pm 0.5$. We caution, however, that this possible detection of a very extended envelope around NGC 5824 remains uncertain; a 1 sigma increase the adopted background is sufficient for it to cease to be detected.

4.3.3 Field Subtraction and 2D Density Distribution

The radial density profiles for all our clusters show a departure from what is predicted by the best-fit LIMEPY models. The 2-dimensional (2D) surface density distribution will be able to show exactly how the extra tidal stars are distributed and whether there are

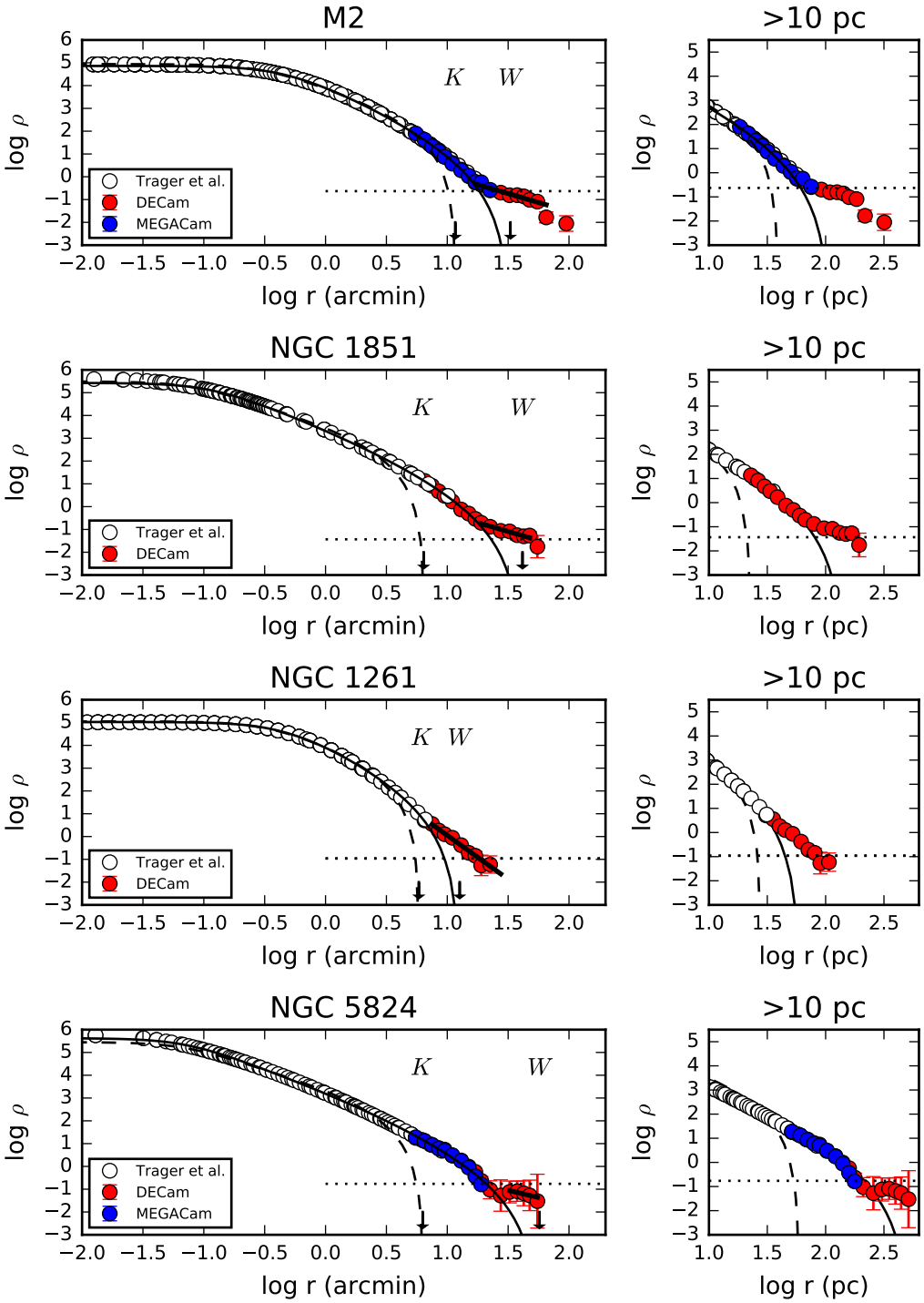

Figure 4.7: Radial density profiles for M2, NGC 1851, NGC 1261 and NGC 5824. The white points are surface photometry measurements from Trager et al. (1995), scaled to our star counts. The LIMEPY King (1966) and Wilson (1975) models are displayed by the dashed and solid lines respectively. Arrows pointing to the axis indicate the tidal radii of the King and Wilson models and are labelled with "K" and "W" respectively above the profiles. The horizontal dotted line shows our calculated background level. Star counts that deviate away from the Wilson (1975) models are fit with a power-law, indicated by the black bolded solid line. Left column: full profile as a function of radius in arcmin. Right: The outer regions (beyond 10 pc) of the profiles.

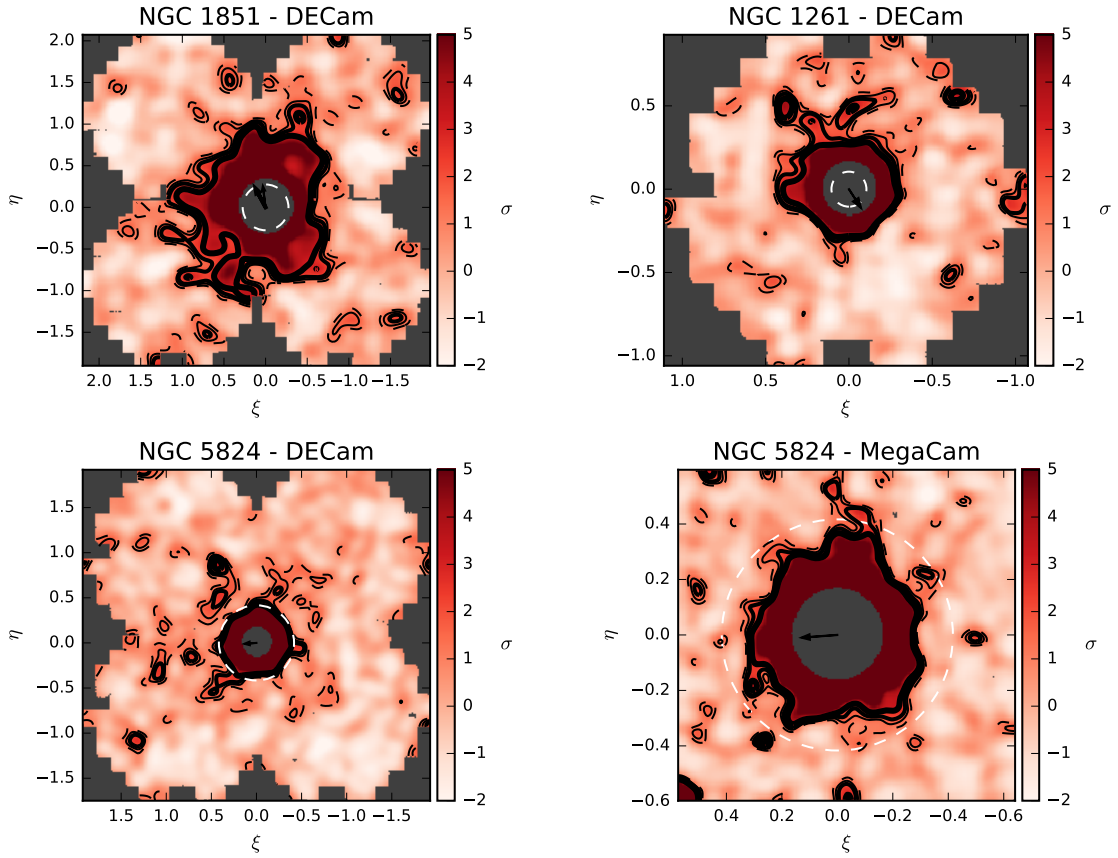

Figure 4.8: 2-D density distributions from our DECam and MegaCam observations. Top row: NGC 1851 and NGC 1261. Bottom row: NGC 5824 DECam and MegaCam observations. Colour scheme depicts different levels of the standard deviation of the mean background density, with contours indicating 1.5, 2 and 3σ and thicker contours implying higher significance. We have excluded in the inner regions of the clusters to enhance the clarity of the envelopes. Radius of areas excluded: 20′ (NGC 1851), 10′ (NGC 1261 and NGC 5824). Also plotted are arrows located at each clusters' centre indicating the direction to the Galactic center, and a bold arrow indicating proper-motion if it has been measured (e.g. Dinescu et al. 1999; Allen et al. 2006). The white ring indicates the radius of departure from the Wilson (1975) models for NGC 1851 and NGC 1261 (16.5 and 6.3 arcmin, respectively) and the 3σ detection radius for NGC 5824 (24.5′).

any streams, tails or envelopes in the fields of view. The techniques for finding the 2D field-subtracted distribution have been improved from Paper I, and are similar to the techniques used in Roderick et al. (2016). Specifically, we have updated how the 'field' contamination was identified and removed. We created smoothed distributions of both catalogs (smoothing parameters and bin widths for each cluster are presented in Table 4.7), in their respective gnomonic coordinates transformed from R.A. and DEC (J2000). In order to remove the inevitable field contamination in our 'cluster' distribution, we first created a flat-field out of the 'field' distribution, by scaling the mean 'field' bin density to one. The 'cluster' distribution was then divided by the flat field. The original 'field' distribution was normalized to the 'cluster' distribution by scaling the densities to the outer regions in the 'cluster' distribution, where there is no evidence of cluster populations. The normalized 'field' was subsequently subtracted from the 'cluster' distribution. This created our field-subtracted 2D density distribution of cluster stars. A bin was deemed as significant if its value (smoothed surface density of cluster stars) was more than three standard deviations (denoted as σ where σ represents one standard deviation) above the mean surface density value in the background subtracted 2D distribution. This process was completed for each cluster individually, per camera. To search for any cluster-related over-densities in the distributions, the cluster and its immediate periphery were masked as so they do not influence the statistics. This region was determined from their non background-subtracted radial profiles, and is presented in Table 4.7. The final 2D distributions for the three clusters are displayed in Fig. 4.8[5]. To help contrast the low surface brightness features in the 2D maps, we have excluded the most central regions of the clusters where the surface density values are many multiples of σ.

We will discuss the 2D distributions in the following section, but before we do, we explored the reality of a number of 2σ detections (hereafter over-densities) that do not appear to be spatially connected to the cluster envelopes. Such features were also seen in 2D distribution of M2 (see section 3.1.4 in Paper I). We explored the probability of these over-densities being either somehow connected to the cluster+envelope systems, or just fluctuations in the background distributions. As described in Paper I, we defined a parameter ζ that was determined by exploring the number of cluster stars in any given overdensity with respect to a series of random sampling of cluster stars from the complete stellar catalog through a series of Monte Carlo simulations as described in Paper I. The

[5] *The flat-fields used in this calculation are shown in 4.11, located in this chapter's addendum.*

Table 4.7: Parameters used to calculate the 2D density maps.

Cluster	Camera	Bin Width	Smoothing	Masked Region[a]
NGC 1851	DECam	1.2′ x 1.2′	6′	≤ 60′
NGC 1261	DECam	0.6′ x 0.6′	3′	≤ 20′
NGC 5824	DECam	0.6′ x 0.6′	4.8′	≤ 20′
	MegaCam	0.36′ x 0.36′	1.8′	≤ 20′

[a]Radius masked for mean bin value calculation.

simulations were conducted for each over-density beyond the central cluster+envelope detection for each cluster in the DECam imaging. No over-densities for any cluster detected beyond the cluster+envelope system appear to be significant (i.e. have $\zeta > 3$).

4.4 Analysis

4.4.1 M2

We presented the existence of a diffuse stellar envelope embedding M2 in Paper I. In Paper I, we calculated the characteristics of the envelope based on the deviation from the fit of a King (1962) model. As we have developed new techniques for analysing the radial density profiles, we decided to revisit the radial profile of M2 with the improved methods discussed in section 4.3.2. From the LIMEPY models, we found M2 deviates from both the King and Wilson profiles. Defining the stellar envelope as the deviation from the Wilson model, we find the star counts deviate from the Wilson model at approximately 17′, and decrease with a power law rate of $\gamma = -1.6 \pm 0.2$ beyond this point. In light of this new information, we recalculated the estimated mass ratio in the envelope by numerically integrating the observed radial density profile. The mass ratio was determined as the ratio between the integral of the profile from the point of deviation from the Wilson model to the extent of the profile (which we have defined as the envelope) with respect to the combined integral of the Wilson model (which defines the cluster) and the envelope (see Paper I). Under the new models, we integrated the profile between 17′-70′ and found the envelope contains $1.06 \pm 0.04\%$ of the combined mass of M2 and its envelope, where the uncertainty is estimated by varying the outer regions of the radial profile by one standard deviation.

4.4.2 NGC 1851

In the upper left panel of Fig. 4.8 the envelope of NGC 1851 is clearly visible, well beyond the excluded inner 20′. We see no distinct tail-like feature similar to those seen in Palomar 5 (see Odenkirchen et al. 2003) or NGC 5466 (Belokurov et al. 2006a; Grillmair & Johnson 2006), nor is there an obvious large stream nearby; the structure we see is centered on NGC 1851 and does not extend across the entire field of view. The envelope we find extends out to a radius of 67.5 arcmin at the 3σ detection level, which at a distance of 12.1 kpc from the Sun corresponds to $\sim$ 240 pc. This value is in good agreement with the extent of the radial profile and comparable to the $\sim$ 250 pc given in Olszewski et al. (2009). We have also presented the CMD for the region beyond the nominal Wilson tidal radius in the upper left panel of Fig. 4.9 and the main sequence is clearly evident.

With the aid of the astroML python module[6], we fit a bivariate Gaussian to the envelopes to uncover any possible orientation or elongation. Using "cluster stars" between the radial distance of the deviation from the Wilson model to the limit of the 3σ detection (16.5′ - 67.5′), we find an ellipticity $e = 0.17 \pm 0.04$ with a preferred orientation of $\theta = 176^\circ \pm 19^\circ$, though this position angle is poorly constrained. The moderate ellipticity of the envelope agrees with the central regions of the cluster ($< 16.5'$), $e = 0.11 \pm 0.01$, though the position angle of the cluster ($\theta = 70^\circ \pm 2^\circ$) does not match with the envelope.

The star counts of NGC 1851 (Fig. 4.7, top left) revealed a clear deviation from the King and Wilson models. Of these two models, the Wilson model better describes the star counts, but in either case, there are stars beyond the model profiles, decreasing a rate described by a power law of index $\gamma = -1.5 \pm 0.2$. Olszewski et al. (2009) found a similar relation with a best-fit power law index of $\gamma = -1.24 \pm 0.66$ in agreement with our result. Taking the envelope to extend from 16.5' to 67.5', we find that it contains $0.92 \pm 0.08\%$ of the total mass of the cluster+envelope system. This is more than the 0.1% reported in Olszewski et al. (2009), though it is similar to the ratio of M2's envelope, $\sim 1.1\%$. Based on the Wilson model, NGC 1851 is highly concentrated, $c = 2.55 \pm 0.03$. This is amongst the highest concentrations for Galactic globular clusters (see the Wilson models presented in (McLaughlin & van der Marel 2005)).

4.4.3 NGC 5824

Grillmair et al. (1995) searched for tidal tails in a large sample of Globular Clusters using

[6] http://www.astroml.org/

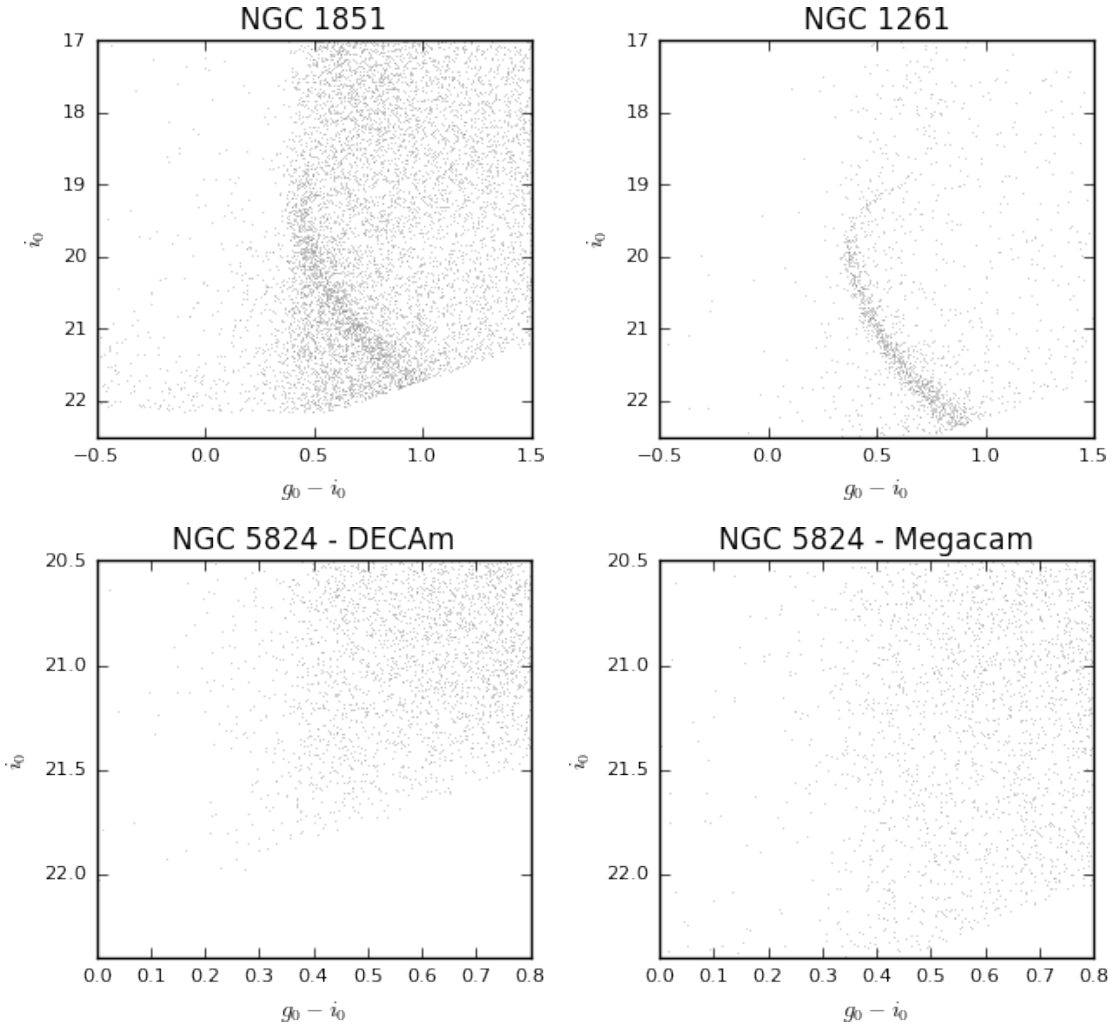

Figure 4.9: Top row: CMD of the stellar envelopes ranging from the radius of deviation from the LIMEPY models to the extent of the 3σ detection belonging to: NGC 1851 (left, stars of radius $16.5' < r < 67.5'$) and NGC 1261 (right, stars of radius $6.3' < r < 22'$). Both CMDs show clear signs of the clusters' main sequence. Bottom row: CMD of the region surrounding NGC 5824 between the radius of deviation from the LIMEPY models to the outermost radial bin that had a measured density value that is non-zero: $25' < r < 50'$. No obvious main sequence is seen.

photographic plates. Amongst those, NGC 5824 was one of the clusters whose radial profile suggested the presence of stars beyond the King tidal radius. We find that the over the radius 1.5 to 45 arcmin (see Fig. 6 in Grillmair et al. 1995) the profile follows a power law of index $\gamma = -2.2 \pm 0.1$. This is consistent with our findings if we fit a power law over our radial density profile, $\gamma = -2.20 \pm 0.02$. When compared to the data of Grillmair et al. (1995) our star counts are consistent with theirs but begin to differ for radii beyond 15 arcmin. Specifically, as seen in Fig. 4.7, we see a drop away from the -2.2 power law slope beyond 13 arcmin that is not present in the Grillmair et al. (1995) data. Given our superior photometric precision and our explicit allowance for the significant variable reddening, we believe our data are more reliable than those of Grillmair et al. (1995) in these outermost regions.

We find the stars counts are reasonably well described by a Wilson model. The limiting radius from the Wilson model is $\sim$ 530 pc for NGC 5824, with only a small group of clusters having a similar radius or larger (e.g., NGC 5634: $\sim$ 537 pc, NGC 6356: $\sim$ 589 pc, NGC 6139: $\sim$ 676 pc, See McLaughlin & van der Marel 2005). Furthermore, NGC 5824 is found to be remarkably concentrated, $c = 2.86 \pm 0.16$, in very good agreement with the Wilson model fit in McLaughlin & van der Marel (2005), $c = 2.87 \pm 0.08$. In fact, NGC 5824 is amongst the most concentrated clusters in the Milky Way. Similarly massive clusters like NGC 5824 with a comparable concentration include NGC 5634 ($c = 2.79 \pm 0.08$) and NGC 6139 ($c = 2.95 \pm 0.08$) (McLaughlin & van der Marel 2005). However, we note that the data sets featured in McLaughlin & van der Marel (2005) do not cover a similar radial extent as our profiles. As a result, their values for limiting cluster radii and concentration indices may not be as accurate when compared to our profiles.

Both the 2D distributions from the MegaCam and DECam imaging of NGC 5824 show that the cluster does not obviously have an extended envelope, based on the interpretation of the fitted Wilson model. We find the cluster is detectable (3σ detection) to a radius in the DECam imaging of 24.5′ (~230 pc). The cluster, between 5′ and 24.5′, has a low ellipticity, 0.18 ± 0.01, and position angle of $87° \pm 2°$. We note that in Fig. 8 there are a number of moderate significance (2.0 - 3.0 σ) detections at large radii in the DECAM imaging. These may be signs of extended structure beyond our detection limit.

Despite the differences in scales and adopted smoothing, and the differences in the outer radial profile, we find the 2D distribution DECam observations (Fig. 4.8) to be in broad agreement with the 2D distribution shown in Fig. 13 of Grillmair et al. (1995).

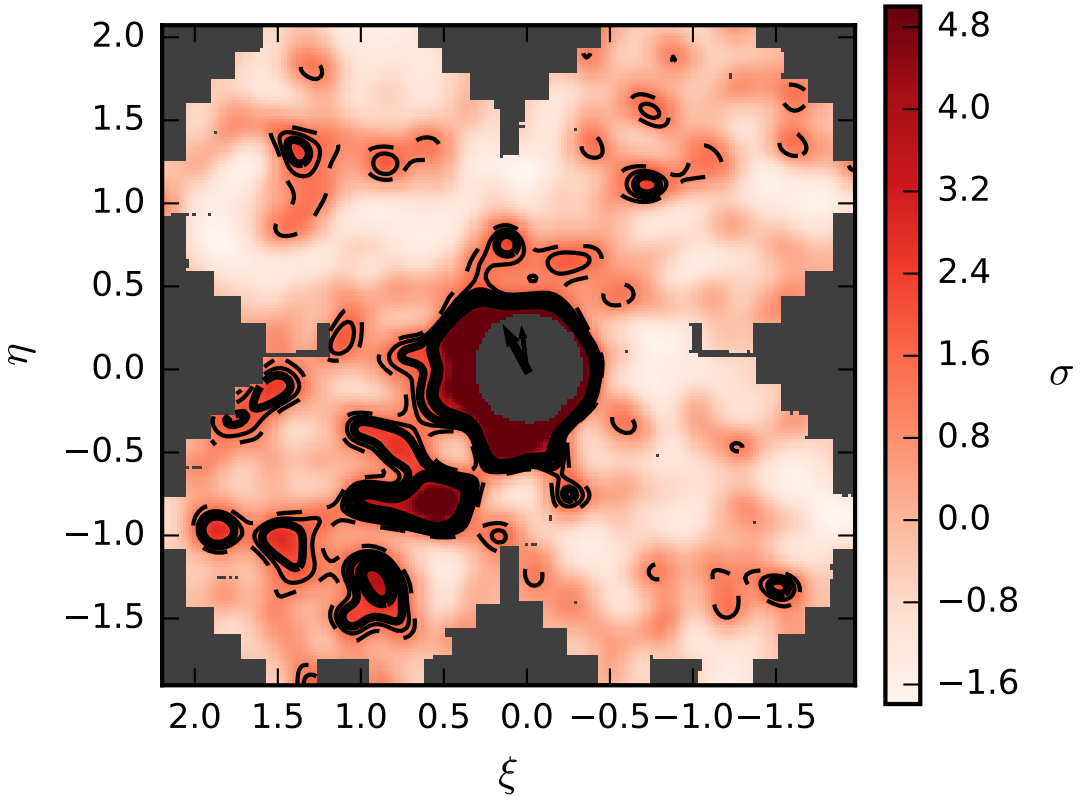

Figure 4.10: 2D density distribution of NGC 1851 when the detection limit is restricted to 1.5 mag below the main sequence turn off. There is some structure beyond the envelope in this image that has no match in Fig. 4.8, but none of these over densities were determined to be a real feature ($\zeta > 3$) in the 2D map.

Specifically, we have recovered a similar looking features in the North West to North East, although we do not have detections to the South of the cluster. There are no signs of any large stream-like structure in the field of view, or any detection of tidal tails.

We further find that beyond $\sim 25'$, where the observed profile breaks away from the Wilson model fit, the star counts follow a power-law of index $\gamma = -1.3 \pm 0.5$ to a distance of $\sim 50'$ (470 pc). While still within the Wilson limiting radius, the power law index is similar to both NGC 1851 and M2. These star counts are within 1σ error of the background uncertainty, and given the uncertainty on the power law index, it is ambiguous whether these star counts are describing a real feature of NGC 5824. The lower row of Fig. 4.9 shows the CMD all stars between radial region that follows the shallow power law description ($25' < r < 50'$), and there is no apparent evidence for the main sequence of NGC 5824. We decided to perform a check to see how the envelope of NGC 1851 appears if we restrict the photometric depth of our NGC 1851 data to match that of NGC 5824 (1.5 mag below

the MSTO). Fig. 4.10 shows that the majority of the envelope disappears, leaving behind a considerably smaller envelope. There are some over densities present in this figure that are not in Fig. 4.8, but none of which have a ζ value greater than three. Based on this comparison it is conceivable that NGC 5824 could harbour a large diffuse envelope that would be revealed if substantially deeper data were available.

We can estimate the mass ratio in the tentative outer stellar structure by employing the same techniques we have used for NGC 1851 and M2. Beyond the point of deviation of the Wilson model ($\sim 25'$, ~ 235 pc), we find the mass ratio to be $0.82 \pm 0.05\%$, similar to the mass ratio of NGC 1851's envelope. Considering the similarities between the possible extended stellar structure with what has been calculated from NGC 1851, deeper photometry may uncover a substantial number of extra-tidal stars belonging to NGC 5824.

4.4.4 NGC 1261

DECam imaging of NGC 1261 reveals the existence of a small, but detectable, envelope. As for NGC 1851 and NGC 5824, we see no evidence for any 2-arm axisymmetry, with the envelope detectable out to $22'$ (~ 105 pc). The debris appears symmetric with an ellipticity of $e = 0.04 \pm 0.01$ and an associated position angle of $\theta = 79° \pm 9°$ East of North between $6.3'$-$22'$, the apparent radial extent of the envelope. The envelope is less massive than previous envelopes this study has uncovered; the low-surface brightness feature contains $0.42 \pm 0.03\%$ of the total mass of the NGC 1261 system. Further, the upper left panel of Fig. 4.9 clearly displays that the stellar population of NGC 1261 is detected beyond the nominal Wilson tidal radius.

Compared to the other clusters in this study, the star counts for NGC 1261 drop off at a steeper rate with $\gamma = -3.8 \pm 0.2$ instead of $-2 < \gamma < -1$. Moreover, the power law outer profile fit for NGC 1261 found by Carballo-Bello et al. (2012), $\gamma = -3.68^{+0.07}_{-0.17}$ is consistent with our findings. The envelope is detectable out to a less than half the distance of the envelopes surrounding M2 and NGC 1851 (see also right column of Fig. 4.7) and the extent of NGC 5824 itself. Combining this difference in power law slope with the fact that the NGC 1261 envelope contains notably less mass, this then suggests that the NGC 1261 envelope may have an origin that is different from that for the other envelopes uncovered in this study.

4.5 Discussion

4.5.1 Origin of the envelopes

This study has presented evidence for the existence of diffuse extended stellar envelopes surrounding four massive Galactic globular clusters. The envelopes extend beyond the King and, in most cases, Wilson model fit limiting radii. M2 and NGC 1851 show a well-defined break from the best fit Wilson model, which is already substantially more extended than the best fit King model. Beyond the Wilson model, there is a power law distribution of $\gamma = -1.6 \pm 0.2$ for M2 and $\gamma = -1.5 \pm 0.2$ for NGC 1851. The envelopes extend to at least 240 pc in radius in both cases and contain approximately 1.1% and 0.9% of the system mass. NGC 5824 is well fit by a very extended Wilson model ($r_t = 533 \pm 7$pc). We note that, despite no definitive detection of a diffuse stellar envelope, the apparent size of NGC 5824 is larger than that for the M2 and NGC 1851 envelopes. NGC 1261 is like M2 and NGC 1851 in that there is a well defined break from the best fit model, but the envelope is detected to much smaller radii ($\sim$ 105 pc), the power-law slope is substantially steeper ($\gamma = -3.8 \pm 0.2$) and the fractional mass in the envelope is less (0.4%). A summary of these results are in Table 4.8.

It is natural to ponder how these envelopes came to be; whether they are born out of the dynamical evolution of globular clusters in the Milky Way, or are perhaps linked to the remains of dwarf galaxies that the Milky Way accreted some time ago. We proposed in Paper I that based on: (a) orbital information, (b) the distribution and shape of the detected extended envelope, (c) the presence of internal Fe abundance variations, and (d) the existence of peculiar stellar populations in the cluster CMD, the M2 cluster+envelope system may have its origins in a long since accreted dwarf galaxy, rather than being a natural product of the dynamical evolution of globular clusters. We will now explore these two scenarios with respect to NGC 1851, NGC 5824 and NGC 1261.

Even though they spend a majority of their lifetimes away from the disk, Galactic halo globular clusters can still suffer from disruption due to tidal effects from the Milky Way. These interactions can add enough energy to the cluster for stars to escape the cluster. Modelling of this process shows that the escaped stars form long streams extending out from the cluster itself, one leading and the other trailing the cluster; otherwise known as tidal tails (Lee et al. 2006; Küpper et al. 2010b). All four clusters do not show the long, thin tidal tail structures which are seen around a small number of other clusters (e.g., Palomar 5; Odenkirchen et al. 2001; Grillmair & Dionatos 2006, NGC 5466; Belokurov

et al. 2006a).

When a cluster passes through the disk of the Milky Way, it experiences a significant change in the gravitational potential on a short timescale. This inflicts a sudden addition of energy on the globular cluster, known as a shock (e.g., Gnedin et al. 1999; Binney & Tremaine 2008). The loosely bound stars in the outermost regions of the cluster are much more affected by the shock than the tightly bound stars in the core. As a result, shocks contribute towards the disruption process: increasing the number of stars that can potentially escape the cluster. However, after a cluster experiences a shock, Küpper et al. (2010b) shows that excited stars do not leave the cluster immediately. Instead, the excited stars start to populate the outer regions of the cluster within the Jacobi radii. It may take many dynamical times for the stars to escape from the cluster, leaving through the Lagrange points to create the characteristic tails. In their studies, Küpper et al. (2010b) find the Jacobi radius of the non-core collapse clusters can be comparable to the observed tidal radius, with the ratio between to ranging from 0.8 to 1.2. Beyond this radius, Küpper et al. (2010b) state that the surface density profiles can decrease at rate that follows a power-law like relationship with slope $\gamma \approx -4$, potentially as sharp as -5[7]. This power-law can become noticeably flatter when the modelled cluster approaches apogalacticon; at this point in the clusters orbit, the power-law indices can be shallow as $\gamma \approx -1$. Other studies present similar results: the models of disrupted globular clusters performed in Lee et al. (2006) show that, beginning with a cluster that follows a King profile, the evolution of the cluster can develop a power-law profile with an average index of -3.2. The models, therefore, show that envelopes are possible from dynamical evolution, but they generally have steep power laws and are not very extended. These are the characteristics we will use to interpret our results.

NGC 1851

NGC 1851 has been known to be embedded in a envelope since the photometric findings of Olszewski et al. (2009). Carballo-Bello et al. (2014) also found evidence for extended structure surrounding NGC 1851. However, it was unclear from those studies what the morphology of the envelope was, and whether it extended into, or was part of, a larger stellar stream. Our results are shown in the upper left panel of Fig. 4.8. The envelope is clearly visible, extending well beyond the excluded $20'$. We see that NGC 1851, perhaps

[7] *As mentioned in Chapter 3, the observed power-law profile may be a product of the viewing angle of the cluster. This must be considered when comparing our profiles to the results of Küpper et al. (2010b).*

Table 4.8: Details of the clusters and their envelopes.

Cluster	Limiting Radius (pc)[a]	3σ Size Detection (pc)[b]	Power Law Index (γ)	Mass Ratio
M2	111 ± 1	~ 210	-1.6 ± 0.2	$1.06 \pm 0.05\%$
NGC 1261	60 ± 5	~ 105	-3.8 ± 0.2	$0.42 \pm 0.03\%$
NGC 1851	146 ± 2	~ 240	-1.5 ± 0.2	$0.92 \pm 0.08\%$
NGC 5824[c]	533 ± 7	~ 230	(-1.3 ± 0.5)	$(0.82 \pm 0.05\%)$

[a] Limiting radius from the Wilson Model.
[b] Size of the 3 σ detection from the 2D distribution.
[c] Bracketed values are properties of the tentative envelope estimated by the radial density profile.

because it is not near apogalacticon (e.g., Dinescu et al. 1999; Allen et al. 2006), does not have a power law outer density profile consistent with the predictions of the Küpper et al. (2010b) models. Orbital estimates for NGC 1851 suggest that the cluster has made ~ 40 disk passages over a Hubble time, taking 580 - 685 megayears to complete an orbit of our Galaxy (Dinescu et al. 1999; Allen et al. 2006). The evaporation rates calculated in Gnedin & Ostriker (1997) show that destruction through evaporation is on a similar time scale to destruction through bulge and disc shocks, implying that NGC 1851 is not greatly susceptible to shocks (see also Dinescu et al. 1999; Allen et al. 2006).

NGC 1851 has been suggested before as being the remnant of a dwarf galaxy. After the discovery of the envelope by Olszewski et al. (2009), Bekki & Yong (2012) modelled the cluster+envelope system to explore the formation of the system from the accretion of nucleated dwarf galaxy. Some of our results agree with what was presented in those models. The projected radial density in Fig. 5 of Bekki & Yong (2012), shows the debris follows a power law slope of ~ -2 within a radial distances of ≤ 80 pc, becoming steeper beyond 80 pc as ~ -2.5. Our observed profile ($\gamma = -1.5 \pm 0.2$) is flatter than the models, but, within uncertainties, is consistent with Bekki & Yong (2012) findings. The peculiar stellar populations that NGC 1851 contains also supports an origin in a dwarf galaxy. As discussed in the Introduction, the properties of the stellar populations of NGC 1851 have a lot in common with those of ω Cen, M54 and M2, all clusters for which an origin in an accreted dwarf galaxy has been postulated. Interestingly, Marino et al. (2014) found that stars in the envelope show the same Fe-spread and similar heavy element abundances as one of the two sub-giant branch populations. Collectively, the previous discussion makes a strong argument for the envelope belonging to NGC 1851 to be the last vestiges of a dwarf galaxy.

NGC 5824

The orbit of NGC 5824 is not known. The evaporation rates of NGC 5824 are similar to that of NGC 1851, the cluster is not susceptible to disk and bulge shocks (Gnedin & Ostriker 1997). Unlike NGC 1851, NGC 5824 is located at a greater galactocentric distance. At a distance of 25.9 kpc, NGC 5824 has the largest galactocentric distance amongst the clusters presented in this study (M2: 10.4 kpc, NGC 1851: 16.6 kpc, NGC 1261: 18.1 kpc; Harris (1996b) 2010 edition). Therefore it is possible that NGC 5824 could hold onto a diffuse stellar envelope if the orbit does not take it relatively close to the Galactic center. While we do not find definitive evidence for stellar envelope, NGC 5824 is still very extended. We found NGC 5824 detected out to a radius of approximately 230 pc. As well as being similar in size to the envelopes belonging to M2 and NGC 1851, it is also comparable to the half-light radii of Local Group dwarf galaxies (see McConnachie et al. 2009). Furthermore, the Wilson model fit to NGC 5824 gives a truncation radius much larger than most, if not all, Milky Way Globular Clusters (see McLaughlin & van der Marel 2005). The concentration parameters calculated in both the King and Wilson models (see Table 4.6) present more similarities between NGC 5824 and NGC 1851.

Further, NGC 5824 also has common properties with other anomalous globular clusters such as ω Cen and M54. It is amongst the brightest clusters in the Galactic halo (M_v = −8.83 mag), and is second only to M54 at galactocentric distances beyond $\sim$ 20 kpc. NGC 5824 was reported in Da Costa et al. (2014) as having an internal Fe abundance variation, although Roederer et al. (2016) was unable to confirm the variations, however the authors did find a star with notably different s-process abundances amongst their sample. Our observations do not provide concrete evidence for the existence of a diffuse stellar envelope surrounding NGC 5824. However, we have determined that NGC 5824 itself has a limiting radius of approximately 500pc according to Wilson model fit, much larger than the envelopes of M2 and NGC 1851. This fact and the above discussion does present encouraging results that warrant deeper photometric observations of NGC 5824 and its periphery.

NGC 1261

The final cluster presented in this paper, NGC 1261, does not appear to be similar to the others. It is not as massive as the others studied: it is approximately 60% less massive than NGC 1851 for the same mass-to-light ratio, even more so when compared to the other

clusters in this study. The stellar populations of NGC 1261 have not been extensively studied as for the other clusters, though Milone et al. (2017) do detect evidence for a possible Fe-variation in their chromosome maps. The radial profile uncovered an envelope, though it is different to the other envelopes we have discovered. It contains relatively less mass in the envelope ($\sim$ 0.4 % compared to the 1.1% and 0.9% for M2 and NGC 1851) and the radial profile follows a much sharper power law, $\gamma = -3.8 \pm 0.2$, which is in good agreement with the profile fit by Carballo-Bello et al. (2012). The radial profile is also consistent with the globular cluster disruption models of Lee et al. (2006) and Küpper et al. (2010b).

NGC 1261 does not have a known orbit. However, Webb et al. (2014) placed constraints on the orbit through the Galactocentric distance and the slope of the mass function of NGC 1261. The authors report that NGC 1261 is likely near apogalacticon, with a highly eccentricity ($e > 0.7$) orbit. If NGC 1261 is near apogalacticon, the debris still is compatible with Küpper et al. (2010b) simulations. *The authors show that at apogalacticon, the density profile power-law index of a disrupted cluster can be still be in the range of -4 to -5 within 50 pc (comparable to the limits of our detected envelope). It will then flatten to the shallower power-law of index -1 at approximately 100 pc, much further beyond our field of view.* Interestingly, the destruction rate of NGC 1261 appears to not be sensitive to shocks as well, with the evaporation rate remaining constant across the Gnedin & Ostriker (1997) models. However, the relatively low concentration value compared to NGC 1851, NGC 5824 and M2 (across both King and Wilson models) may suggest it is more susceptible to dynamical effects. We suggest that NGC 1261 and its envelope are unlike NGC 1851 and M2: its envelope appears consistent with an origin in the dynamical evolution of the cluster.

Connections to Dwarf Galaxies

Combining semi-analytic modelling of galaxy formation and the Millennium II simulation, Pfeffer et al. (2014) explored the contributions of dwarf galaxy nuclei to GC populations in galaxies. In their study the authors described a nucleated dwarf galaxy as a GC that possesses an internal heavy element abundance spread and/or a variance in age (Pfeffer et al. 2014). In Paper I, we suggested that the GC M2 met this criterion and noted that the existence of an extended stellar envelope around the cluster could be added as further evidence favouring this interpretation. The similarities between M2 and NGC

1851, particularly as regards the existence of extended stellar envelopes, and potentially NGC 5824 suggest that this interpretation could be applied to these clusters as well. However, radial profiles like that of NGC 1261 are not uncommon: the survey completed by Carballo-Bello et al. (2014) shows that in their sample many GCs have outer profiles that can be described by power laws similar to what we found for NGC 1261. There is therefore no reason to postulate that the envelope surrounding NGC 1261 is in any way related to the remnant of an accreted dwarf galaxy.

4.6 Conclusion

We have presented the results of wide-field imaging, using the mosaic cameras MegaCam and DECam, of the outer halo globular clusters, NGC 1261, NGC 1851 and NGC 5824. Identifying clusters stars though the observed colour-magnitude diagram, we have determined that all three clusters have extra tidal stars, lying beyond the predicted limiting radius of surface brightness profiles models. NGC 1851 is found to possess an envelope ~ 240 pc in size that contains $\sim 0.9\%$ of the system mass and is described by a power law of index $\gamma = -1.5 \pm 0.2$. NGC 1261 is also found to be embedded in a stellar envelope, ~ 105 pc in size and contains $\sim 0.4\%$ of the total mass of the system. The density profile of the envelope is fit with a power law of index $\gamma = -3.8 \pm 0.2$. NGC 5824 does not have a detectable envelope, though it is found to extend out to a distance of ~ 230 pc, which is comparable to the envelopes found around NGC 1851 and M2 from our previous study.

Some fundamental properties, such as the kinematics and element abundances, of these stellar envelopes are still unknown. With respect to disrupting globular clusters, it is unclear whether the process of heating/evaporation (either through two-body relaxation or tidal/disk shocks) can create an envelope of the size of those we see for NGC 1851 and M2. The envelopes of NGC 1851 and M2, and the overall size of NGC 5824 are all similar in size to local dwarf galaxies, and the clusters themselves have properties similar to those of M54 and ω Cen. We follow, then, to the same conclusion that these clusters could be the nucleated cores of former dwarf galaxies. The envelope surrounding NGC 1261 is consistent with those seen in dynamical models (e.g., Lee et al. 2006; Küpper et al. 2010b), favouring dynamical evolution as the likely origin.

Our results so far suggest that faint envelopes are a common feature in outer halo globular clusters. However, it is important to distinguish the differences between the envelopes we have found. While we find massive, low surface brightness envelopes surrounding al-

ready anomalous clusters, the envelope embedding NGC 1261 is different, in both relative size and luminosity. It is of interest to see if this feature is common around other more 'classic' globular clusters, and whether the frequency of the envelopes are comparable to the amount of clusters with tidal tails; or indeed whether the envelopes are somehow related to the formation of tidal tails. It is obvious that more data is needed before we can start to draw connections between these two seemingly different kinds of outer envelope structure in globular clusters. Targeting clusters of similar magnitude and size such as M3, NGC 2808 or NGC 7078 and deeper imaging of NGC 5824 would be beneficial towards understanding the frequency of large stellar envelopes in massive Milky Way globular clusters and their connections to the build up of the Milky Way and its Halo.

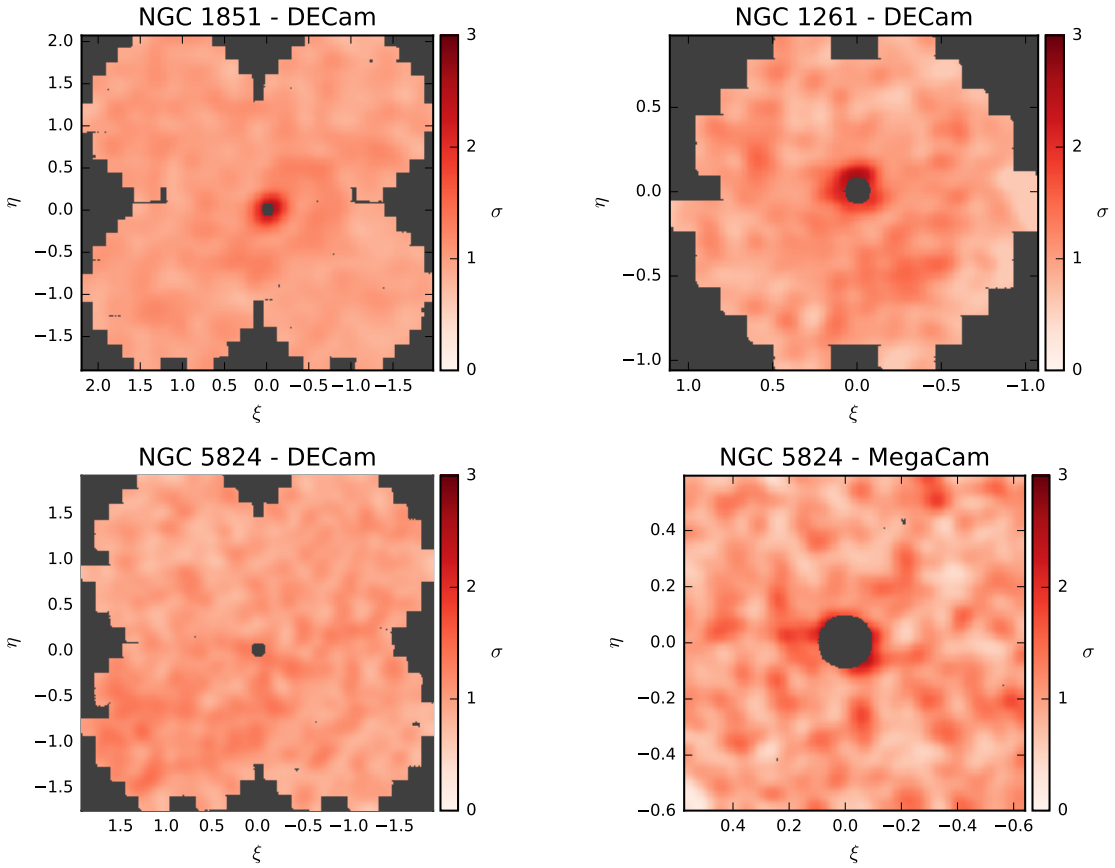

Figure 4.11: The flat fields from our DECam and MegaCam observations. Top row: NGC 1851 and NGC 1261. Bottom row: NGC 5824 DECam and MegaCam observations. Colour scheme depicts the density fluctuations about the mean value of one. We have excluded in the inner regions of the clusters for consistency with Fog. 4.8.

4.7 Addendum

Please visit the works listed below for more information on the following topics:

- Globular clusters associated with the Sagittarius dwarf galaxy: Bellazzini et al. (2003).
- C+N+O abundance variations in NGC 1851: Villanova et al. (2010) and Gratton et al. (2012b).
- Possible merger origin of NGC 1851: Carretta et al. (2010c).

Chapter 5

Conclusions

Galactic globular clusters may appear as gravitationally-robust structures with many thousands of stars held within their tidal boundaries, but it is clear that they can be dissolved and disrupted by both internal processes and the external tidal forces their host galaxy imposes on them. Once a cluster begins to experience substantial mass loss, the long thin tidal tails that can form are remarkably powerful probes for understanding not only the evolution of globular clusters, but also the properties and characteristics of the tidal field in which they have evolved (e.g., Bonaca et al. 2014; Pearson et al. 2015). However, it is becoming increasingly clear that tidal tails are not the only extended stellar structures that are found around Galactic globular clusters. This thesis has explored the different kinds of extended structures surrounding globular clusters, building on the knowledge of the important tidal stream of Palomar 5, while also uncovering previously unknown stellar structures surrounding some of the most massive globular clusters in the Galactic halo. The key points arising from this dissertation are as follows:

Palomar 5 has been known for the past decade to be near complete destruction (Dehnen et al. 2004). The outer tail structure is immense, though previous kinematic studies have only covered the parts of the tails closest to the cluster itself (Odenkirchen et al. 2009). While the tails have proved helpful in placing constraints on the cluster's orbit, there is much more of the tidal debris to explore. We presented kinematic measurements for 47 newly identified red giants, as well as recovering 20 already confirmed giants, along 23° of the tails, more than doubling the previous coverage presented in Odenkirchen et al. (2009). These results have already been utilised in studies of the tails, such as estimates of the Galactic potential (e.g., Bovy et al. 2016) and simulating the substructure seen within the tails (e.g., Erkal et al. 2016).

Wide field imaging of the clusters presented in this work found evidence for the existence of extra-tidal stellar populations. NGC 1261, NGC 1851 and M2 were all found to be embedded in low mass, diffuse stellar envelopes. The envelopes of NGC 1851 and M2

have characteristics that are similar to each other: a similar size, similar radial profiles exhibiting shallow power-law declines ($\gamma \approx -1.5$) and similar relative mass in the envelopes. NGC 1261 and its envelope appear different: smaller in both size and relative mass in the envelope, as well as exhibiting a steeper power-law decline ($\gamma \approx -3.8$) in the radial density profile of the extra-tidal population. An envelope is also tentatively detected in NGC 5824, but the cluster itself is found to extend to a similar distance as the cluster+envelope systems of NGC 1851 and M2. If the signs of an envelope in the radial profile represent a real feature in NGC 5824, then we find it to have a similar power-law decline to NGC 1851 and M2.

There appears to be two different kinds of extra-tidal structures in globular clusters: tidal tails and diffuse stellar envelopes. Further, we have found evidence for the potential existence of two distinct types of stellar envelopes. Intriguingly, the more massive, flatter envelopes belong to the more massive clusters that have peculiar stellar properties (i.e., Fe-spread). It is worth exploring whether the possible bimodality of the envelope structure is real or just a product of the small sample of clusters we have presented so far. It is clear we need to explore more clusters to build a stronger sample to search for any relationship between the types of envelopes that may exist. Such relationships could be between cluster properties (i.e., element abundances) and the type/shape of any tidal debris or between the power-law description and cluster mass. In any case, the sample size needs to be increased before we can be confident of the properties of envelopes and how they relate to characteristics of their associated clusters in the Milky Way.

Models of disrupting globular clusters demonstrate the eventual formation of tidal tails as an end result (e.g., Küpper et al. 2010b). However, the faint stellar envelopes discovered surrounding NGC 1261, NGC 1851, M2 and NGC 5824 (though tentative at the moment for the latter cluster) do not appear to show any kind of elongation or axisymmetry that would be indicative of tidal tails. Furthermore, the faint stellar envelope embedding NGC 1261 is different from those for the other three clusters. The fact that we have uncovered evidence for diffuse stellar envelopes surrounding all the clusters presented here suggests that perhaps stellar envelopes may be a common feature for Galactic globular clusters.

Recent studies that have looked for tidal extensions in globular clusters at comparable photometric depth, such as Jordi & Grebel (2010) and Carballo-Bello et al. (2012, 2014), have found evidence for extra tidal populations amongst most of the their targets. Jordi & Grebel (2010) found that most clusters in their sample show extra-tidal halo-like features.

That is, stellar populations beyond the tidal radius predicted by a King model fit (see also Grillmair et al. 1995). However, the extra-tidal populations exist within the Jacobi radii (i.e., still within the cluster potential), and their radial density profiles follow power law descriptions of $\gamma \leq -3$. The authors comment that these envelopes may just be an envelope of cluster stars, not strictly extra-tidal stars. The characteristics of the envelopes are very similar to the properties of the envelope we have uncovered around NGC 1261. Much the same is presented in Carballo-Bello et al. (2012): most of the clusters presented have power law descriptions of $\gamma \leq -3$ or steeper in their outer radial profiles. Models of clusters evolving in tidal fields predict a similar kind of phenomenon developing in the outer regions (e.g., Combes et al. 1999; Johnston et al. 1999; Testa et al. 2000; Küpper et al. 2010b).

The clusters we have studied in this thesis were also presented in Jordi & Grebel (2010) and Carballo-Bello et al. (2012, 2014). NGC 1851, NGC 5824 and M2 had power law like profiles of index $-3 < \gamma < -2$, sharper than our findings, but shallower than the majority of the clusters presented. NGC 1261, on the other hand, is consistent with the findings of Jordi & Grebel (2010) and Carballo-Bello et al. (2012). These studies help affirm our suggestion that the envelopes surrounding NGC 1851, NGC 5824 and M2 contrast with what we found around NGC 1261. Based on the consistency of steeper power law descriptions and the lower relative mass in the envelope, we suggest that NGC 1261 envelope has its origins as a product of the cluster's dynamical evolution. Whether the rest of the clusters featured in Jordi & Grebel (2010) and Carballo-Bello et al. (2012) with a similar power-law index to NGC 1261 possess cluster-like populations in the shape of an envelope between the tidal and Jacobi radii is a question that would be worth exploring.

Pfeffer et al. (2014) defined two criteria that may classify a globular cluster as a potential former dwarf galaxy nucleus. Those criteria are: variances in age and/or internal heavy element abundance spreads in their stellar populations. Furthermore, they predicted that the sample of clusters in the Milky Way that are dwarf galaxy nuclei is $1.9^{+1.3}_{-0.9}$ of mass $> 10^5$ $M_\odot$, though it worth mentioning that these numbers are . Based on the Pfeffer et al. (2014) definition, the number of globular clusters that can be considered as dwarf galaxy nuclei are ω Cen (e.g., Freeman 1993), M2 (e.g., Milone et al. 2015), M54 (e.g., Da Costa & Armandroff 1995), Terzan 5 (Ferraro et al. 2009), NGC 1851 (Bekki & Yong 2012), NGC 5824 (Da Costa et al. 2014) and NGC 5826 (Marino et al. 2015). There is cause for concern as the list of clusters is larger than the predicted number. We

speculate that the existence of a higher relative mass, shallower profile envelope as seen in NGC 1851 and M2 could be added to the criterion suggested by Pfeffer et al. (2014). Our added criteria, then, could help establish whether a given anomalous cluster is a dwarf galaxy nucleus or not. Exploring more of the higher mass or other anomalous clusters and their periphery for extra tidal debris will be key to understanding whether all anomalous clusters can be considered as dwarf galaxy nuclei.

The lack of tidal tails like those of Palomar 5 surrounding luminous clusters is of a particular note. As previously mentioned in this thesis, models of disrupting clusters have been shown to form tidal tails, with a stellar envelope potentially forming before stars can begin to populate the tails. Palomar 5 is a considerably lower mass cluster, even allowing for mass loss, compared to the other clusters studied in this thesis. Most recently, simulations of the evolution of high mass star clusters by Balbinot & Gieles (2017) found the mass of the cluster may affect the detectability of tidal tails. The authors comment that the median stellar mass in the cluster will be larger than the median stellar mass in the tidal debris. A result that is complimented by the different luminosity functions that exist in the tails and cluster presented in Koch et al. (2004). Therefore, this may make tidal tails around massive globular clusters, in particular, hard to detect. Fig. 2 in Balbinot & Gieles (2017) displays the median mass of the main-sequence turn-off (MSTO) and the median mass of the escaping stars as a function of time for a cluster of initial stellar mass of 2×10^5 $M_\odot$. While the median MSTO mass at 13 Gyr is ~ 0.2 $M_\odot$ higher than the median stellar mass of the escaper, the upper (first) quartile of the escaper's mass is within a few hundredths of a solar mass of the MSTO. In regards to the cluster we have studied with the smallest heliocentric distance, M2, our photometric limits corresponds to $\sim$0.5 $M_\odot$, about $\sim$0.3 $M_\odot$ beneath the MSTO mass of $\sim$ 0.8 $M_\odot$, based on a 13 Gyr isochrone[1] ($[Fe/H] = -1.7$, $[\alpha/Fe] = +0.4$) (Dotter et al. 2008). Therefore, deep imaging such as what has been analysed in this thesis may be able to detect the beginnings of tidal tails. We assert, however, that it is unclear how the models presented in Balbinot & Gieles (2017) translate to clusters of masses similar to that of the clusters studied here.

We stress that we are so far unable to be definitive as to the origins of the diffuse stellar envelopes. This is just one of the many important concerns and questions this thesis has raised about globular cluster evolution and extra-tidal populations. Others include:

- It is unclear whether a diffuse stellar envelope of the size akin to what is seen around

[1]Isochrone from Dartmouth Stellar Evolution Database, `http://stellar.dartmouth.edu/~models/index.html`

NGC 1851 and M2 can form through evolution of a cluster within the Milky Way's tidal field, as well as whether the envelopes are sufficiently robust to be long-lived structures.

- Are diffuse stellar envelopes ubiquitous amongst globular clusters? If so, is there a continuum of stellar envelopes sizes and/or features that connects the larger and smaller envelopes to tidal tails, or are the two kinds of envelopes we have uncovered here a real difference?

- Are all anomalous clusters the cores of dwarf galaxies, and does the existence of a diffuse stellar envelope help separate those clusters that are native to the Milky Way from those that are not?

It is abundantly clear that observing more clusters of varying luminosity to the level of precision and areal coverage achieved here will be beneficial to understanding and exploring these questions and more. This thesis has shown that not only can we learn about our Galaxy by studying the stars within the tidal radius of globular clusters, but also what lies outside.

5.1 Future Prospects

This thesis has surveyed the outer regions of a small number of clusters chosen from a larger sample. The sample of clusters consist of 25 targets that have either shown anomalous stellar properties or characteristics that suggest a potential connection to dwarf galaxies, or evidence for extra-tidal stellar populations. Excluding the four clusters presented in this thesis, data for 21 clusters have not yet been fully analysed. Combining the deep photometry of MegaCam and the incomparable field of view from the Dark Energy Camera as has been done here has the potential to uncover whether diffuse stellar envelopes are a common feature in outer halo globular clusters, locate disrupting clusters with tidal tails, or unveil large scale stellar features, comparable to the Sagittarius tidal stream. We note that the outer halo of M31 shows a substantial amount of substructure beyond 25 kpc, out to $\sim$ 150 kpc (e.g., Huxor et al. 2014). Consequently, the analysis of the clusters with larger Galactocentric distances will be of high priority to search for large-scale streams, while those closer to the disk may be prime targets for tidal tail studies. Stellar envelopes, however, may be found at all Galactocentric distances.

Virtually all globular clusters possess light element abundance variations. For first generation stars appear to typically be richer in C, O and Mg, while the second generation stars are enhanced in He, N, Na and Al (see Gratton et al. 2012a, for a review and references therein). It is currently undetermined as to how any given cluster can develop these variations amongst its stars, though there are proposals to explain the phenomenon. The abundance patterns are seen throughout the stellar evolutionary stages, therefore it is likely that the variations are present at formation. Mass loss from fast-rotating-massive-stars (Decressin et al. 2007) or asymptotic-giant-branch stars (D'Ercole et al. 2010), for example, may enrich the original gas to form the second generation of stars (see Renzini et al. 2015, and references therein)).

The discovery of the envelope surrounding NGC 1851 presented the perfect opportunity to explore both the light and heavy element abundances in stars in the envelope (Marino et al. 2014). The authors uncovered giants, which were identified as members in the envelope through radial velocities, that showed the same Fe-spread seen in the cluster, as well as s-process abundances (specifically, Sr and Ba) consistent with the bright sub-giant branch seen in the NGC 1851 colour-magnitude diagram. However, the authors found no evidence for stars belonging to the fainter sub-giant branch. The connection of the anomalous populations between the cluster and the envelope leads the authors to reaffirm the possibility of NGC 1851's connection to a disrupted dwarf galaxy. Now that we have identified three more stellar envelopes, spectroscopy of the stars in those envelopes would enable us to explore their properties. Properties such as velocity dispersions, element abundances and radial distributions of different populations will help give clarity into the origin of the stellar envelopes.

Our studies are based on main sequence and main sequence turn off stars. Consequently, the task of identifying appropriate targets for spectroscopic follow up may be challenging. Instruments such as DEIMOS[2] on the Keck II telescope and FLAMES[3] on the VLT may be able to reach the desired photometric depth for the main sequence within a reasonable exposure time, but they potentially will not able to give the ideal resolution needed to complete detailed chemical abundance studies. In the coming years, though, the task of selecting high probability cluster member targets for spectroscopic observations will get much easier. Large surveys will provide invaluable measurements of stellar properties that will avail target selection such as systemic and proper motions of clusters out to 50

[2] `https://www2.keck.hawaii.edu/inst/deimos/`

[3] `http://www.eso.org/sci/facilities/paranal/instruments/flames.html`

kpc from Gaia[4] and chemical tagging along the southern hemisphere from SkyMapper[5]. This holds particular relevance for NGC 7089, as the low line-of-sight velocity of the cluster makes it very hard to distinguish cluster members from field stars. The next generation of large telescopes and their accompanying instruments, such as the Many Instrument Fibre System (MANIFEST) on the Giant Magellan Telescope (GMT), will be able to provide multi-object capabilities over appropriate field sizes to explore the stellar populations of the cluster stars that are beyond the tidal radius. Further, the Large Synoptic Survey Telescope (LSST) will carry out a photometric survey and measure proper motions for the entire southern sky that will reach depths much greater than what has been achieved in this thesis.

Despite how much attention has been devoted to understanding the tidal tails of Palomar 5, observationally there is still much we can uncover. Due to declination limits of the SDSS, the southern (or leading) tail of Palomar 5 is largely unexplored. Without exploring the leading tail to the extent for the northern (or trailing) tail, we may not be fully equipped to completely understand this kind of stellar structure. The leading tail has been identified in the Pan-STARRS1 3π survery[6] (Bernard et al. 2016). It will be of great interest to see if the linear relationship of velocities seen in the stars belonging to the trailing tail continues to be best interpretation after the kinematics in the leading tail have been uncovered. Furthermore, Gaia will be able to determine the proper motions of tail stars and avail the calculation of orbits of not just the tails of Palomar, but the cluster as well.

Astronomy is changing. There is a plethora of new technologies and larger telescopes on the horizon with ambitious surveys and projects already being planned or in progress. All of this drive will pay dividends, as the current unanswered questions about the Milky Way's formation and evolution will be approached with the new array of tools. The questions of galaxy evolution through accretion, globular cluster evolution and dissolution and whether diffuse stellar envelopes are ubiquitous in the Galactic halo globular clusters will be either answered or great strides made towards their understanding. It is abundantly clear that while globular clusters have already taught us much about them and our Galaxy, we are only scratching the surface. Whether we look inside or outside globular clusters, we will understand how pivotal they are for the Galaxy, and the treasures they currently

[4] `http://sci.esa.int/gaia/`
[5] `http://skymapper.anu.edu.au/`
[6] `https://panstarrs.stsci.edu/`

withhold will be uncovered for all to see.

Bibliography

Ahn, C. P., Alexandroff, R., Allende Prieto, C., et al. 2014, ApJS, 211, 17

Alam, S., Albareti, F. D., Allende Prieto, C., et al. 2015, ApJS, 219, 12

Allen, C., Moreno, E., & Pichardo, B. 2006, ApJ, 652, 1150

Armandroff, T. E. & Da Costa, G. S. 1991, AJ, 101, 1329

Balbinot, E. & Gieles, M. 2017, arXiv:1702.02543

Balbinot, E., Santiago, B. X., da Costa, L. N., Makler, M., & Maia, M. A. G. 2011, MNRAS, 416, 393

Balbinot, E., Yanny, B., Li, T. S., et al. 2016, ApJ, 820, 58

Battaglia, G. & Starkenburg, E. 2012, A&A, 539, 123

Bekki, K. & Yong, D. 2012, MNRAS, 419, 2063

Bellazzini, M., Ferraro, F. R., & Ibata, R. 2003, AJ, 125, 188

Bellazzini, M., Ibata, R. A., Chapman, S. C., et al. 2008, AJ, 136, 1147

Bellini, A., Bedin, L. R., Piotto, G., et al. 2010, AJ, 140, 631

Belokurov, V., Evans, N. W., Irwin, M. J., Hewett, P. C., & Wilkinson, M. I. 2006a, ApJ, 637, L29

Belokurov, V., Zucker, D. B., Evans, N. W., et al. 2006b, ApJ, 642, L137

Bernard, E. J., Ferguson, A. M. N., Schlafly, E. F., et al. 2016, MNRAS, 463, 1759

Bertin, E. & Arnouts, S. 1996, A&AS, 117, 393

Binney, J. 1981, MNRAS, 196, 455

Binney, J. & Tremaine, S. 2008, Galactic Dynamics: Second Edition

Bland-Hawthorn, J. & Gerhard, O. 2016, ARA&A, 54, 529

Blumenthal, G. R., Faber, S. M., Primack, J. R., & Rees, M. J. 1984, Nature, 311, 517

Bonaca, A., Geha, M., Küpper, A. H. W., et al. 2014, ApJ, 795, 94

Bovy, J., Bahmanyar, A., Fritz, T. K., & Kallivayalil, N. 2016, ApJ, 833, 31

Bovy, J., Rix, H.-W., & Hogg, D. W. 2012, ApJ, 751, 131

Bullock, J. S. & Johnston, K. V. 2005, ApJ, 635, 931

Carballo-Bello, J. A., Gieles, M., Sollima, A., et al. 2012, MNRAS, 419, 14

Carballo-Bello, J. A., Sollima, A., Martínez-Delgado, D., et al. 2014, MNRAS, 445, 2971

Carlberg, R. G., Grillmair, C. J., & Hetherington, N. 2012, ApJ, 760, 75

Carraro, G. 2009, AJ, 137, 3809

Carraro, G., Zinn, R., & Moni Bidin, C. 2007, A&A, 466, 181

Carrera, R., Gallart, C., Pancino, E., & Zinn, R. 2007, AJ, 134, 1298

Carretta, E., Bragaglia, A., Gratton, R., D'Orazi, V., & Lucatello, S. 2009, A&A, 508, 695

Carretta, E., Bragaglia, A., Gratton, R. G., et al. 2010a, A&A, 520, A95

Carretta, E., Bragaglia, A., Gratton, R. G., et al. 2010b, A&A, 516, A55

Carretta, E., Gratton, R. G., Lucatello, S., et al. 2010c, ApJL, 722, L1

Casey, A. R., Da Costa, G., Keller, S. C., & Maunder, E. 2013, ApJ, 764, 39

Casey, A. R., Keller, S. C., & Da Costa, G. 2012, AJ, 143, 88

Chen, C. W. & Chen, W. P. 2010, ApJ, 721, 1790

Chernoff, D. F. & Weinberg, M. D. 1990, ApJ, 351, 121

Chun, S.-H., Kim, J.-W., Sohn, S. T., et al. 2010, AJ, 139, 606

Cohen, J. G. 1978, ApJ, 223, 487

Combes, F., Leon, S., & Meylan, G. 1999, A&A, 352, 149

Cooper, A. P., Cole, S., Frenk, C. S., et al. 2010, MNRAS, 406, 744

Correnti, M., Bellazzini, M., Dalessandro, E., et al. 2011, MNRAS, 417, 2411

Cottrell, P. L. & Da Costa, G. S. 1981, ApJ, 245, L79

Da Costa, G. S. 2012, ApJ, 751, 6

Da Costa, G. S. & Armandroff, T. E. 1995, AJ, 109, 2533

Da Costa, G. S., Held, E. V., & Saviane, I. 2014, MNRAS, 438, 3507

de Vaucouleurs, G. 1970, Science, 167, 1203

Decressin, T., Meynet, G., Charbonnel, C., Prantzos, N., & Ekström, S. 2007, A&A, 464, 1029

Dehnen, W., Odenkirchen, M., Grebel, E. K., & Rix, H.-W. 2004, AJ, 127, 2753

D'Ercole, A., D'Antona, F., Ventura, P., Vesperini, E., & McMillan, S. L. W. 2010, MNRAS, 407, 854

Dinescu, D. I., Girard, T. M., & van Altena, W. F. 1999, AJ, 117, 1792

Dotter, A., Chaboyer, B., Jevremović, D., et al. 2008, ApJS, 178, 89

Dotter, A., Sarajedini, A., Anderson, J., et al. 2010, ApJ, 708, 698

Eggen, O. J., Lynden-Bell, D., & Sandage, A. R. 1962, ApJ, 136, 748

Erkal, D., Koposov, S. E., & Belokurov, V. 2016, arXiv:1609.01282

Ferguson, A. M. N., Irwin, M. J., Ibata, R. A., Lewis, G. F., & Tanvir, N. R. 2002, AJ, 124, 1452

Ferraro, F. R., Dalessandro, E., Mucciarelli, A., et al. 2009, Nature, 462, 483

Flaugher, B., Diehl, H. T., Honscheid, K., et al. 2015, AJ, 150, 150

Fleming, D. E. B., Harris, W. E., Pritchet, C. J., & Hanes, D. A. 1995, AJ, 109, 1044

Freeman, K. C. 1970, ApJ, 160, 811

Freeman, K. C. 1993, in Astronomical Society of the Pacific Conference Series, Vol. 48, The Globular Cluster-Galaxy Connection, ed. G. H. Smith & J. P. Brodie, 608

Fukugita, M., Ichikawa, T., Gunn, J. E., et al. 1996, AJ, 111, 1748

Geisler, D., Claria, J. J., & Minniti, D. 1997, PASP, 109, 799

Gieles, M. & Zocchi, A. 2015, MNRAS, 454, 576

Gnedin, O. Y., Lee, H. M., & Ostriker, J. P. 1999, ApJ, 522, 935

Gnedin, O. Y. & Ostriker, J. P. 1997, ApJ, 474, 223

Goldsbury, R., Richer, H. B., Anderson, J., et al. 2010, AJ, 140, 1830

Gratton, R., Sneden, C., & Carretta, E. 2004, ARA&A, 42, 385

Gratton, R. G., Carretta, E., & Bragaglia, A. 2012a, A&AR, 20, 50

Gratton, R. G., Villanova, S., Lucatello, S., et al. 2012b, A&A, 544, A12

Grillmair, C. J. 2009, ApJ, 693, 1118

Grillmair, C. J. & Dionatos, O. 2006, ApJ, 641, L37

Grillmair, C. J., Freeman, K. C., Irwin, M., & Quinn, P. J. 1995, AJ, 109, 2553

Grillmair, C. J. & Johnson, R. 2006, ApJ, 639, L17

Gunn, J. E., Carr, M., Rockosi, C., et al. 1998, AJ, 116, 3040

Hanes, D. A. & Brodie, J. P. 1985, MNRAS, 214, 491

Harris, W. E. 1974, ApJ, 192, L161

Harris, W. E. 1996a, AJ, 112, 1487

Harris, W. E. 1996b, VizieR On-line Data Catalog, 7195, 0

Heggie, D. C. & Aarseth, S. J. 1992, MNRAS, 257, 513

Henden, A. A., Levine, S., Terrell, D., & Welch, D. L. 2015, AAS, 225, 336.16

Henden, A. A., Welch, D. L., Terrell, D., & Levine, S. E. 2009, AAS, 214, 407.02

Huxor, A. P., Mackey, A. D., Ferguson, A. M. N., et al. 2014, MNRAS, 442, 2165

Ibata, R. A., Gilmore, G., & Irwin, M. J. 1994, Nature, 370, 194

Ibata, R. A., Gilmore, G., & Irwin, M. J. 1995, MNRAS, 277, 781

Ibata, R. A., Lewis, G. F., McConnachie, A. W., et al. 2014, ApJ, 780, 128

Ivezic, Z., Tyson, J. A., Abel, B., et al. 2008, arXiv:0805.2366

Jester, S., Schneider, D. P., Richards, G. T., et al. 2005, AJ, 130, 873

Johnston, K. V., Sigurdsson, S., & Hernquist, L. 1999, MNRAS, 302, 771

Jordi, K. & Grebel, E. K. 2010, A&A, 522, 71

Kafle, P. R., Sharma, S., Lewis, G. F., & Bland-Hawthorn, J. 2014, ApJ, 794, 59

Keeping, E. S. 1995, Exact tests on samples from a normal population, 3rd edn. (Introduction to statistical inference. New York: Dover)

Keller, S. C., Schmidt, B. P., Bessell, M. S., et al. 2007, PASA, 24, 1

King, I. R. 1962, AJ, 67, 471

King, I. R. 1966, AJ, 71, 64

Klimentowski, J., Łokas, E. L., Kazantzidis, S., et al. 2009, MNRAS, 400, 2162

Koch, A., Grebel, E. K., Odenkirchen, M., Martínez-Delgado, D., & Caldwell, J. A. R. 2004, AJ, 128, 2274

Koposov, S. E., Belokurov, V., Torrealba, G., & Evans, N. W. 2015, ApJ, 805, 130

Kraft, R. P. 1994, PASP, 106, 553

Kron, G. E. & Mayall, N. U. 1960, AJ, 65, 581

Küpper, A. H. W., Balbinot, E., Bonaca, A., et al. 2015, ApJ, 803, 80

Küpper, A. H. W., Kroupa, P., Baumgardt, H., & Heggie, D. C. 2010a, MNRAS, 407, 2241

Küpper, A. H. W., Kroupa, P., Baumgardt, H., & Heggie, D. C. 2010b, MNRAS, 401, 105

Kuzma, P. B., Da Costa, G. S., Mackey, A. D., & Roderick, T. A. 2016, MNRAS, 461, 3639

Lardo, C., Mucciarelli, A., & Bastian, N. 2016, MNRAS, 457, 51

Lardo, C., Pancino, E., Mucciarelli, A., et al. 2013, MNRAS, 433, 1941

Lardo, C., Pancino, E., Mucciarelli, A., & Milone, A. P. 2012, A&A, 548, A107

Law, D. R. & Majewski, S. R. 2010a, ApJ, 718, 1128

Law, D. R. & Majewski, S. R. 2010b, ApJ, 714, 229

Law, D. R., Majewski, S. R., & Johnston, K. V. 2009, ApJL, 703, L67

Law, D. R., Majewski, S. R., & Johnston, K. V. 2010, AAS, 215, 322

Layden, A. C. & Sarajedini, A. 2000, AJ, 119, 1760

Leaman, R., VandenBerg, D. A., & Mendel, J. T. 2013, MNRAS, 436, 122

Lee, K. H., Lee, H. M., & Sung, H. 2006, MNRAS, 367, 646

Leon, S., Meylan, G., & Combes, F. 2000, A&A, 359, 907

Li, T. S., Balbinot, E., Mondrik, N., et al. 2016, ApJ, 817, 135

Lux, H., Read, J. I., Lake, G., & Johnston, K. V. 2013, MNRAS, 436, 2386

Lynden-Bell, D. & Eggleton, P. P. 1980, MNRAS, 191, 483

Lynden-Bell, D. & Wood, R. 1968, MNRAS, 138, 495

Mackey, A. D., Ferguson, A. M. N., Irwin, M. J., et al. 2010a, MNRAS, 401, 533

Mackey, A. D. & Gilmore, G. F. 2004, MNRAS, 355, 504

Mackey, A. D., Huxor, A. P., Ferguson, A. M. N., et al. 2010b, ApJL, 717, L11

Mackey, A. D., Huxor, A. P., Ferguson, A. M. N., et al. 2013, MNRAS, 429, 281

Mackey, A. D., Lewis, G. F., Collins, M. L. M., et al. 2014, MNRAS, 445, L89

Mackey, A. D. & van den Bergh, S. 2005, MNRAS, 360, 631

Majewski, S. R., Skrutskie, M. F., Weinberg, M. D., & Ostheimer, J. C. 2003, ApJ, 599, 1082

Marín-Franch, A., Aparicio, A., Piotto, G., et al. 2009, ApJ, 694, 1498

Marino, A. F., Milone, A. P., Karakas, A. I., et al. 2015, MNRAS, 450, 815

Marino, A. F., Milone, A. P., Yong, D., et al. 2014, MNRAS, 442, 3044

Martínez-Delgado, D., Gómez-Flechoso, M. Á., Aparicio, A., & Carrera, R. 2004, ApJ, 601, 242

Martinez Delgado, D., Zinn, R., Carrera, R., & Gallart, C. 2002, ApJ, 573, L19

Mastrobuono-Battisti, A., Di Matteo, P., Montuori, M., & Haywood, M. 2012, A&A, 546, L7

McConnachie, A. W. 2012, AJ, 144, 4

McConnachie, A. W., Irwin, M. J., Ibata, R. A., et al. 2009, Nature, 461, 66

McLaughlin, D. E. & van der Marel, R. P. 2005, ApJS, 161, 304

McLeod, B., Geary, J., Conroy, M., et al. 2015, PASP, 127, 366

McMillan, P. J. 2017, MNRAS, 465, 76

McMillan, S. & Hut, P. 1994, ApJ, 427, 793

Meylan, G. & Heggie, D. C. 1997, A&AR, 8, 1

Milone, A. P., Bedin, L. R., Piotto, G., et al. 2008, ApJ, 673, 241

Milone, A. P., Marino, A. F., Piotto, G., et al. 2015, MNRAS, 447, 927

Milone, A. P., Marino, A. F., Piotto, G., et al. 2015, ApJ, 808, 51

Milone, A. P., Piotto, G., Renzini, A., et al. 2017, MNRAS, 464, 3636

Milone, A. P., Stetson, P. B., Piotto, G., et al. 2009, A&A, 503, 755

Montuori, M., Capuzzo Dolcetta, R., Matteo, P. D., & Miocchi, P. 2008, ASPC, 390, 394

Myeong, G. C., Jerjen, H., Mackey, D., & Da Costa, G. S. 2017, ApJL, 840, L25

Navarrete, C., Belokurov, V., & Koposov, S. E. 2017, ApJL, 841, L23

Navin, C. A., Martell, S. L., & Zucker, D. B. 2015, MNRAS, 453, 531

Newberg, H. J. & Carlin, J. L., eds. 2016, Astrophysics and Space Science Library, Vol. 420, Tidal Streams in the Local Group and Beyond

Newberg, H. J., Yanny, B., & Willett, B. A. 2009, ApJL, 700, L61

Ngan, W. H. W. & Carlberg, R. G. 2014, ApJ, 788, 181

Niederste-Ostholt, M., Belokurov, V., Evans, N. W., et al. 2010, MNRASL, 408, L66

Norris, J., Cottrell, P. L., Freeman, K. C., & Da Costa, G. S. 1981, ApJ, 244, 205

Norris, J. E. & Da Costa, G. S. 1995, ApJ, 447, 680

Odenkirchen, M., Grebel, E. K., Dehnen, W., Rix, H.-W., & Cudworth, K. M. 2002, AJ, 124, 1497

Odenkirchen, M., Grebel, E. K., Dehnen, W., et al. 2003, AJ, 126, 2385

Odenkirchen, M., Grebel, E. K., Kayser, A., Rix, H.-W., & Dehnen, W. 2009, AJ, 137, 3378

Odenkirchen, M., Grebel, E. K., Rockosi, C. M., et al. 2001, ApJ, 548, L165

Olszewski, E. W., Saha, A., Knezek, P., et al. 2009, AJ, 138, 1570

Parmentier, G., Jehin, E., Magain, P., et al. 1999, A&A, 352, 138

Peacock, J. A., Cole, S., Norberg, P., et al. 2001, Nature, 410, 169

Pearson, S., Küpper, A. H. W., Johnston, K. V., & Price-Whelan, A. M. 2015, ApJ, 799, 28

Peterson, C. J. 1986, PASP, 98, 192

Pfeffer, J., Griffen, B. F., Baumgardt, H., & Hilker, M. 2014, MNRAS, 444, 3670

Piotto, G. 2009, The Ages of Stars, 258, 233

Planck Collaboration, Ade, P. A. R., Aghanim, N., et al. 2016, A&A, 594, A13

Renaud, F., Gieles, M., & Boily, C. M. 2011, MNRAS, 418, 759

Renzini, A., D'Antona, F., Cassisi, S., et al. 2015, MNRAS, 454, 4197

Riess, A. G. 1998, AAS, 192, 17.06

Robin, A. C., Reylé, C., Derrière, S., & Picaud, S. 2003, A&A, 409, 523

Rockosi, C. M., Odenkirchen, M., Grebel, E. K., et al. 2002, AJ, 124, 349

Roderick, T. A., Jerjen, H., Da Costa, G. S., & Mackey, A. D. 2016, MNRAS, 460, 30

Roderick, T. A., Jerjen, H., Mackey, A. D., & Da Costa, G. S. 2015, ApJ, 804, 134

Roederer, I. U., Mateo, M., Bailey, J. I., et al. 2016, MNRAS, 455, 2417

Roeser, S., Demleitner, M., & Schilbach, E. 2010, AJ, 139, 2440

Rubin, V. C., Ford, W. K. J., & Thonnard, N. 1980, ApJ, 238, 471

Saviane, I., Da Costa, G. S., Held, E. V., et al. 2012, A&A, 540, 27

Sbordone, L., Monaco, L., Moni Bidin, C., et al. 2015, A&A, 579, A104

Schlafly, E. F. & Finkbeiner, D. P. 2011, ApJ, 737, 103

Schlegel, D. J., Finkbeiner, D. P., & Davis, M. 1998, ApJ, 500, 525

Schönrich, R. & Binney, J. 2009, MNRAS, 399, 1145

Searle, L. & Zinn, R. 1978, ApJ, 225, 357

Siegel, M. H., Dotter, A., Majewski, S. R., et al. 2007, ApJ, 667, L57

Smith, G. H., Sneden, C., & Kraft, R. P. 2002, AJ, 123, 1502

Sollima, A., Gratton, R. G., Carballo-Bello, J. A., et al. 2012, MNRAS, 426, 1137

Spitzer, L. 1987, Dynamical evolution of globular clusters (Princeton, NJ, Princeton University Press, 1987, 191 p.)

Springel, V., White, S. D. M., Jenkins, A., et al. 2005, Nature, 435, 629

Starkenburg, E., Hill, V., Tolstoy, E., et al. 2010, A&A, 513, 34

Steinmetz, M. & Navarro, J. F. 2002, New. A., 7, 155

Tailo, M., Di Criscienzo, M., D'Antona, F., Caloi, V., & Ventura, P. 2016, MNRAS, 457, 4525

Takahashi, K. 1995, PASJ, 47, 561

Taylor, M. B. 2006, Astronomical Data Analysis Software and Systems XV ASP Conference Series, 351, 666

Testa, V., Zaggia, S. R., Andreon, S., et al. 2000, A&A, 356, 127

The Dark Energy Survey Collaboration. 2005, prepreint (astro–ph/0510346)

Tonry, J. L., Stubbs, C. W., Lykke, K. R., et al. 2012, ApJ, 750, 99

Trager, S. C., King, I. R., & Djorgovski, S. 1995, AJ, 109, 218

Trenti, M. & van der Marel, R. 2013, MNRAS, 435, 3272

Valdes, F., Gruendl, R., & DES Project. 2014, in Astronomical Society of the Pacific Conference Series, Vol. 485, Astronomical Data Analysis Software and Systems XXIII, ed. N. Manset & P. Forshay, 379

Vásquez, S., Zoccali, M., Hill, V., et al. 2013, A&A, 555, A91

Veljanoski, J., Ferguson, A. M. N., Mackey, A. D., et al. 2013, ApJ, 768, L33

Veljanoski, J., Mackey, A. D., Ferguson, A. M. N., et al. 2014, MNRAS, 442, 2929

Ventura, P., Caloi, V., D'Antona, F., et al. 2009, MNRAS, 399, 934

Villanova, S., Geisler, D., Carraro, G., Moni Bidin, C., & Muñoz, C. 2013, ApJ, 778, 186

Villanova, S., Geisler, D., Gratton, R. G., & Cassisi, S. 2014, ApJ, 791, 107

Villanova, S., Geisler, D., & Piotto, G. 2010, ApJL, 722, L18

von Hoerner, S. 1957, ApJ, 125, 451

Walker, A. R., Kunder, A. M., Andreuzzi, G., et al. 2011, MNRAS, 415, 643

Walker, M. G., Mateo, M., Olszewski, E. W., et al. 2006, AJ, 131, 2114

Webb, J. J., Leigh, N., Sills, A., Harris, W. E., & Hurley, J. R. 2014, MNRAS, 442, 1569

Wegg, C. & Gerhard, O. 2013, MNRAS, 435, 1874

White, S. D. M. & Rees, M. J. 1978, MNRAS, 183, 341

Wilson, C. P. 1975, AJ, 80, 175

Yanny, B., Newberg, H. J., Johnson, J. A., et al. 2009a, ApJ, 700, 1282

Yanny, B., Rockosi, C., Newberg, H. J., et al. 2009b, AJ, 137, 4377

Yong, D. & Grundahl, F. 2008, ApJL, 672, L29

Yong, D., Grundahl, F., D'Antona, F., et al. 2009, ApJL, 695, L62

Yong, D., Grundahl, F., & Norris, J. E. 2015, MNRAS, 446, 3319

Yong, D., Roederer, I. U., Grundahl, F., et al. 2014, MNRAS, 441, 3396

York, D. G., Adelman, J., Anderson, J. E. J., et al. 2000, AJ, 120, 1579

Zacharias, N., Finch, C. T., Girard, T. M., et al. 2013, AJ, 145, 44

Zoccali, M. & Valenti, E. 2016, PASA, 33, e025